UNIVERSIDADE DE BRASÍLIA

INSTITUTO DE GEOCIÊNCIAS

DEFORMAÇÃO, ALTERAÇÃO HIDROTERMAL E MINERALIZAÇÃO AURÍFERA ASSOCIADOS AO GRANITO PRÍNCIPE, DISTRITO AURÍFERO DE NATIVIDADE.

ROBERTO DE SIQUEIRA CORRÊA

DISSERTAÇÃO DE MESTRADO N° 335

Brasília, 2014.

UNIVERSIDADE DE BRASÍLIA

INSTITUTO DE GEOCIÊNCIAS

DISSERTAÇÃO DE MESTRADO N° 335

DEFORMAÇÃO, ALTERAÇÃO HIDROTERMAL E MINERALIZAÇÃO AURÍFERA ASSOCIADOS AO GRANITO PRÍNCIPE, DISTRITO AURÍFERO DE NATIVIDADE.

Área de Concentração: Geologia Econômica e Prospecção

Mestrando: Roberto de Siqueira Corrêa

Banca Examinadora:
Claudinei Gouveia de Oliveira (UnB - Orientador)
Raul Minas Kuyumjian (UnB)
Lydia Maria Lobato (UFMG)

Brasília, 2014.

Oh Very Young

Oh Very Young, What You Will Leave Us This Time?
You're Only Dancing on This Earth For A Short While
And Though Your Dreams May Toss And Turn You Now,
They Will Vanish Away Like Your Daddy's Best Jeans
Denim Blue Fading Up To The Sky
And Though You Want Him To Last Forever You Know He Never Will
And The Patches Make The Goodbye Harder Still

Oh Very Young, What Will You Leave Us This Time?
There will Never Be A Better Chance to Change Your Mind
And If You Want This World To See A Better Day
Will You Carry The Words Of Love With You,
Will You Ride The Great White Bird Into Heaven?
And Though You Want To Last Forever You Know You Never Will
And The Goodbye Makes The Journey Harder Still

Oh Very Young, What You Will Leave Us This Time?
You're Only Dancing on This Earth For A Short While
Oh Very Young, What You Will Leave Us This Time?

Yusuf Islam/Cat Stevens

AGRADECIMENTOS

Deus

Jesus, Buda e Mestres Iniciados

José, Rosa, Rosália, Eva e Família

Júlia

Claudinei

Roberta

Valmir, Elton, Maria Emília, Nilson, Márcia e professores do IG

Lorena e companheiros do TF 2012

Débora e Weska

Felipe, Érico, Gilbésio, Chechel e pessoal do Laboratório de Geocronologia

Jacqueline e Ricardo

Ziba, Raimundo, Francisca, Estela, Alice, Corrêa, Dione, Tião e demais funcionários do IG

Isa, Berna, Debs, Renatchongas, Rafa, Titi, Citão, Gaucho, Cirus, Caiopira, Toscoman, Leo, Brant e demais companheiros da Pós

Chico, Tomj, Nate, Maria, Sertão, Feique, Pedro e povo da Geo/UnB 2°/2008

Daldegudo, Feliz, Rafa, Faustão, Túlio, Thais, Faby, Deusa, Gus e amigos da Graduação

Mestres Tânia, Aristein e Woo e John, Emília, Tauana, Day, Cleitinho e Paulinho

Gabs, Fábio, Clara, Tinho, Nasce, Tanália, Naty, Mariposa, Vic, Galo, Pedrão, Petry, Menck, Mariana, Marina, Sheep, Fernando, Hanna, Dan, Deyse, Renkeriano, Antônio Lucas e demais amigos do coração

RESUMO

Inserido no Distrito Aurífero Natividade, o Depósito de Príncipe tem sua origem associada à implementação de um sistema regional do tipo *strike-slip* durante o Evento Brasiliano, no Neoproterozoico. A associação litológica local, entretanto, possui idades mais antigas, datadas por U-Pb em zircão e Sm-Nd como Paleoproterozoicas, conferindo um caráter epigenético para este depósito. Ela é constituída por um embasamento composto pela Suíte tonalítica-granodiorítica Rio do Moleque, que foi intrudida pelo Granito Príncipe, de natureza peraluminosa. Após um período de calmaria tectônica, estas unidades foram submetidas a um metamorfismo regional em fácies xisto verde e processos de deformação e hidrotermalismo, produzindo tectonitos metamórficos dentro do Granito Príncipe e hidrotermalitos na extremidade norte deste corpo intrusivo, que é onde o depósito está localizado. Nele, há um forte controle estrutural através de zonas de cisalhamento rúpteis-dúcteis de orientação N-N20°E que ocorrem em todas as escalas de observação e culminam num sistema pervasivo e interconectado de veios descontínuos e anastomosados, compostos por quartzo, carbonato, sulfetos e ouro.

Produtos geofísicos de gamaespectrometria e magnetometria auxiliam na definição dos limites litológicos e na delimitação de estruturas para este depósito, respectivamente. Na gamaespectrometria, a composição ternária RGB evidencia o formato sigmoide do Granito Príncipe, que possui assinatura de alto K-eTh-eU, com sombras de pressão nas suas extremidades sul (alto K), composta por pegmatitos, e norte (alto eTh), composta por hidrotermalitos, a exemplo de um objeto cinemático dextral do tipo sigma. Cristas bastante pronunciadas no interior do Granito Príncipe em imagens de K e K anômalo correspondem a faixas de tectonitos caracterizados por biotita-sericita-quartzo-xistos. Em produtos magnetométricos e em processamentos por *matched filtering* e deconvolução de Euler, há anomalias que bordejam o Granito Príncipe e suas sombras de pressão, sendo associadas a zonas de cisalhamento. Há também falhas N45°E, que correspondem ao *trend* regional do Lineamento Transbrasiliano, e EW, mais rasas e de caráter rúptil.

As zonas de cisalhamento presentes na área foram determinantes para a formação do depósito, promovendo o fluxo canalizado da solução hidrotermal até o sítio de precipitação aurífera, onde a migração adquiriu caráter pervasivo. Ao longo destas estruturas, há evidências de processos de alteração hidrotermal em diferentes intensidades, caracterizados essencialmente pela hidrólise dos minerais ígneos primários, originando uma paragênese neoformada. Durante a deformação, o Granito Príncipe atuou como um obstáculo para o hidrotermalismo e deformação, originando duas sombras de pressão, que atuaram como *traps* estruturais para o minério. Por serem zonas de alívio, onde os valores de tensão são menores, as sombras de pressão trapearam a solução hidrotermal. Outra característica deste tipo de estrutura é o de desestabilizar as condições físico-químicas do fluido através de quedas bruscas de pressão e aumento da interação fluido-rocha, fazendo com que o ouro e metais associados fossem precipitados.

Estudos de inclusões fluidas apontam uma natureza aquo-carbônica com salinidade média de 5% equivalente em peso de NaCl. Estudos termométricos apontam que a mineralização aurífera ocorreu entre 250°C e 400°C. Análises por isótopos estáveis de S, C e O sugerem uma fonte metamórfica para o fluido e estudos geoquímicos em rochas e minerais indicam processos de alteração hidrotermal envolvendo metassomatismo em Fe, Ca, Mg, K, Na, Au, Ag, entre outros.

Pelas características apresentadas, o Depósito de Príncipe se encaixa na classe de depósitos orogênicos, se distinguindo das demais ocorrências do Distrito Aurífero Natividade e da maioria dos depósitos orogênicos do mundo pelas suas feições singulares, com destaque para sua sombra de pressão de escala regional.

PALAVRAS-CHAVE: FAIXA BRASÍLIA, NATIVIDADE, OURO OROGÊNICO

ABSTRACT

Situated at the Natividade Gold District, the Príncipe Gold Deposit was formed after the establishment of a regional strike-slip system during the Neoproterozoic Brasiliano Event. The area rocks, however, were dated by zircon U-Pb and Sm-Nd as Paleoproterozoic, providing an epigenetic character for this deposit. The local lithological association is constituted by the Rio do Moleque tonalitic-granodioritic suite that was intruded by the peraluminous Príncipe Granite. During the Neoproterozoic these units undergone greenschist facies metamorphism and deformational and hydrothermal events, forming metamorphic tectonites inside the Príncipe Granite and hydrothermalites at the granite's northern border, which is where the Príncipe Gold Deposit is located. Inside it, a strong structural control can be verified, with N-N20°E-trending brittle-ductile shear zones that appear at all scales of observation and end up as an interconnected pervasive system of discontinuous and anastomosed quartz-carbonate-sulphide-gold-veins.

Airbone gamma-ray spectrometric and magnetometric geophysical products helped to delimitate lithological boundaries and structures for this deposit. Gamma images such as the RGB ternary composition highlight the Príncipe Granite's sigmoid shape, with a high K-eTh-eU signature. Two southern high-K and northern high-eTh pressure shadows are also evident, with the southern composed by pegmatites and the northern by hydrothermally altered granitoids, where the Príncipe Gold Deposit is located. These three lithologies assemble a dextral sigma-type kinematic object. High-K lineaments inside the Príncipe Granite can be identified at the K and Anomalous K images, corresponding to tectonites, defined as biotite-sericite-quartz-schists. In Matched Filtering and Euler Deconvolution analyses, anomalies at the Príncipe Granite's borders were identified and correlated to shear zones. N45°E-trending anomalies were also identified, corresponding to faults parallel to the regional Transbrasiliano Lineament Trend. These analyses also identified EW-trending shallower anomalies that were associated to younger brittle faults.

The shear zones played an important role for the deposit formation, acting as pathways that promoted a channelized fluid flow until the site of metal precipitation. Hydrothermal alteration processes in different grades can be verified along these structures, mainly characterized by the primary minerals hydrolysis, originating a neoformed mineral assemblage. The Príncipe Granite acted as an obstacle for the hydrothermalism and deformation, producing two pressure shadows that acted as structural traps for the ore. Since they are stress release zones, these structures concentrated the hydrothermal solution. They also changed the physicochemical conditions of the fluid through abrupt pressure lowerings and an increase of the fluid-rock interaction rate, precipitating gold and other base metals.

Fluid inclusion studies point an aqueous-carbonic nature for the fluid with 5% NaCl equivalent weight and thermometric studies suggest that the gold mineralization occurred between 250°C and 400°C. S, C and O stable isotopes indicate a metamorphic source for the fluid. Whole rock geochemistry and microprobe studies highlight hydrothermal alteration processes involving Fe, Ca, Mg, K, Na, Au, Ag metasomatism.

The Príncipe Gold Deposit belongs to the orogenic class, being distinguished from the other occurrences inside the Natividade Gold District and from most orogenic deposits of the world for its singular features, such as the regional-scale auriferous pressure shadow.

KEYWORDS: BRASÍLIA FOLD BELT, NATIVIDADE, OROGENIC GOLD

SUMÁRIO

CAPÍTULO I

1. APRESENTAÇÃO E OBJETIVOS

Esta dissertação de mestrado consiste na continuação dos trabalhos iniciados com o trabalho de conclusão de curso de 2012 da Universidade de Brasília, em que uma área de 1.440 km² ao redor da cidade de Natividade-TO foi mapeada na escala 1:50.000. Este trabalho – denominado de Projeto Natividade – empreendeu técnicas de geofísica e sensoriamento remoto e aquisição de dados estruturais, litológicos e petrográficos, levando à proposição de hipóteses e sugestões acerca dos eventos deformacionais, metamorfismo, evoluções geológica e tectônica e potencial econômico. As principais justificativas do Projeto Natividade envolviam dois tópicos: O aprimoramento da compreensão das associações litológicas e evolução geológica da área e o mapeamento e caracterização de ocorrências auríferas na região.

Para melhor esclarecer estes tópicos, entretanto, tornaram-se necessárias informações complementares oriundas de técnicas analíticas que tradicionalmente não são contempladas nestes trabalhos de graduação. Deste modo, foram conduzidos estudos de geoquímica, geocronologia, isótopos estáveis, microssonda eletrônica, inclusões fluidas, além de análises mais aprofundadas de geofísica e petrografia. Para o caso específico desta dissertação, o segundo tópico foi escolhido com o objetivo de compreender os processos de mineralização aurífera na região.

Esta região é conhecida por sua história relacionada à extração de ouro, que teve início em meados do século XVIII e foi responsável pela criação e desenvolvimento de diversas cidades ao longo do Município de Natividade. Devido à sua relevância econômica, ocorreu sua denominação de Distrito Aurífero Natividade. Atualmente, existem quatro localidades que mantém essas atividades, nos depósitos de Chapada de Natividade, Serra de Natividade, Geominas e Príncipe. Esta dissertação manteve o foco no Depósito de Príncipe, porém apresenta algumas comparações com o Depósito de Chapada de Natividade, buscando verificar feições comuns e características distintas entre eles.

Os principais objetivos consistem na caracterização geológica das rochas do depósito, como o Granito Príncipe, tectonitos e hidrotermalitos, a serem definidos na seção de Geologia Regional, e a determinação dos principais mecanismos metalogenéticos que levaram à extração, transporte e deposição do ouro.

A dissertação é dividida em três capítulos. O Capítulo I está escrito em língua portuguesa e possui caráter introdutório, buscando familiarizar o leitor com a geologia da região. Para tanto, consiste nesta seção de Apresentação e Objetivos, na de Geologia Regional

e na de Histórico de Mineralizações Auríferas. Estas duas últimas seções evocam trabalhos regionais e locais já realizados. O Capítulo II está escrito em língua inglesa e é o foco desta dissertação, apresentando os dados obtidos durante o período do mestrado com o intuito de publicação em revista internacional na área de geologia econômica. O Capítulo III está escrito em língua portuguesa e é essencialmente uma parte de discussões/conclusões extendida, com o fim de sintetizar e esclarecer os principais pontos da dissertação.

2. GEOLOGIA REGIONAL

A área de estudo está inserida na porção setentrional da Faixa de Dobramentos Brasília, pertencente à Província Tocantins (Almeida et al., 1981; Fuck et al., 2005). Ela possui origem associada ao Ciclo Brasiliano, evento Neoproterozoico que consistiu na colisão entre os crátons Amazônico e do São Francisco (Brito Neves & Cordani, 1991), formando a Faixa Brasília. Esta faixa de dobramentos é segmentada na direção norte-sul com as porções Meridional, de orientação sudeste, e Setentrional, de *trend* nordeste (Araújo Filho, 2000).

Na direção leste-oeste, a compartimentação se dá em quatro unidades tectônicas (Fuck et al., 2005), compostas pelo Arco Magmático de Goiás, formado pelos arcos neoproterozoicos juvenis de Mara Rosa e Arenópolis; o Maciço de Goiás, um terreno granito-*greenstone* que foi acrescionado à faixa durante a Orogênese Brasiliana, interpretado como o embasamento da Faixa Brasília Setentrional (Cordeiro, 2014); o Núcleo Metamórfico, composto pelos terrenos granulíticos dos complexos Anápolis-Itauçu e Uruaçu e pelas intrusões máfico-ultramáficas acamadadas granulitizadas dos complexos de Canabrava, Niquelândia e Barro Alto; o Cinturão de dobras e empurrões, composto por sequências sedimentares representadas pelos grupos Paranoá, Bambuí, Araxá, Canastra, Ibiá e Vazante e pelas sequências do tipo rifte dos grupos Araí, Serra da Mesa e Natividade. O Depósito de Príncipe está localizado no Domínio Almas-Conceição do Tocantins, caracterizado por um embasamento composto por associações paleoproterozoicas de terrenos TTG e sequências metavulcanossedimentares com a cobertura das rochas metassedimentares do Grupo Natividade (Figura 1).

Outra terminologia, traduzida como o "Bloco Crustal Cavalcante-Natividade" (Fuck et al., 2014), representa o embasamento siálico de rochas supracrustais na Faixa Brasília Setentrional, tais como os grupos Serra da Mesa, Araí e Natividade. As rochas que compõem o embasamento pertencem em parte ao Terreno Almas-Dianópolis e em parte à Suíte Aurumina, onde granitoides de assinatura peraluminosa afloram se estendendo da cidade de Cavalcante até Pindorama do Tocantins, situada a norte de Natividade (Figura 2).

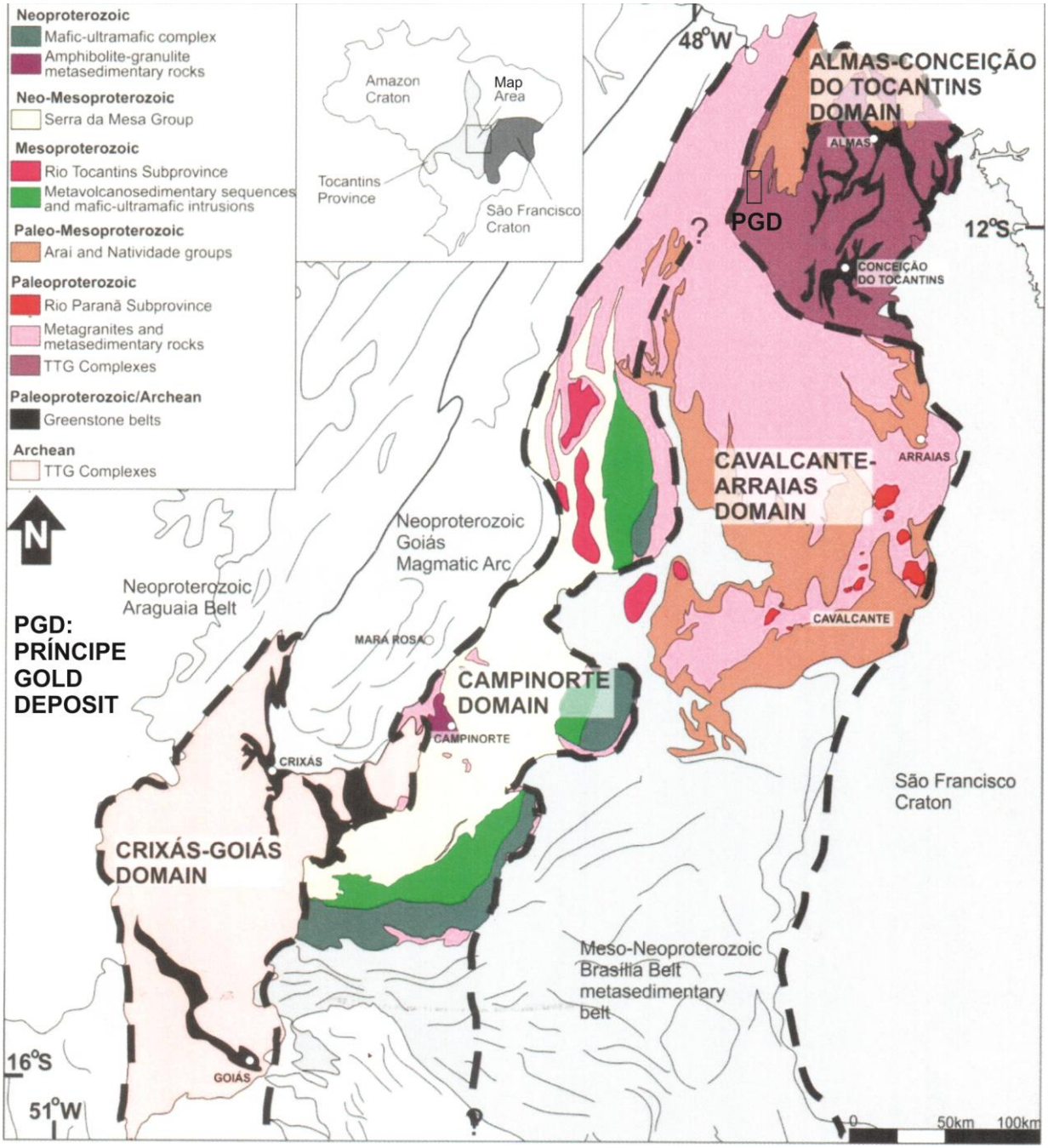

Figura 1. Mapa geológico da Faixa Brasília retirado de Cordeiro (2014). O Depósito Aurífero de Príncipe (PGD), que engloba a área desta dissertação de mestrado, está destacado e exagerado pela área no extremo norte do mapa. Nele, a região é caracterizada por um embasamento paleoproterozoico composto por complexos granito-gnaissicos associado a rochas metavulcânicas e metassedimentares.

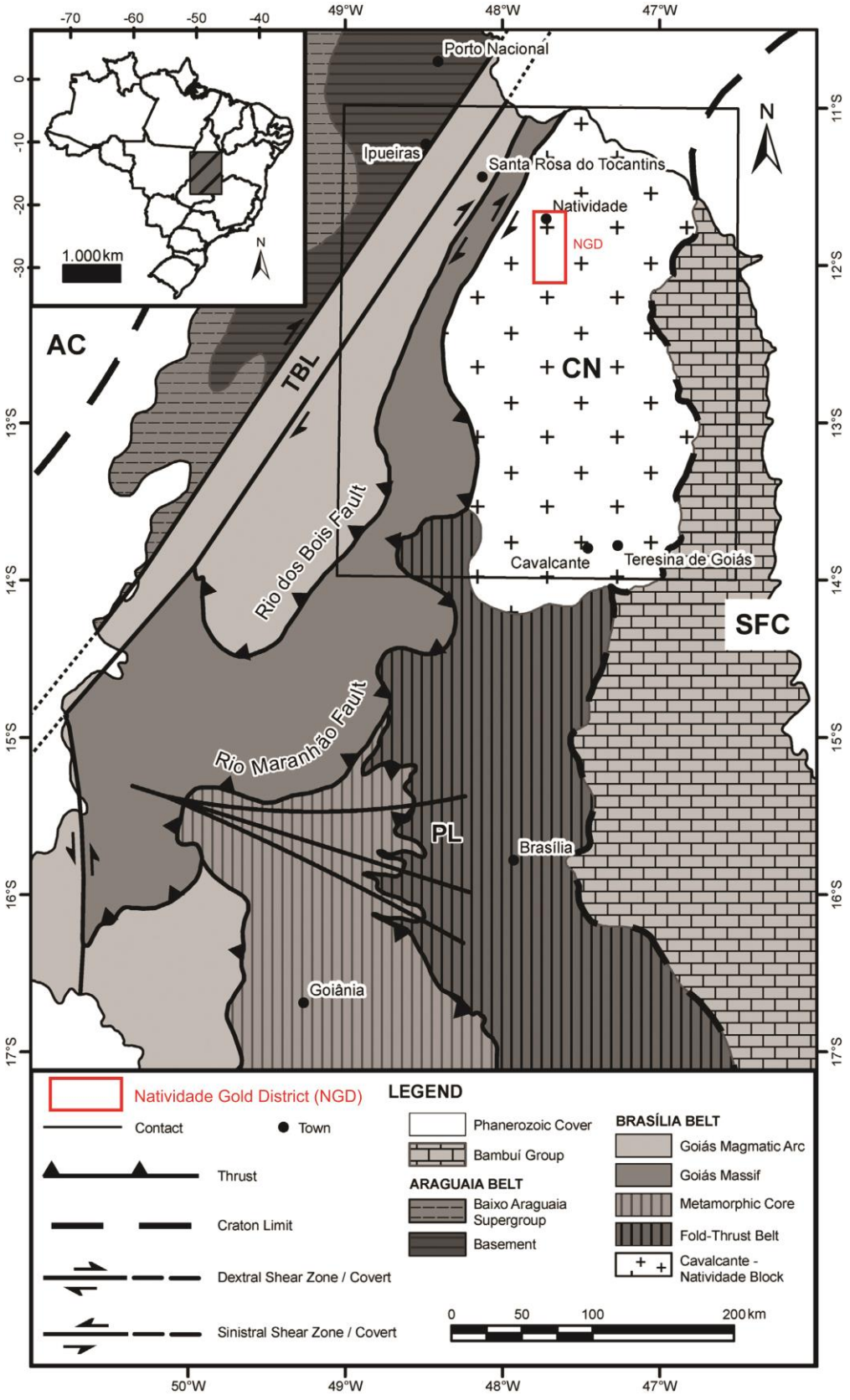

Figura 2. Mapa geológico que representa o Bloco Cavalcante-Natividade extraído de Fuck et al. (2014). O Distrito Aurífero Natividade (NGD) está com suas dimensões exageradas e encontra-se evidenciado pela área vermelha.

Segundo estas classificações, o Depósito de Príncipe fica localizado na Faixa Brasília Setentrional, no Maciço de Goiás, no domínio Almas-Conceição do Tocantins, no Bloco Cavalcante-Natividade (Figuras 1 e 2). Outra definição visando a caracterização do embasamento envolve o termo "Terreno Almas-Dianópolis" (Cruz & Kuyumjian, 1998) ou "Terreno Granito-*Greenstone* do Tocantins" (Kuyumjian et al., 2012). Eles são definidos como várias faixas de *greenstone belts* envoltas por intrusões dômicas de complexos granito-gnaissicos tipo TTG entre as cidades de Almas e Dianópolis, mas que se estendem até as proximidades de Natividade (Figura 3). Este padrão é muito claro em imagens de magnetometria (Figura 4), com morfologia em Y (Oliveira et al., 2012). Os altos valores magnéticos estão correlacionados aos *greenstone belts*, enquanto os baixos estão associados às suítes tipo TTG.

No trabalho de mapeamento 1:250.000 da Folha Arraias (Abdallah, 2011; Abdallah & Meneghini, 2013) pelo Serviço Geológico do Brasil (CPRM), o embasamento granito-gnaissico é composto por "granitoides de terrenos acrescionários de Arco Magmático", subdivididos em duas séries geoquímicas. A primeira, composta por granitoides calci-alcalinos metaluminosos que contém anfibólio e biotita, é associada ao Complexo Almas-Cavalcante, formada em ambiente convergente de margem continental. A segunda, constituída por granitoides peraluminosos que contém muscovita, biotita e granada magmáticas, é associada à Suíte Aurumina (Botelho et al., 1999), formada sob regime tectônico sin- a pós-colisional. Datações U-Pb nestas litologias (Abdallah & Meneghini, 2013; Fuck et al., 2014) sugerem a progressão do arco continental de 2,2 a 2,17 Ga para a colisão de blocos, determinada no intervalo de 2,03 a 2,15 Ga (Figura 5).

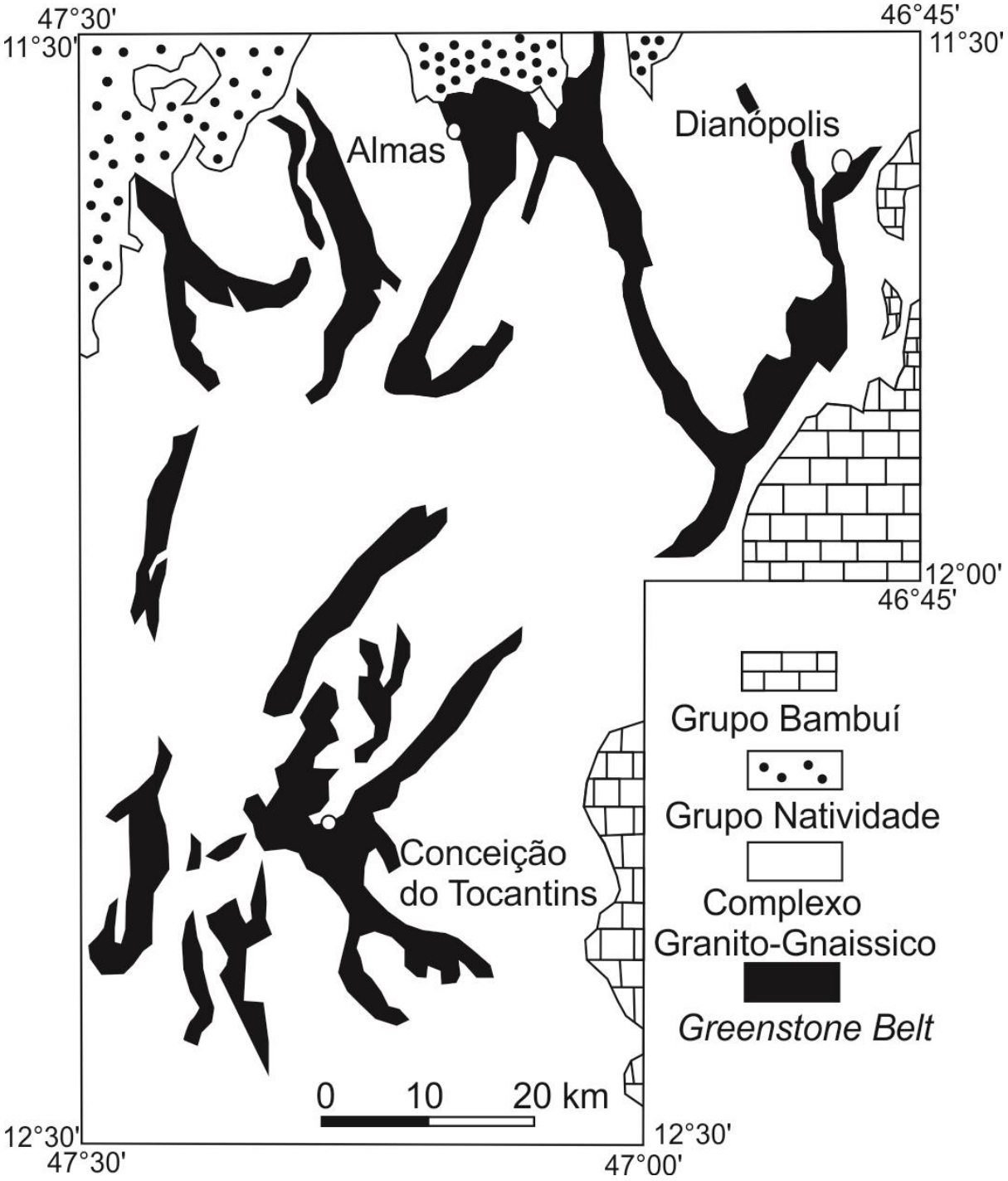

Figura 3. Mapa geológico simplificado do Terreno Almas-Dianópolis adaptado de Cruz & Kuyumjian (1998). Este terreno, localizado nas proximidades do Distrito Aurífero Natividade, é caracterizado por sequências de *greenstone belts* intrudidas por complexos granito-gnaissicos.

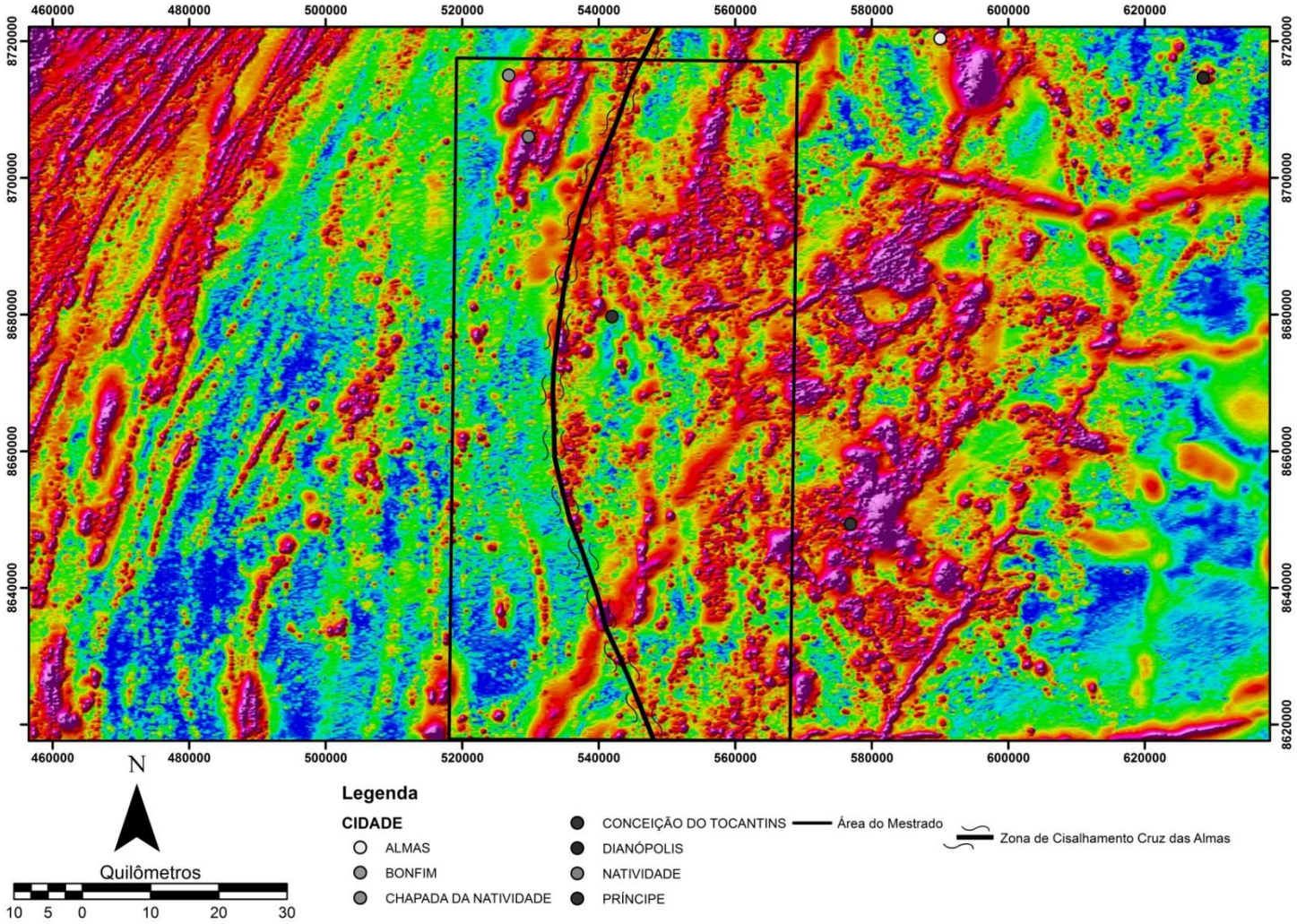

Figura 4 Imagem da Amplitude do Sinal Analítico (ASA) regional, com a área desta dissertação de mestrado destacada pelo retângulo preto. Este produto geofísico evidencia a distinção das respostas magnéticas entre o Terreno Almas-Dianópolis, à leste e com o padrão em Y, e a área a oeste, de repostas mais discretas. Sua separação se dá pela Zona de Cisalhamento Cruz das Almas, estrutura interpretada como um limite de blocos tectônicos por Oliveira et al. (2012).

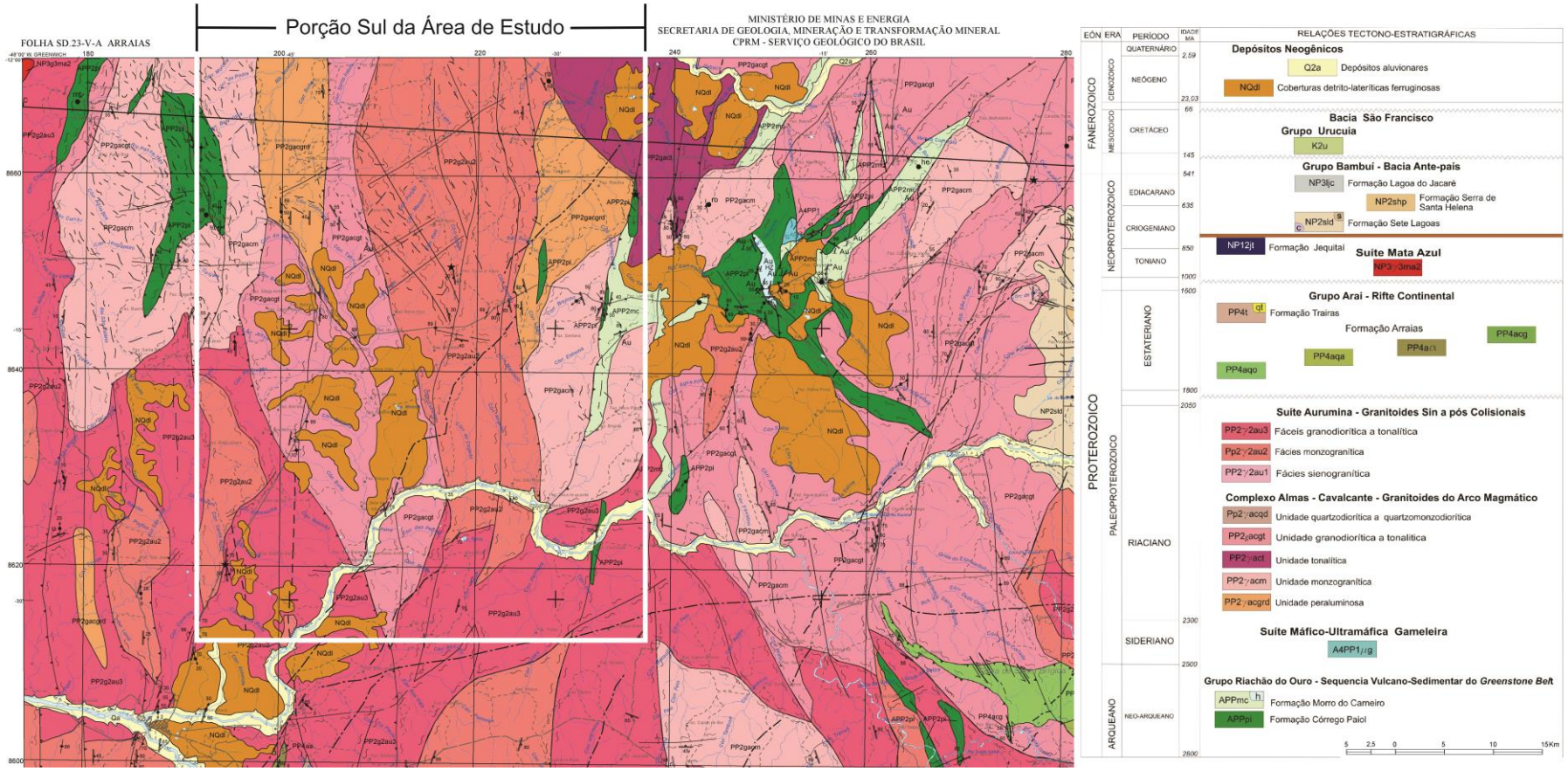

Figura 5. Detalhe do mapa geológico 1:250.000 da Folha Arraias realizado pela CPRM (Abdallah & Meneghini, 2013), com a área do mestrado destacada pelo retângulo branco. Neste domínio, o embasamento é definido por corpos intrusivos referentes à Suíte Aurumina, com discretas faixas do *greenstone* Riachão do Ouro e granitoides do Complexo Almas-Cavalcante.

O mapeamento realizado pelo Projeto Natividade (2012) individualizou unidades litológicas previamente indiferenciadas para o embasamento granito-gnaissico paleoproterozoico, definindo a sequência metavulcanossedimentar Água Suja (Queiroz, 2001), as suítes granodioríticas-tonalíticas Manuel Alves e Rio do Moleque, a suíte granítica-pegmatítica Xobó (Gorayeb et al., 1988) e o Granito Príncipe. Ainda para o embasamento, foram identificadas as unidades neoproterozoicas Tectonitos, Hidrotermalitos e Cianititos. A sequência supracrustal mapeada corresponde às rochas metassedimentares do Grupo Natividade, constituindo as principais serras da área (Figura 6).

A unidade litológica mais antiga na área corresponde à Sequência Metavulcanossedimentar Água Suja, análoga à sequência de *greenstone* do terreno Almas-Dianópolis, o Grupo Riachão do Ouro (Correia Filho & Sá, 1980). Estas unidades apresentam, entretanto, algumas diferenças nas variedades de rochas encontradas, tendo sido diferenciadas por Queiroz (2001). Ela apresenta rochas oriundas de sedimentações clástica e química intercaladas a rochas vulcânicas, tendo origem associada a bacias de *back-arc* riacianas (Oliveira et al., 2012).

Esta sequência foi intrudida pelas suítes tonalíticas-granodioríticas Manuel Alves e Rio do Moleque em ambiente de arco. Posteriormente, em ambiente colisional, ocorreu a ascensão dos magmas félsicos peraluminosos da Suíte Xobó e do Granito Príncipe formados a partir de processos de fusão parcial (Oliveira et al., 2012). No Estateriano, processos de rifteamento promoveram a deposição dos sedimentos relativos ao Grupo Natividade.

Após um período de quiescência tectônica, o Ciclo Brasiliano implementou no Neoproterozoico um sistema transcorrente, provocando a deformação, o metamorfismo e o hidrotermalismo das rochas da área, formando as unidades Cianititos, Tectonitos e Hidrotermalitos. Tais litologias neoproterozoicas possuem definições específicas e serão referidas nesta dissertação segundo estes conceitos: A unidade Tectonitos corresponde a faixas de alta deformação inseridas dentro do Granito Príncipe análogas a xistos oriundos dos processos de blastese e recristalização desta rocha granítica. Estas rochas são tipicamente compostas por quartzo e filossilicatos; A unidade Hidrotermalitos representa granitoides alterados hidrotermalmente em diferentes graus dentro de um domínio situado na extremidade norte do Granito Príncipe; A unidade Cianititos corresponde a rochas que contém cianita que ocorrem ao longo da zona de cisalhamento Cruz das Almas.

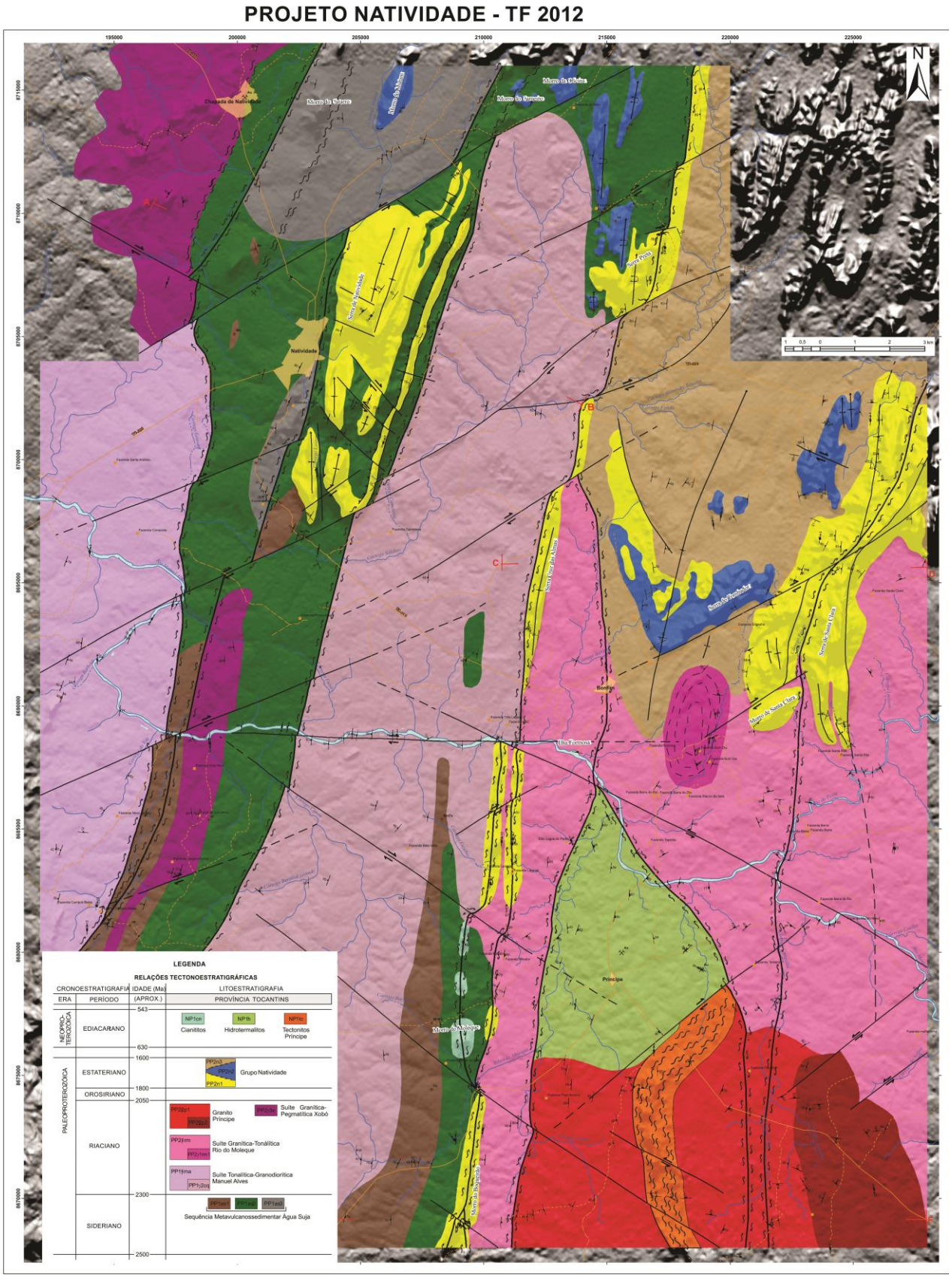

Figura 6. Mapa geológico 1:50.000 elaborado por Oliveira et al. (2012). Este mapa indica uma associação litológica paleoproterozoica retrabalhada durante o Ciclo Brasiliano. O Depósito Aurífero de Príncipe está destacado na região verde clara, onde está definida a Unidade Hidrotermalitos.

3. HISTÓRICO DE MINERALIZAÇÕES AURÍFERAS

Nestes trabalhos também são ressaltados os aspectos estruturais, deformacionais e metamórficos a que esta região foi submetida, estando diretamente relacionados às mineralizações auríferas (Queiroz, 2001; Alvarez, 2006; Oliveira et al., 2012; Corrêa et al., 2013). Foram identificados dois eventos deformacionais, sendo o primeiro paleoproterozoico e não associado à mineralização (Kuyumjian et al., 2012), com metamorfismo em fácies anfibolito (Oliveira et al., 2012), e o segundo neoproterozoico, oriundo do Ciclo Brasiliano (Schobbenhaus et al., 1984). A área de estudo está na zona de influência do Lineamento Transbrasiliano, responsável pela formação, reativação e rotação de zonas de cisalhamento dextrais de mergulho subvertical e orientação NS-N20°E. Este evento de transcorrência foi responsável pelo metamorfismo regional sob fácies xisto verde e pela implementação de processos de milonitização e hidrotermalismo nas rochas da área, originando vários depósitos auríferos do tipo orogênico (Kuyumjian et al., 2012).

Na região, a estrutura de maior destaque é a zona de cisalhamento Cruz das Almas, destacada na Figura 4. Ela foi interpretada como uma zona de sutura entre blocos de rochas paleoproterozoicas, separando as suítes Manuel Alves e Rio do Moleque (Oliveira et al., 2012; Sousa & Oliveira, 2013). Sua extensão é superior a 100 km, marcada por serras descontínuas de cristas alinhadas compostas por quartzitos pertencentes ao Grupo Natividade. Ao longo da sua zona de influência, as rochas encontram-se intensamente milonitizadas sob regime dúctil a dúctil-rúptil, formando pares S-C, além de apresentarem associações minerais hidrotermais que incluem turmalina, cianita e óxidos de ferro em determinadas localidades (Oliveira et al., 2012).

Os processos deformacionais e hidrotermais brasilianos foram de suma importância para a formação de várias ocorrências minerais com potencialidades econômicas na área. O Projeto Natividade (2012) identificou potencialidades para formações ferríferas e maganesíferas, rochas ornamentais, gemas, cerâmica, materiais para construção civil, abrasivos e cianita refratária, além dos depósitos de ouro (Figura 7). Estes depósitos e/ou ocorrências auríferas concentram-se em minas e garimpos, geralmente nas proximidades de povoados ou cidades.

As áreas com mineralização de ouro apresentam uma série de semelhanças entre si, ocorrendo ao longo das zonas de cisalhamento brasilianas e dispostas em veios de quartzo-carbonato sulfetados. As diferenças principais se dão no tipo de alteração hidrotermal da

rocha encaixante, pois estes processos variam de acordo com a composição química e reologia da rocha e com os mecanismos de precipitação de metais.

No depósito de Chapada de Natividade, a mineralização ocorre ao longo das rochas pegmatíticas da Suíte Xobó, provocando hidrólise de feldspatos e neoformação de epidoto e sericita, além de sulfetos. Neste depósito, datações Rb-Sr em micas de milonitos apontam a idade de mineralização em 517±40 Ma e estudos de inclusões fluidas reiteraram a natureza aquo-carbônica do fluido mineralizante, tendo sido identificadas também inclusões aquosas e carbônicas (Queiroz, 2001). No depósito de Serra de Natividade, há a alteração hidrotermal de rochas da sequência Água Suja. Sua composição mais rica em ferro provoca a neoformação de magnetita e hematita, além de carbonato, sericita, biotita e sulfetos (Oliveira et al., 2012; Corrêa et al., 2013).

O Depósito de Príncipe se destaca por ter se formado dentro de uma sombra de pressão de escala regional, bastante evidente em produtos geofísicos (Corrêa et al., 2014), que atua como uma zona de alívio favorável à deposição do ouro e outros metais. O Granito Príncipe, ao ser deformado, adquiriu morfologia sigmoide, com sombras de pressão sendo formadas nas suas extremidades norte e sul. Dentro da sombra de pressão norte, que é onde as ocorrências auríferas estão localizadas, há rochas em diferentes graus de alteração hidrotermal, onde protólitos ígneos vão gradualmente sendo alterados, culminando em veios de quartzo com mineralizações auríferas. Questões mais aprofundadas acerca do Depósito de Príncipe serão abordadas no Capítulo II.

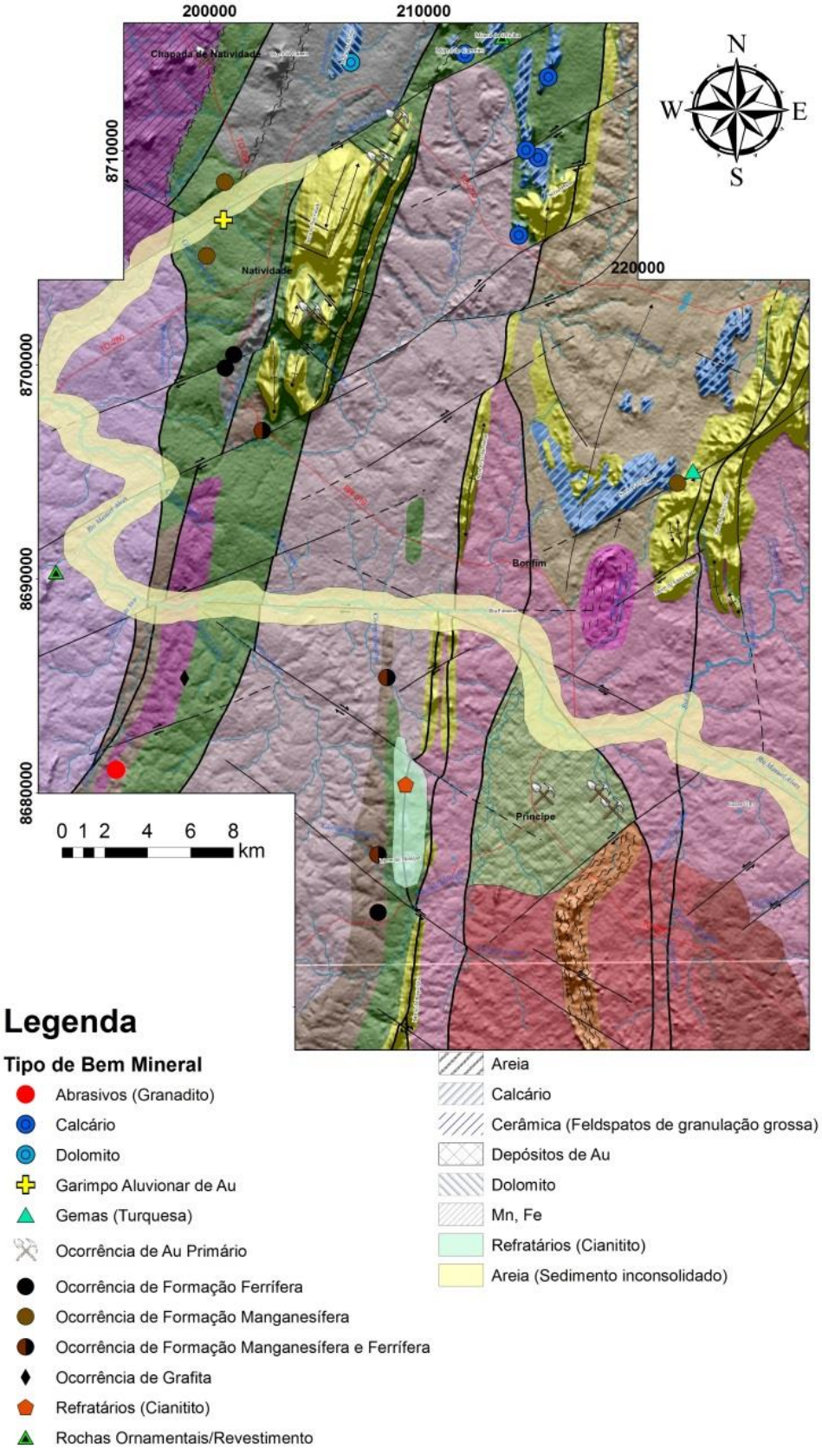

Figura 7. Mapa de potencialidades econômicas do Projeto Natividade (2012). Os depósitos e ocorrências auríferas ocorrem associados a zonas de cisalhamento em diferentes rochas. O Depósito Aurífero de Príncipe está destacado na extremidade norte do Granito Príncipe, dentro da área esverdeada.

CAPÍTULO II:

The Príncipe Orogenic Deposit, Brazil: Metallogenetic Implications and Exploration Guides for a Regional-Scale Pressure Shadow Gold Deposition Site

The Príncipe Orogenic Deposit, Brazil: Metallogenetic Implications and Exploration Guides for a Regional-Scale Pressure Shadow Gold Deposition Site

ABSTRACT

Situated in the Natividade Gold District, the Príncipe Gold Deposit was formed after the establishment of a regional strike-slip system during the Neoproterozoic Brasiliano Event. The area rocks, however, were dated by zircon U-Pb and Sm-Nd as Paleoproterozoic, providing an epigenetic character for this deposit. The local lithological association is constituted by the Rio do Moleque tonalitic-granodioritic suite that was intruded by the peraluminous Príncipe Granite. During the Neoproterozoic these units underwent greenschist facies metamorphism and deformational and hydrothermal events, forming metamorphic tectonites inside the Príncipe Granite and hydrothermalites at the granite's northern border, where the Príncipe Gold Deposit is located. Inside it, a strong structural control can be verified, with N-N20°E-trending brittle-ductile shear zones that are discernible at all scales of observation and end up as an interconnected pervasive system of discontinuous and anastomosed quartz-carbonate-sulfide-gold-veins.

Airborne gamma-ray spectrometric and magnetometric geophysical products helped to delimitate lithological boundaries and structures for this deposit. Gamma-ray images such as the RGB ternary composition highlight the Príncipe Granite's sigmoid shape, with a high K-eTh-eU signature. Two pressure shadows, one southern high-K and one northern high-eTh, are also evident, with the southern composed by pegmatites and the northern by hydrothermally altered granitoids, where the Príncipe Gold Deposit is located. These three lithologies assemble a dextral sigma-type kinematic object. High-K lineaments inside the Príncipe Granite can be identified at the K and Anomalous K images, corresponding to tectonites, defined as biotite-sericite-quartz-schists. In Matched Filtering and Euler Deconvolution analyses, anomalies at the Príncipe Granite's borders were identified and correlated to shear zones. Some N45°E-trending anomalies were also identified, corresponding to faults parallel to the regional Transbrasiliano Lineament Trend. These analyses also identified shallower EW-trending anomalies that were associated to younger brittle faults.

The shear zones played an important role for the deposit formation, acting as pathways that promoted a channelized fluid flow until the site of metal precipitation. Hydrothermal alteration processes in different grades can be verified along these structures, mainly characterized by primary minerals hydrolysis, originating a neoformed mineral assemblage. The Príncipe Granite acted as an obstacle for hydrothermalism and deformation, producing two pressure shadows that acted as structural traps for the ore. These structures, being stress release zones, concentrated the hydrothermal solution. They also changed the physicochemical conditions of the fluid through abrupt pressure reductions and an increase of the fluid-rock interaction rate, precipitating gold and other base metals.

Fluid inclusion studies indicate an aqueous-carbonic nature for the fluid with 5% NaCl equivalent weight and thermometric studies suggest that the gold mineralization occurred between 250°C and 400°C. The S, C and O stable isotopes indicate a metamorphic source for the fluid. Whole rock geochemistry and microprobe studies highlight hydrothermal alteration processes involving Fe, Ca, Mg, K, Na, Au, Ag metasomatism.

The Príncipe Gold Deposit belongs to the orogenic class, being distinguished from the other occurrences inside the Natividade Gold District and from most orogenic deposits of the world for its singular features, such as the regional-scale auriferous pressure shadow.

KEYWORDS: BRASÍLIA FOLD BELT, OROGENIC DEPOSITS, GOLD

1. INTRODUCTION

Since its initial proposal by Groves et al. (1998), the orogenic gold mineralization model changed some concepts concerning the mesothermal deposits type. For sixteen years, it has passed through several reviews and improvements (Goldfarb et al., 2005; Phillips & Powell, 2009; Phillips & Powell, 2010), being able to categorize and classify a lot of gold-only deposits across the world. Many of these works try to explain the mechanisms of gold extraction from source rocks and the processes involving the tectonic environment, structural control (Pirajno, 2010; Hronsky et al., 2012), gold transportation, endowment and deposition (Goldfarb et al., 2001; Frimmel, 2008).

This kind of deposits has a close relation to orogenesis (Groves & Bierlein, 2007) and supercontinent cycles (Barley & Groves, 1992; Cawood & Buchan, 2007; Goldfarb et al., 2010), where regional greenschist facies and compressive or transpressive regimes are established (Bierlein et al., 2006; Bierlein et al., 2009). These processes lead to the formation of aqueous-carbonic hydrothermal fluids that carry gold along sulfide complexes (Phillips & Evans, 2004; Stefánsson & Seward, 2004; Zezin et al., 2007). These solutions migrate vertically across the continental crust (Sibson, 1994; Sibson, 1996) until they reach a site of precipitation, where the fluid suffers abrupt physicochemical changes (Williams-Jones et al., 2009). The destabilization can be reached by processes like pressure and temperature lowering, reaction with host rocks, fluid mixing, rheological discontinuities and structural entrapment (Robb, 2005; Pirajno, 2009).

The main subject of this work is the Príncipe Gold Deposit, where the main control of gold deposition is a regional-scale pressure shadow formed in a strike-slip system. In order to better understand the metallogenetic mechanisms that led to the deposit formation, several techniques were applied to classify it and determine petrogenetic aspects, structures mapping, fluid migration paths and hydrothermal alteration processes.

2. REGIONAL GEOLOGIC SETTING

The study area is located in the Tocantins Structural Province (Figure 1), at the Northern Brasília Fold Belt (Almeida, 1981). This Province was established during Neoproterozoic events, when the Gondwana supercontinent was formed (Brito Neves & Cordani, 1991). During this orogenetic event, known as the Brasiliano Cycle (Fuck et al., 2005), a collision between the Amazonian and São Francisco cratons occurred (Pimentel & Fuck, 1992), originating the Brasília Fold Belt. This belt is divided in the Northern and

Southern sections (Araújo Filho, 2000), having been formed after a continuous accretion of blocks that were amalgamated and deformed (Pimentel et al., 1999).

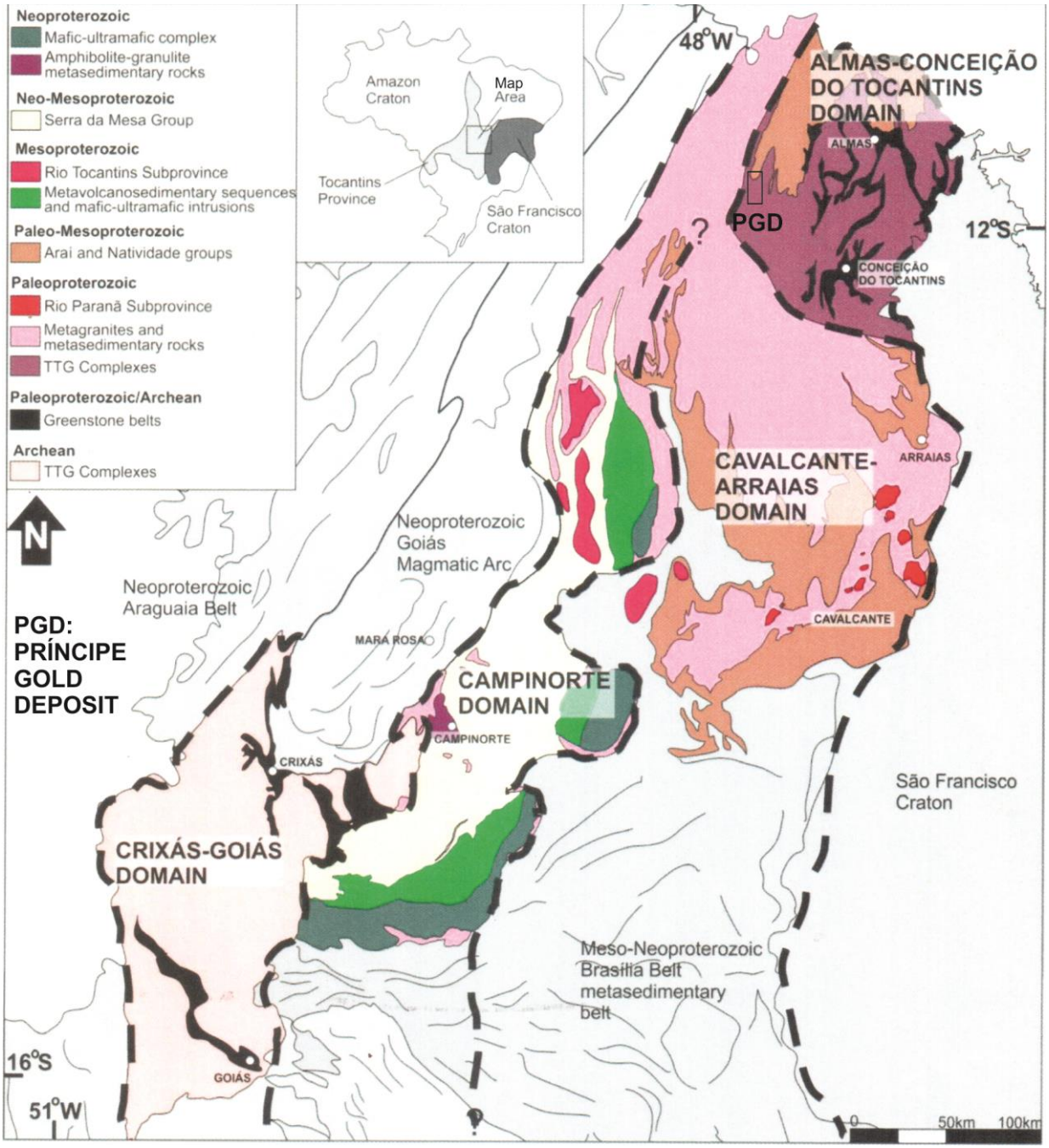

Figure 1: Brasília Fold Belt geological map extracted from Cordeiro (2014). The Príncipe Gold Deposit area is displayed at the Almas-Conceição do Tocantins Domain as the PGD rectangle inside the extreme north of the map. This Domain is characterized by a Paleoproterozoic lithological association of greenstone sequences and TTG complexes.

The Príncipe Gold Deposit (Figure 2) comprises an association of Rhyacian Paleoproterozoic rocks that belong to the Almas-Conceição do Tocantins Domain (Cordeiro, 2014). The Almas-Dianópolis terrane (Cruz & Kuyumjian, 1998) is part of this domain and is constituted by the Riachão do Ouro (Correia Filho & Sá, 1980) and Água Suja (Queiroz,

2001) metavolcanosedimentary sequences and by the Manuel Alves and Rio do Moleque tonalitic-granodioritic suites (Oliveira et al., 2012). This terrane is intruded by rocks correlated to the Aurumina suite (Botelho et al., 1999) that belongs to the Cavalcante-Teresina de Goiás-Campos Belos-Nova Roma area (Botelho et al., 1995; Botelho et al., 1998). Recent works (Fuck et al., 2014) show that these intrusions extend to the north, named as the Cavalcante-Natividade crustal block. This suite is characterized by a peraluminous granitoid assemblage with U-Pb zircon ages between 2.12 and 2.17 Ga formed by crustal melting during syn- to post-collisional events (Botelho et al., 2006). The lithological associations that belong to this terrane and occur in the area of study are the Xobó granitic-pegmatitic suite (Gorayeb et al., 1988) and the Príncipe Granite (Oliveira et al., 2012). The metasedimentary covering of this basement occurs by unconformities and is constituted by the Natividade and Serra da Mesa Groups (Gorayeb et al., 1988; Saboia, 2009; Marques, 2009), deposited during Staterian taphrogenic events (Brito Neves et al., 1995).

During the Brasiliano Cycle, a transcurrent system was developed in the area, characterized by NS-trending brittle-ductile to ductile shear zones of high dip angle (Kuyumjian & Araújo Filho, 2005). This system is part of the Transbrasiliano Lineament (Schobbenhaus et al., 1984; Fuck et al., 1994), a regional-scale structure of thousands of kilometers that has several metallogenetic implications for the region (Cruz & Kuyumjian, 1999; Queiroz, 2001; Kuyumjian et al., 2012). The intense hydrothermal fluid flow inside the shear zones, associated with regional deformation and greenschist facies metamorphism led to the alteration of the Paleoproterozoic rocks of the area. The different grades of mylonitization and hydrothermalism originated a Neoproterozoic neoformed paragenesis, forming rocks that will be referred in this work as tectonites for the high deformation bands inside the Príncipe Granite and hydrothermalites for the hydrothermally altered granitoids of the deposit (Oliveira et al., 2012).

There are several gold deposits and occurrences located around the city of Natividade, such as Chapada de Natividade (Queiroz, 2001), Serra de Natividade, Geominas and Príncipe. They share many features in common, typically occurring along shear zones and being hosted in quartz±carbonate veins. The age of mineralization by Rb-Sr in secondary biotites is 517±40 Ma (Queiroz, 2001), showing that the gold emplacement happened at the final stages of the Brasiliano Cycle (late orogenic). These lode gold deposits are part of the Natividade Gold District (Corrêa et al., 2013), comprised by deposits correlated to the orogenic gold deposits model (Groves et al., 1998).

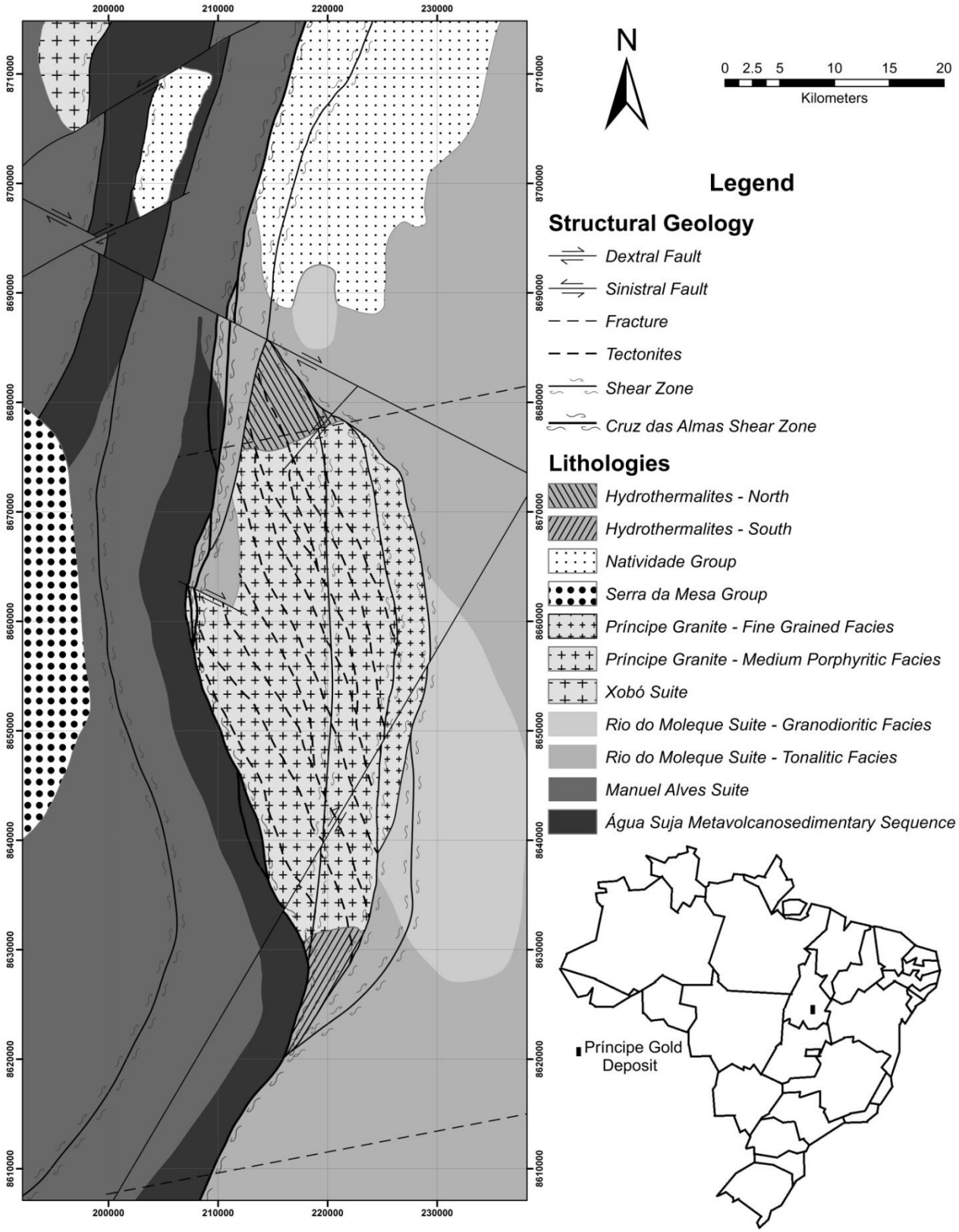

Figure 2: The Príncipe Gold Deposit simplified geological map, made after IBGE (2007), Oliveira et al. (2012) and Abdallah & Meneghini (2013). The Príncipe gold deposit is located at the northern dashed area, a zone characterized by hydrothermally altered granitoids.

3. METHODS

3.1 Geophysics

The airborne gamma-ray spectrometric and magnetometric data that cover the study area were obtained from the Tocantins Aerogeophysical Project. The flight lines were spaced 0.5 km from each other with NS direction, while the control lines orientation was EW, with a spacing of 10 km. The average flight height was 100 m and the medium speed was 270 km/h (AGP-LA, 2006). The geophysical data was processed using the GEOSOFT Oasis Montaj 8.0 software at the Laboratory of Applied Geophysics in the University of Brasília.

This software helped create magnetometric images such as the Anomalous Magnetic Field (AMF), Vertical Derivative (dZ), Analytical Signal Amplitude (ASA) and Tilt Derivative (TDR), obtained from geophysical formulas (Roest et al., 1992; Miller & Singh, 1994; Blakely, 1995). Further analyses by Matched Filtering (Phillips, 1997; Phillips, 2001) and Euler Deconvolution (Thompson, 1982; Reid et al., 1990; Barbosa et al., 1999; Barbosa & Silva, 2005) were performed to identify how the magnetic anomalies behave in different depth intervals. The Matched Filtering processing obtained depths of 177, 462, 1723 and 11340 m, and the Euler Deconvolution processing used the structural index of 1.5 to identify unidimensional (linear) and bidimensional (planar) structures at depths up to 3 km.

Using the gamma-ray spectrometric data, the K, eTh and eU and the RGB ternary composition images were created to delimitate areas of different compositions (Jacques et al., 1997; Blum et al., 2003). Further processing generated the anomalous K image (Pires, 1995), through correlations between K and ASA, eTh and eU/eTh products. The multiple regressions technique (Davis, 1973; Fianco et al., 2012) produced the formula $K = 0.143 – 0.874*ASA + 0.0275*eTh + 0.825*(eU/eTh)$, aiming to identify K concentrations above the crustal average (2.3%).

3.2 Geochemistry

The samples were pulverized and analyzed at the ACME Analytical Laboratories LTD., using an ICP-ES to determine the proportions of the major elements (oxide wt%) and an ICP-MS for the trace elements (gold in ppb and the rest in ppm). The granitic rocks had low loss on ignition (LOI) values, generally <2%, while the neoformed rocks reached higher values, up to 4.1% (Tables 1-3).

Petrochemical studies were applied to the granite samples to determine the tectonic setting where they formed and their geochemical signature (De La Roche et al., 1980; Pearce et al., 1984; Chappel & White, 2001; Frost et al., 2001). For the tectonites and hydrothermalites, binary diagrams were made to identify compositional changes that show

processes of mobility, loss and gain of elements (Zhu et al., 2011; Alyiari et al., 2014). In order to verify these processes, the neoformed samples were compared to the granite samples, since they preserve their original chemical composition.

3.3 Geochronology

The zircon U-Pb analyses (Tables 4-7) were performed at the Geochronology Laboratory of the University of Brasília using a Multicollector LA-ICP-MS Thermo-Finnigan Neptune coupled to a 213 nm New Wave laser and the obtained data led to the creation of Concordia diagrams with the Isoplot 4.15 software (Ludwig, 2008).

The Sm-Nd samples (Table 8) were also analyzed at the Geochronology Laboratory of the University of Brasília using a TIMS Triton Plus, and then the ℇNd at the time of crystallization was calculated (Allègre, 2008) using the U-Pb ages obtained for the Príncipe Granite (2.16 Ga) and the age of 0.52 Ga (Queiroz, 2001) for the tectonites and quartz veins.

There were some difficulties concerning the geochronological analyses. In the U-Pb analyses, most of the zircon grains were highly discordant, leaving only a few crystals with ratios and ages with concordances between 90% and 110%. For the Sm-Nd analyses, the hydrothermalites and tectonites data seem to have been affected by a rare earth elements (REEs) metasomatism, presenting much older model ages than the ones from the Príncipe Granite. The main cause of these problems is related to sampling difficulties, since the deposit rocks are usually highly altered by processes of weathering, hydrothermalism and/or deformation.

3.4 Stable Isotopes

For the S isotopes (Table 9), selected pyrite grains were analyzed at the Geochronology Laboratory of the University of Brasília using a Multicollector LA-ICP-MS Thermo-Finnigan Neptune coupled to a 213 nm New Wave laser with the reference standard IAEA-S1 (Ding et al., 2001 apud Bühn et al., 2012).

The C and O isotopes samples (Table 10) were analyzed using a Delta V Advantage connected to a Gas Bench II apparatus at the Geochronology Laboratory of the University of Brasília. The reference standards used were the VPDB for the C and O isotopes and the VSMOW for the O isotopes (Coplen, 1994).

A general difficulty involving these studies is the low amount of certain rocks or minerals that could be used in analytical procedures, such as carbonate veins and sulfide grains. These problems tend to preclude larger scale studies in the area, limiting them to restricted outcrops and samples.

3.5 Microprobe Analyses

The analyses were performed in the Electron Microprobe Laboratory of the University of Brasília using a JEOL JXA-8230 operating at 20kv and 20 nA. A total of 233 spots were analyzed in silicate, carbonate (Tables 11-16) and sulfide (Table 17) crystals. The data is presented in oxide wt% for the silicates and carbonates and in element wt% for the sulfides. From the obtained mass proportions the amount of atoms per formula unit (apfu) was calculated for each mineral (Deer et al., 2013).

In order to determine the compositional variations of the igneous minerals of the Príncipe Granite, the neoformed phyllosilicates of the tectonites and the metasomatized assemblage of the hydrothermalites, three groups of samples were analyzed. Two thin sections of the Príncipe Granite were used to analyze the composition of K-feldspar, plagioclase, muscovite, biotite and garnet. Two tectonite samples were selected to determine the differences between the primary and secondary varieties of muscovite, sericite and biotite. Four hydrothermalite samples containing carbonate, K-feldspar, plagioclase, biotite, chlorite, sericite, pyrite, chalcopyrite, galena, pyrrhotite and native gold were also analyzed.

3.6 Fluid Inclusions

The analyses were performed at the Fluid Inclusions Laboratory of the University of Brasília, where petrographic, mapping and microthermometric studies of the inclusions were made. The samples were analyzed on an Olympus BX 50 microscope coupled to a Linkam THMSG 600/TMS 93 plate and a LNP 2 cooling system. The plate was calibrated by measuring the ice melting and total homogenization temperatures (Tmice and Thtot) of an artificial standard of pure aqueous inclusions and then comparing them to the theoretical values of 0°C and 383.5°C, respectively. The obtained Tmice and Thtot were 0°C and 374.1°C, generating a correction factor of 0.975489 that was applied to the Thtot data. After the microthermometric analyses, some parameters of the fluid at the time of entrapment were calculated using the FLUIDS software (Bakker, 2003). This software helped determine fluid density (Zhang & Frantz, 1987), salinity (Bodnar, 1993), pressure (Roedder & Bodnar, 1980; Shepherd et al., 1985) and build isochores specifically for the system (Table 18).

The petrographic and microthermometric observations were difficult due to the intense recrystallization and fracturing of the veins and the tiny size of the inclusions that were rarely bigger than 20 µm. This fact had been reported by Queiroz (2001) in studies at the Chapada de Natividade deposit.

4. PRÍNCIPE GRANITE AND SURROUNDING ROCKS GEOLOGY

The Príncipe Granite (Figure 2) is an intrusive igneous body inside the basement rocks and is characterized by its homogeneous mineralogy and heterogeneous texture and deformational aspects. This lithology is leucocratic, phaneritic, holocrystalline, with medium to coarse grain size and porphyritic texture. At the eastern border of the granite, the rock presents a fine to medium equigranular facies with a distinct geophysical signature. The adjacent rocks constitute a granodioritic to tonalitic assemblage defined as the Rio do Moleque suite (Oliveira et al., 2012).

At the gamma-ray spectrometric images (Figure 3), the Príncipe Granite appears as a dextral sigmoid-shaped body. In the RGB ternary compositions the medium porphyritic facies is white colored and has a high K-eTh-eU response, while the fine grained facies is red colored and has a high-K signature. At the K, eU and eTh images, the granite's shape and limits can still be identified, presenting different responses at the pressure shadows. The granite presents low frequency and small amplitude anomalies on the magnetometric images (Figure 4), with the high signals being associated to structures, such as faults and shear zones. The Rio do Moleque suite presents low to medium K-eTh-eU values and medium to high magnetic anomalies.

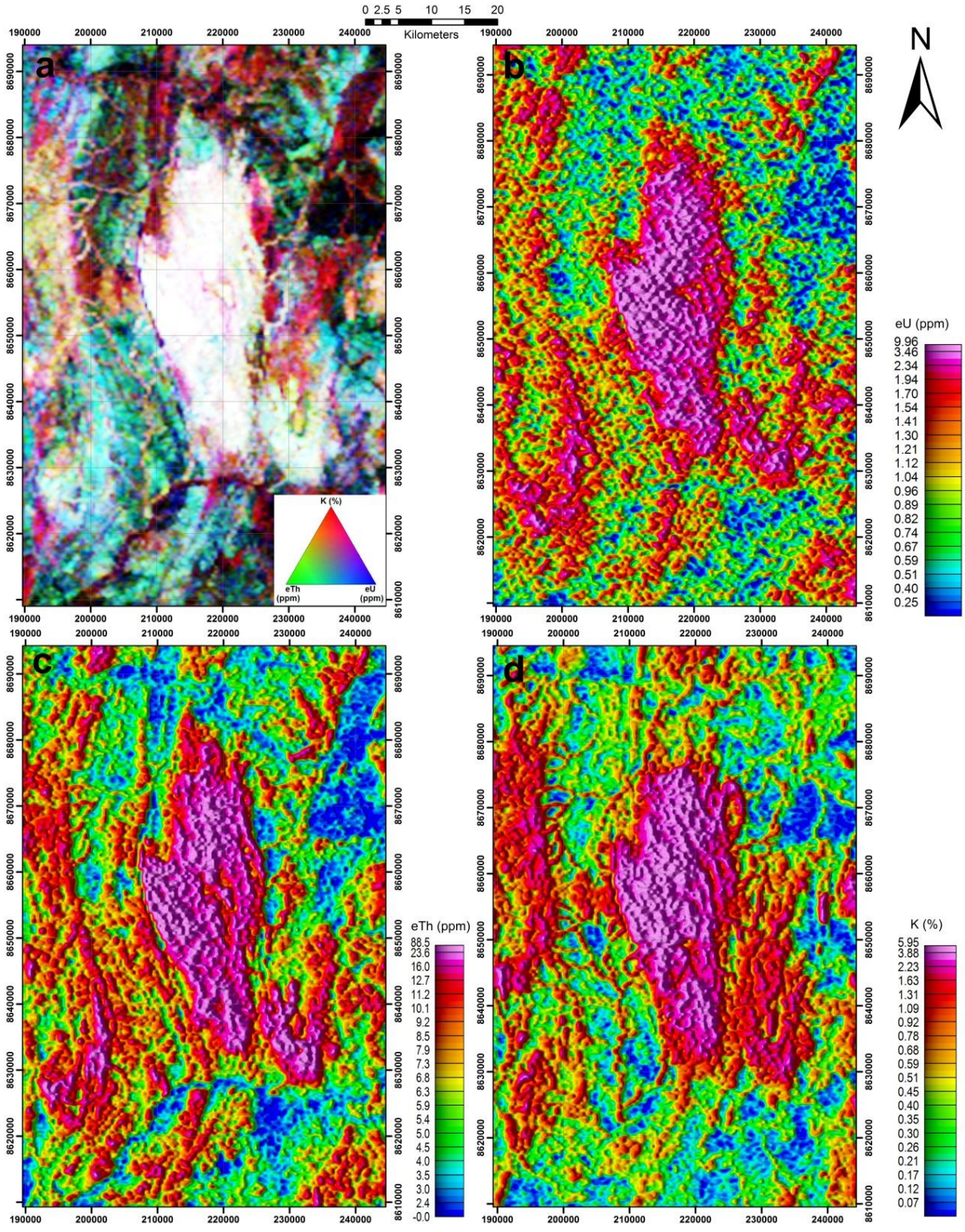

Figure 3: Airborne gamma-ray spectrometry images. These products are useful to identify and delimitate domains based on the lithologies' K, eTh and eU contents. a: RGB ternary composition showing the white-colored Príncipe Granite with its green-colored northern and red-colored southern pressure shadows. b: eU image pointing the Príncipe Granite's high eU values. The pressure shadows still preserve their shapes with medium values, while the Rio do Moleque Suite is characterized by low eU contents. c: eTh product showing the Príncipe Granite's high values along with its northern pressure shadow. The southern pressure shadow and the Rio do Moleque Suite present low eTh contents. d: K image highlighting the Príncipe Granite's high-K contents. The northern pressure shadow is poor in this element, while the southern presents medium values. Inside the granitic body, some high-K lineaments can be verified in this product, which correspond to tectonites' bands.

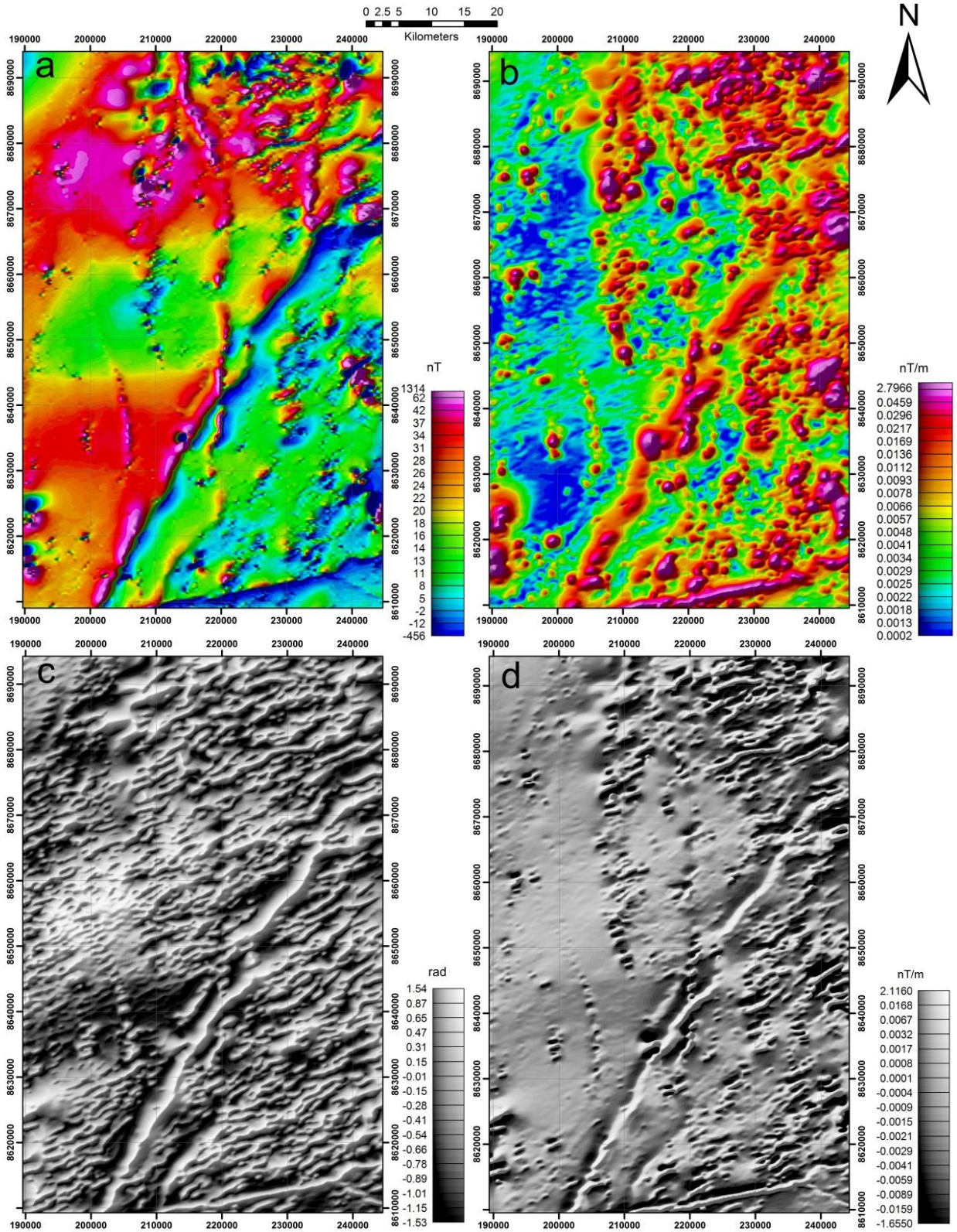

Figure 4: Airborne magnetometric images. The Anomalous Magnetic Field (a) and Analytical Signal Amplitude (b) products were used to locate and centralize anomalous bodies. In these images the Príncipe Granite and its pressure shadows present low values at their centers while their borders have high values due to shear zones. The Tilt (c) and Vertical (d) derivatives were used to identify and trace anomalous lineaments correlated to NS-trending shear zones and N45°E-trending faults.

Petrographic studies show that the minerals that constitute the porphyritic texture of the Príncipe Granite are mainly K-feldspar phenocrysts along with a minor contribution of coarse grained plagioclase and muscovite. These phenocrysts occur inside a fine to medium grained matrix of quartz, plagioclase, muscovite, biotite and garnet (Figures 5 and 6). According to the classification of Le Bas & Streckeisen (1991), the rock is defined as a syenogranite with some monzogranitic and alkali-granitic portions. The typical accessory minerals are zircon, apatite, allanite and leucoxene, appearing as an alteration product of ilmenite. The K-feldspar occurs as orthoclase and inverted orthoclase and frequently presents perthitic exsolutions. The plagioclase composition is mainly albitic, with less than 5% anorthite (An) and is less abundant than the K-feldspars. The muscovite shows a discrete pleochroism, suggesting enrichment in Ti. Both micas and garnet are igneous and occur in equilibrium, which implies a peraluminous nature of the Príncipe Granite.

The Rio do Moleque suite rocks are characterized by mylonites formed by leucocratic quartz-feldspar and biotite-rich melanocratic bands. The main mineralogy is constituted by quartz, plagioclase and biotite, with minor proportions of K-feldspar, carbonate, chlorite and epidote. Most of the biotite, chlorite, carbonate and epidote appear as alteration products, formed after the Brasiliano Cycle hydrothermal and deformational events.

Figure 5: Macroscopic plate for the Rio do Moleque granitoids and the Príncipe Granite. a-b: Rio do Moleque rock samples. They appear much more deformed than the Príncipe granite and present higher plagioclase and biotite concentrations. c: Typical Príncipe Granite outcrop, extending for many kilometers. d: Sample of the medium porphyritic facies of the Príncipe Granite, with coarse feldspar phenocrysts. e: Sample of the fine grained facies of the Príncipe Granite, mainly characterized by its fine to medium equigranular texture. f: Medium porphyritic facies sample with feldspar and muscovite phenocrysts.

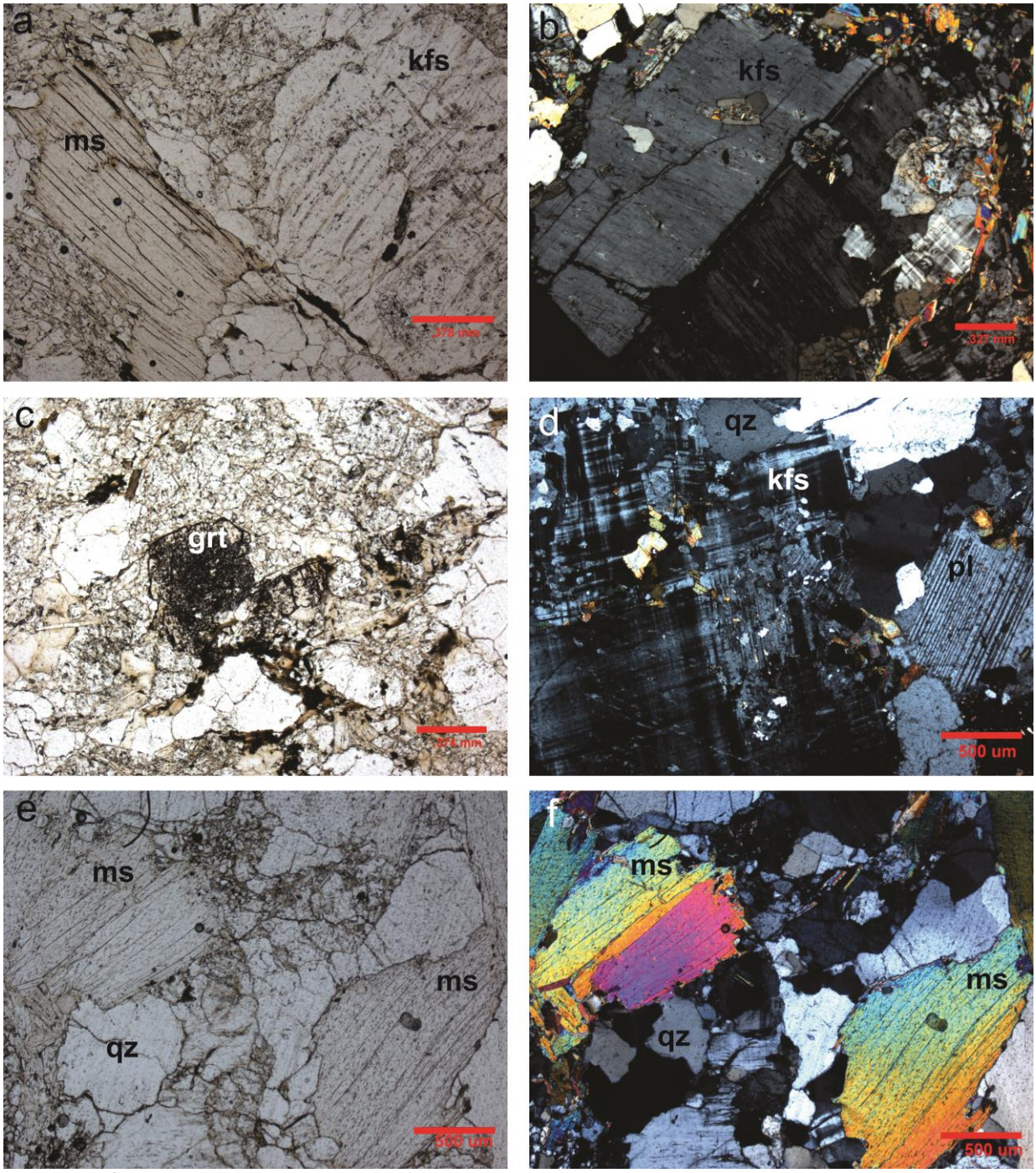

Figure 6: Príncipe Granite micrographs. a: K-feldspar and muscovite phenocrysts. b: Orthoclase phenocryst showing a perthitic exsolution. c: Igneous garnet grain. d: Inverted orthoclase and plagioclase grains. e-f: Muscovite phenocrysts inside the quartz-feldspar matrix. The mineral abbreviations are displayed according to Whitney & Evans (2010).

In microprobe studies, most of the Príncipe Granite petrographic evidences were confirmed. The analyzed K-feldspar shows high-K and low-Ca contents (Or_{92-97}). The plagioclase has high-Na and low-K contents ($Ab_{96.5-98}$). Two garnet groups were identified, with one being richer in Fe ($Alm_{40-44}Grs_{40}$) and the other in Ca ($Alm_{29-34}Grs_{48-55}$). Both garnet groups have Mn values between 13 and 15%, which suggests that they are magmatic (Miller & Stoddard (1981) apud Dahlquist et al., 2007; Deer et al., 2013). The muscovite and biotite microprobe data will be discussed later on the Gold Mineralization section.

Due to the fact that the Príncipe Granite has a higher rheological competence than the adjacent lithologies, it offered more resistance to deformational events, acting like a dextral sigma-type kinematic object (Figure 2). The deformation inside the granite was heterogeneous, since in some places there are no signs of it, with primary magmatic textures and structures preserved, while at other sites intense mineral neoformation and recrystallization occurred, producing granitic schists (Figure 7). They are constituted essentially by quartz, biotite and sericite and mark high deformation bands inside the Príncipe Granite, being referred in this work as tectonites. In geophysical products, they appear as NS-N30°W-trending high-K ridges in the gamma-ray spectrometric K (Figure 3) and anomalous K (Figure 8) images, but have little expression in magnetometric images.

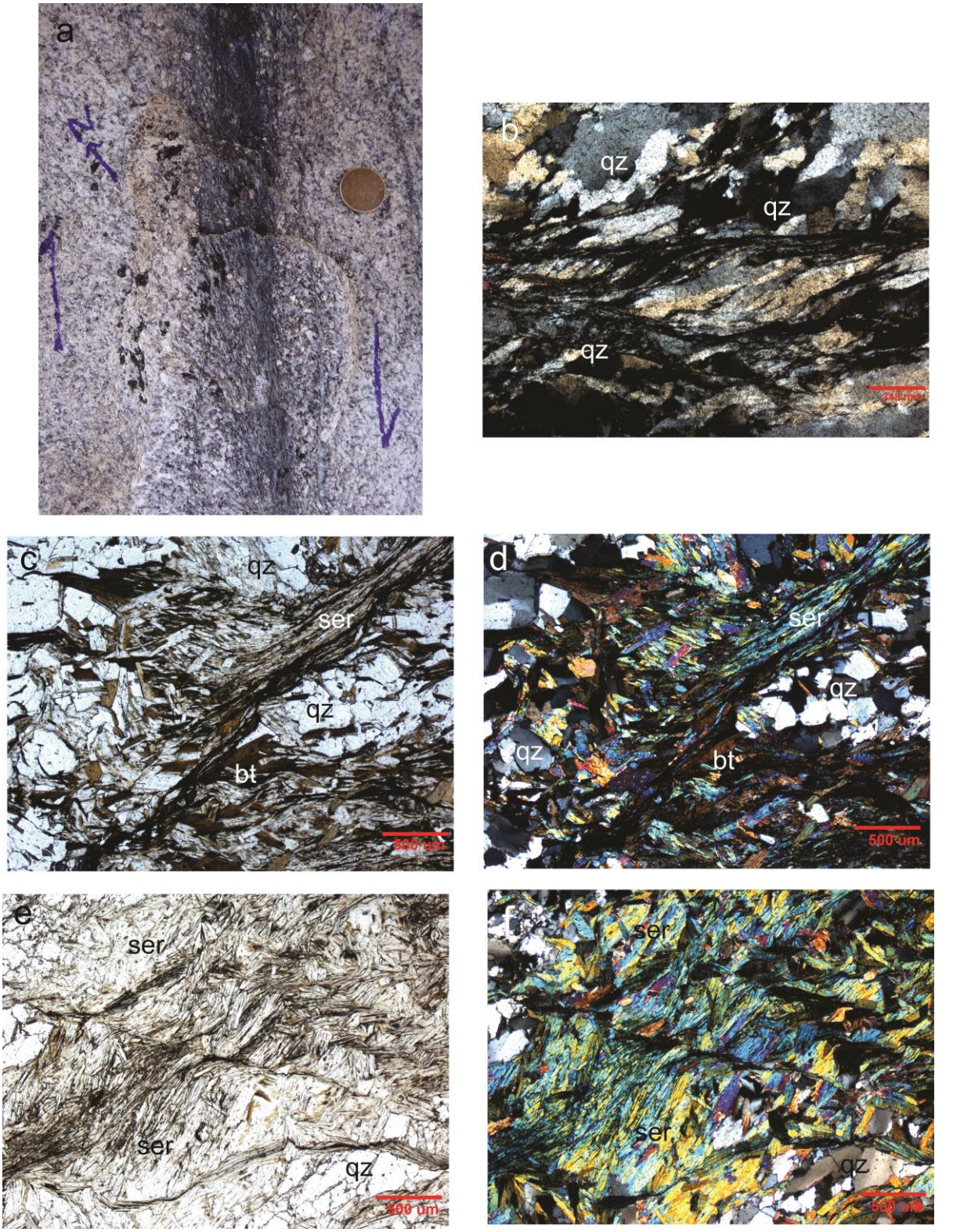

Figure 7: Tectonites plate. a: Minor-scale dextral N20°E-trending shear zone inside the Príncipe Granite. At the external portion of the photo, the granite is preserved. At the high deformation band borders, the quartz and feldspar grains start to rotate, stretch and recrystallize. Inside the shear zone, tectonite constituted by quartz, sericite and biotite is formed. b: Micrograph of a quartz segregation along the Cruz das Almas shear zone. The recrystallized quartz grains present sutured contacts and S-C mylonitic foliation. c-d: Tectonite micrograph detail where the lepidoblastic sericite and biotite bands are cut by a dextral microscopic shear zone. e-f: Other tectonite sample showing sericite lamellae being truncated by the shear zone. The mineral abbreviations are displayed according to Whitney & Evans (2010).

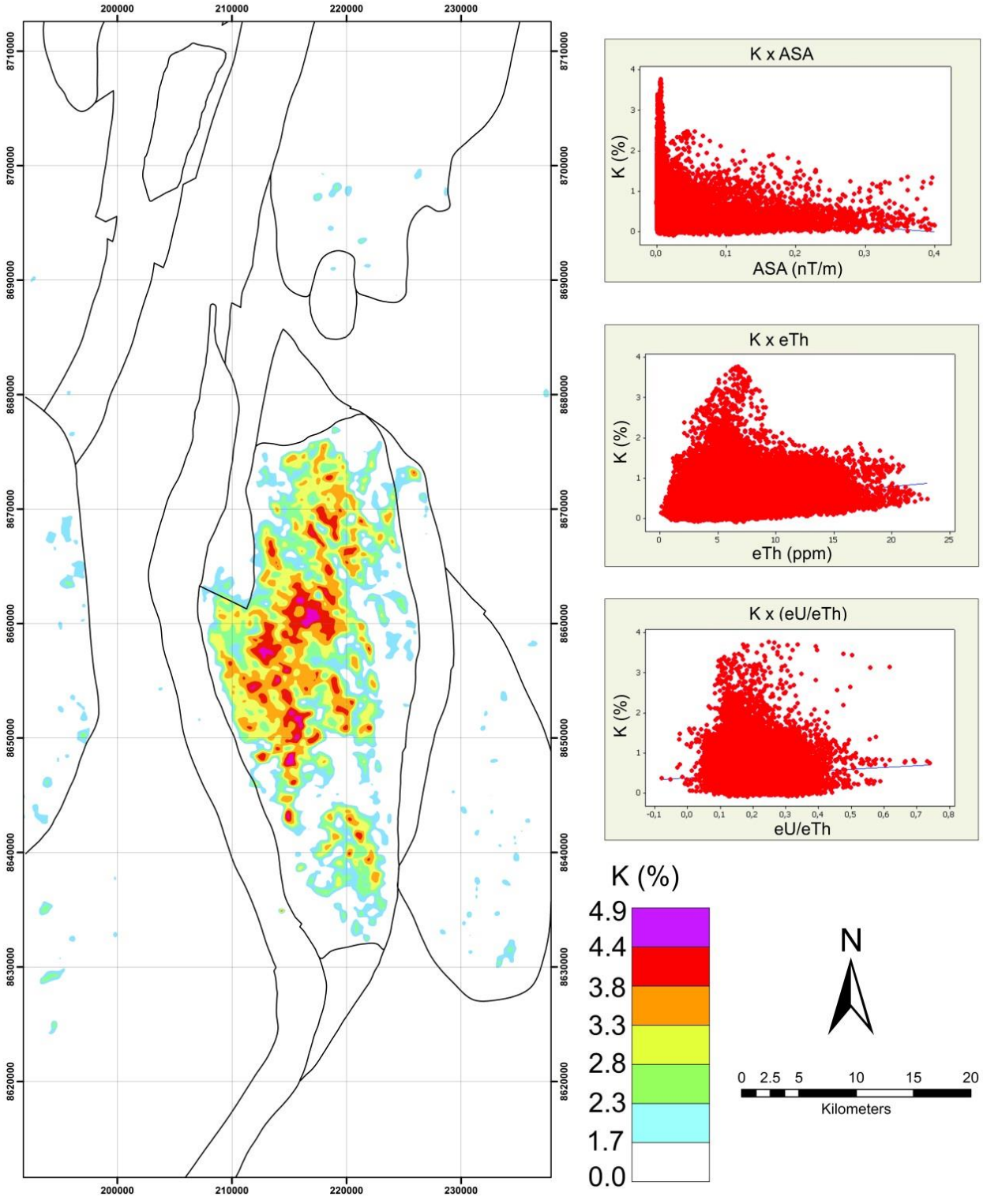

Figure 8: Anomalous K image along with the KxASA, KxeTh and Kx(eU/eTh) graphics used for making the correlation formula. All values above 2.3% show K-enriched areas and most of these regions occur inside the Príncipe Granite domain. Some of the high-K values appear as ridges, representing the biotite-sericite-quartz-tectonites' high deformation bands.

In map scale observations (Figure 2), the Príncipe Granite is bordered by two N10°W-N30°E-trending shear zones and cut by a NS-trending shear zone. These structures affect the nearby rocks and frequently form kilometric quartz segregations, marked by elongated, aligned, discontinuous and amalgamated hills. The main shear zone of the area is the one at the Príncipe Granite's western border, named Cruz das Almas shear zone. It is hundreds of km wide and was interpreted as a suture zone, tectonically dividing the Manuel Alves and Rio do Moleque suites (Oliveira et al., 2012; Sousa & Oliveira, 2013).

The area's faults and fractures represent brittle to brittle-ductile elements of the transcurrent system. Four main fault families were identified at all scales of observation, with N50°W-N30°W, N10°W-N20°E, N30°E-N50°E and N70°E-EW trends. The N10°W-N20°E group is parallel to the regional foliation trend and to the main dextral shear zones. The N50°W-N30°W and N30°E-N50°E families are orthogonal to each other and are also dextral. It was not possible to determine the temporal sequence of the fault families by cut relations, since they often are cut by each other. The N70°E-EW family, however, crosscuts all the other families and is sinistral, being the youngest group of structures (Figure 9).

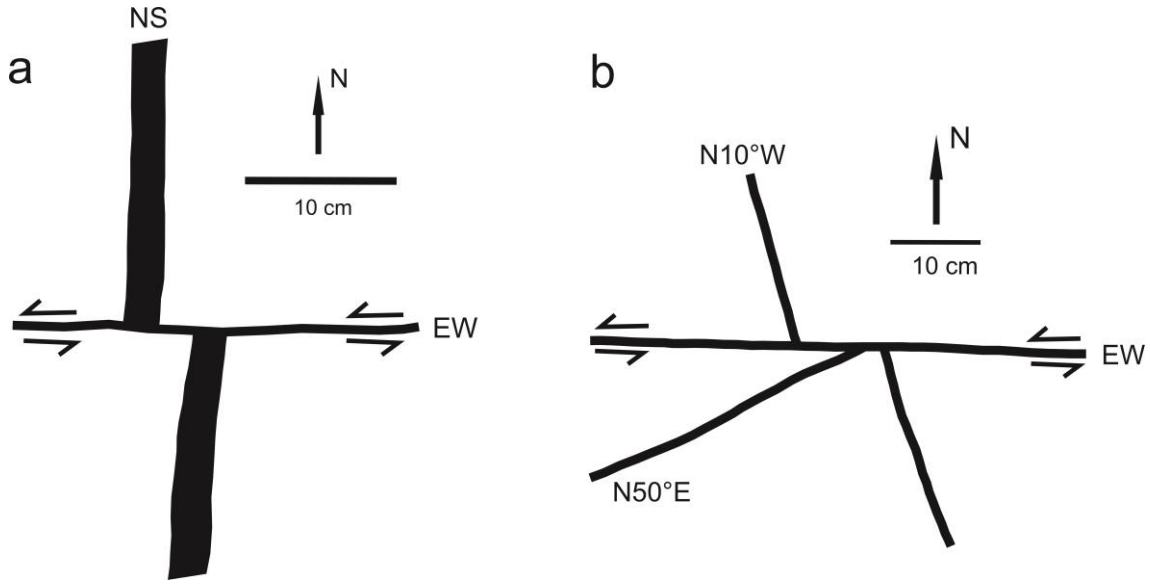

Figure 9: Príncipe Granite's faults and fractures system seen at outcrops. The structural trends were correlated to the Riedel system. a: NS-trending quartz vein cut by a sinistral EW fault. b: Sinistral EW fault crosscutting the N10°W and N50°E fractures.

These structures can be easily identified in the magnetometry products (Figure 4). At the dZ and ASA images the larger scale shear zones appear as high NS-trending anomalies, as well as EW and N30°E faults. Further magnetometric processing was made to examine how these structures behave in depth. At the Matched Filtering analyses (Figure 10), it can be seen that at depths up to 1723m the main lithologies and structures are still evident, while at 11340m the only remaining feature is the N45°E anomaly trend.

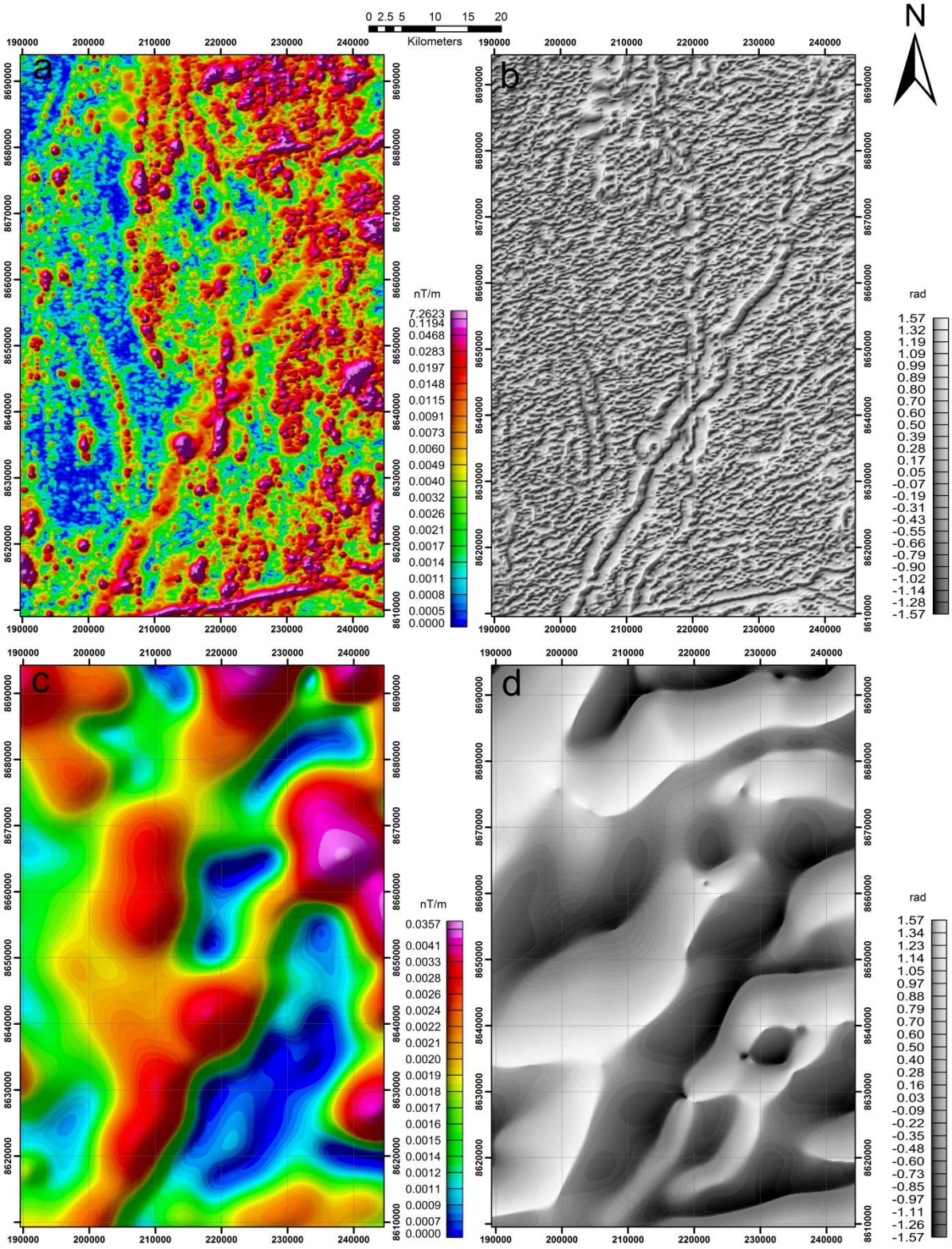

Figure 10: ASA and TDR images obtained by the Matched Filtering processing for the depths of 462 and 11340 m. The high-frequency anomalies are preserved at shallower depths, while at bigger depths the only remaining features are the N30°E lineaments, correlated to the regional Transbrasiliano Lineament trend.

4.1 Whole Rock Chemistry

For the geochemical studies, 25 deposit samples were analyzed, including ten of the Príncipe Granite, four of the tectonites and eleven of the hydrothermalites (Tables 1-3). These analyses show that this lithology is classified as a syn-tectonic peraluminous S-type granite with its origin associated to continental collision tectonics (Figure 11). The granite plots at intermediary fields between the alkalic and calcic trends. In REEs spidergrams (Figure 12), the granite shows enrichment in light REEs (LREEs), a strong Eu anomaly, and low contents of heavy REEs (HREEs). The Príncipe Granite geochemical data are correlated to what was described by Abdallah (2011) as the peraluminous series of the granite-gneiss basement. When compared to the Aurumina suite data (Alvarenga et al., 2007), the Príncipe Granite shows petrographic and geochemical similarities to the PP2γ2au1 (muscovite-granite) and PP2γ2au2 (biotite-muscovite-granite) facies.

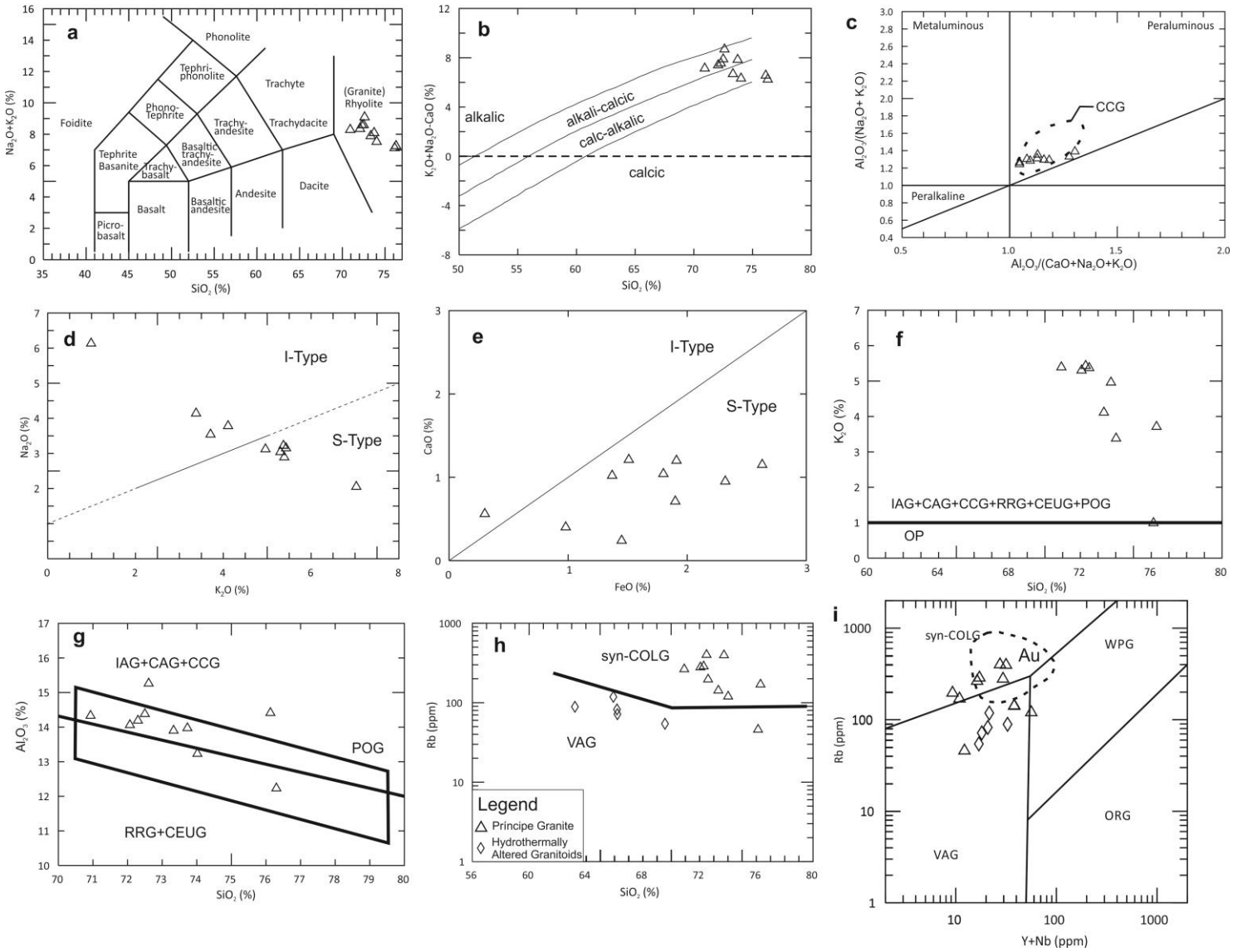

Figure 11: Príncipe Granite and hydrothermalites geochemical diagrams. The terms and abbreviations are extensively used in the literature for granitoids classification, where I-type stand for Igneous-derived, S-type for Sedimentary-derived, IAG for Island Arc, CAG for Continental Arc, RRG for Rift-Related, CEUG for Continental Epeirogenic Uplift, POG for Post-Orogenic, OP for Oceanic Plagiogranites, syn-COLG for syn-Collisional, VAG for Volcanic Arc, WPG for Within Plate and ORG for Ocean Ridge granitoids. a: TAS diagram (Le Bas & Streckeisen, 1991), classifying it as a granite. b: Modified Alkali Index (Frost et al., 2001), showing that the points plot between the alkali-calcic and calc-alkalic fields. c: Aluminum saturation index (Shand, 1943) highlighting the Príncipe Granite's peraluminous nature and classifying it as a CCG. d-e: Diagrams extracted from Chappel & White (2001) that classify the Príncipe granite as a S-Type granite. f-g: Major elements granitoid tectonic discrimination diagrams (Maniar & Piccoli, 1989) highlighting the continental collision granitoid (CCG) geochemical signature of this rock. h-i: Trace elements diagrams for the definition of the Príncipe granite's and hydrothermalites' tectonic setting (Pearce et al., 1984). While the Príncipe Granite is classified as a syn-collisional granite (syn-COLG), the hydrothermally altered granitoids present a volcanic arc signature. At the i diagram, the Aurumina suite field is presented inside the dashed circle, showing that these lithologies have common characteristics not only for major, but also for minor elements.

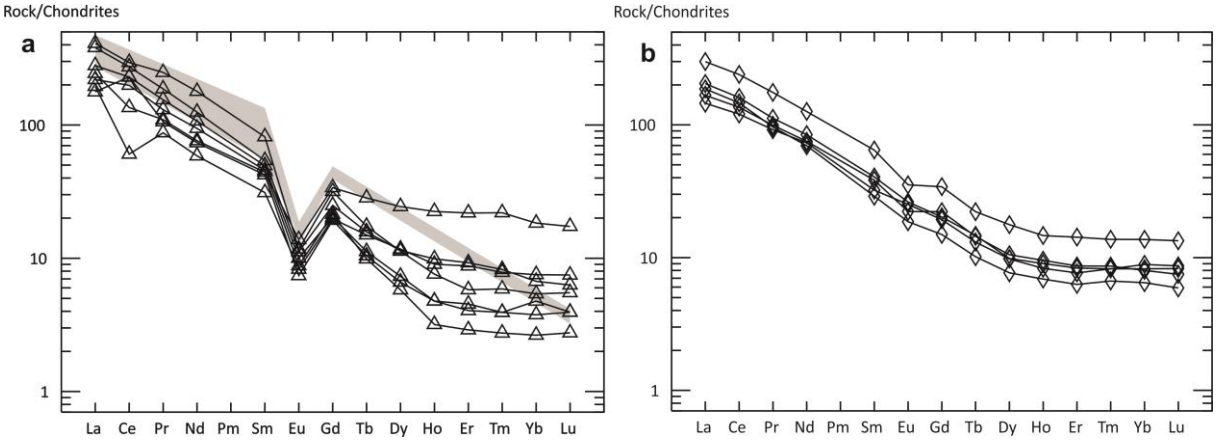

Figure 12: REEs spidergrams normalized to the chondrite (Sun & Mcdonough, 1989) for the Príncipe Granite (a) and the hydrothermalites (b). a: The gray area corresponds to the Aurumina suite data extracted from Alvarenga et al. (2007), presenting similarities with the Príncipe Granite data. b: The hydrothermally altered granitoids present more balanced HREEs and LREEs concentrations than the Príncipe Granite, suggesting that they were not originated from this lithology.

4.2 Geochronology

The age of crystallization of the Príncipe gold deposit rocks by U-Pb in zircon grains was determined by analyses of 4 granitoid samples, with one belonging to a hydrothermally altered granitoid, one to the fine grained facies of the Príncipe Granite and two corresponding to the medium porphyritic facies (Tables 4-7). The Príncipe Granite data (Figure 13) point two distinct ages for the medium porphyritic and the fine grained facies. Ages of 2346 ± 130 Ma and 2284 ± 120 Ma were indicated for the medium porphyritic facies, while the fine grained presented a younger age of 2169 ± 42 Ma. This age discrepancy may be explained by analytical problems, since most of the zircon grains were highly discordant and only a few were used to produce the Concordia diagrams. The obtained ages are compatible with the Aurumina suite data (Alvarenga et al., 2007; Abdallah & Meneghini, 2013) and are associated with the Transamazonic cycle, a global-scale Paleoproterozoic orogenetic event (Brito Neves et al., 1996). The analysis of one sample of a hydrothermally altered granitoid (Figure 13) inside the pressure shadow zone points the age of 2472 ± 64 Ma. This is the oldest age obtained for the deposit and it suggests that most of the pressure shadow area corresponds to a hydrothermalized domain of the Rio do Moleque suite, since it is older than the Granite.

The Sm-Nd model ages (T_{DM}) and source (ε_{Nd}) of the rocks was determined by the analyses of ten samples, five from the Príncipe Granite, two from the tectonites and two from the hydrothermalites (Table 8). The hydrothermalite samples correspond to quartz veins. The Príncipe Granite Sm-Nd data (Figure 14) show ε_{Nd} (T=2.16 Ga) values between -2.17 and 0.26 and T_{DM} between 2.28 and 2.58 Ga, indicating a Paleoproterozoic source for the magma with low crustal reworking. The acquired data are close to the Aurumina suite values (Fuck et al., 2014), suggesting that the rock was originated from continental crust melting. Although

the Sm-Nd data for the hydrothermalites and tectonites are not very reliable due to a probable REEs metasomatism, the negative ε_{Nd} and older T_{DM} values lead to the conclusion that these rocks were formed after the chemical remobilization of older crustal rocks.

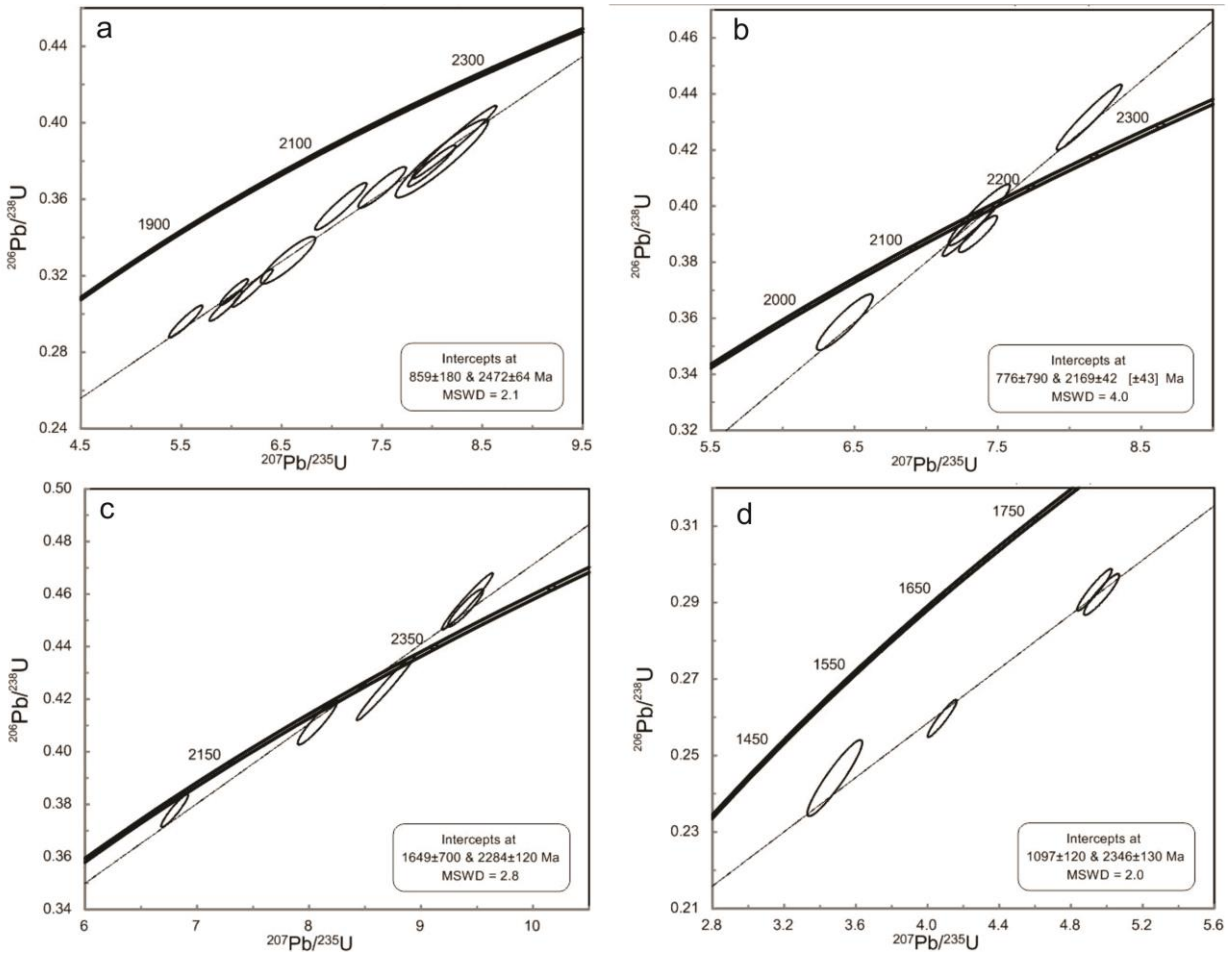

Figure 13: U-Pb Concordia diagrams for a hydrothermally altered granitoid (a) and the Príncipe Granite's fine grained (b) and medium porphyritic facies (c-d) samples. The four analyzed samples show Paleoproterozoic ages, being correlated to the deposit's basement rocks.

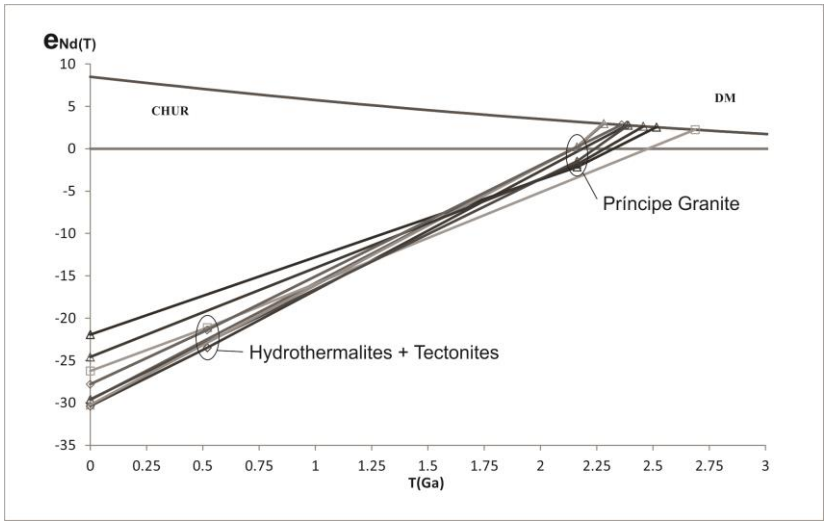

Figure 14: ε_{Nd}xT evolution diagram. The samples present crustal sources and Paleoproterozoic to Neoarchean model ages. The triangles correspond to Príncipe Granite samples, squares to tectonite samples and rhombi to hydrothermalite samples.

5. THE PRÍNCIPE GOLD DEPOSIT

The Natividade Gold District is characterized by several gold deposits formed along or near to shear zones and hosted in quartz±carbonate veins. The Príncipe Gold Deposit is located at the southeastern district area, where hydrothermally altered granitoids host the auriferous quartz veins. The Príncipe granite played an important role in the deposit formation, contributing for the gold and other base metals entrapment inside a regional-scale pressure shadow.

The Príncipe granite presents two pressure shadows at its northern and southern limits, where the granitoids' hydrothermal alteration was more intense (Corrêa et al., 2014). These hydrothermally altered rocks will be reffered in this work as hydrothermalites. The pressure shadows are evident features at the gamma-ray spectrometric RGB ternary composition image (Figure 3), where the southern pressure shadow is characterized by a high-K signature, while the northern shows a high-eTh response. In magnetometric images (Figure 4), both pressure shadows present medium to high anomalies, probably caused by the influence of the shear zones at their borders. The Príncipe gold deposit is located at the northern pressure shadow, which is the main focus of this paper.

5.1 Hydrothermal Alteration

5.1.1 Mineral Assemblages

In a manner similar to the deformation, hydrothermal reactions have a heterogeneous character, being more intense next to faults, shear zones and veins. These structures concentrated the hydrothermal solution, increasing the fluid-rock interaction and the reactions efficiency along them. Since mineralization is strongly controlled by structures that appear in all scales of observation, it is hard to delimit hydrothermal alteration haloes. Although the deposit does not show a clear zoning, five paragenetic sequences were defined, named as Regional Alteration Halo, Low, Medium and High Intensity stages, and Mineralized Veins (Figure 15).

The Regional Alteration Halo occurs outside the pressure shadow domain in several lithologies across the Natividade gold district. The halo applies a slight alteration in the rocks, preserving their primary texture, but with the presence of metasomatic minerals such as epidote, titanite and magnetite in some samples. Minerals like magnetite, calcite and tourmaline are common along shear zones, as well as kyanite (Corrêa & Sousa, 2012) in some areas along the Cruz das Almas shear zone (Figure 16). This halo is also responsible for the increase of the geochemical background, with enrichments in Fe, Mg and Ca.

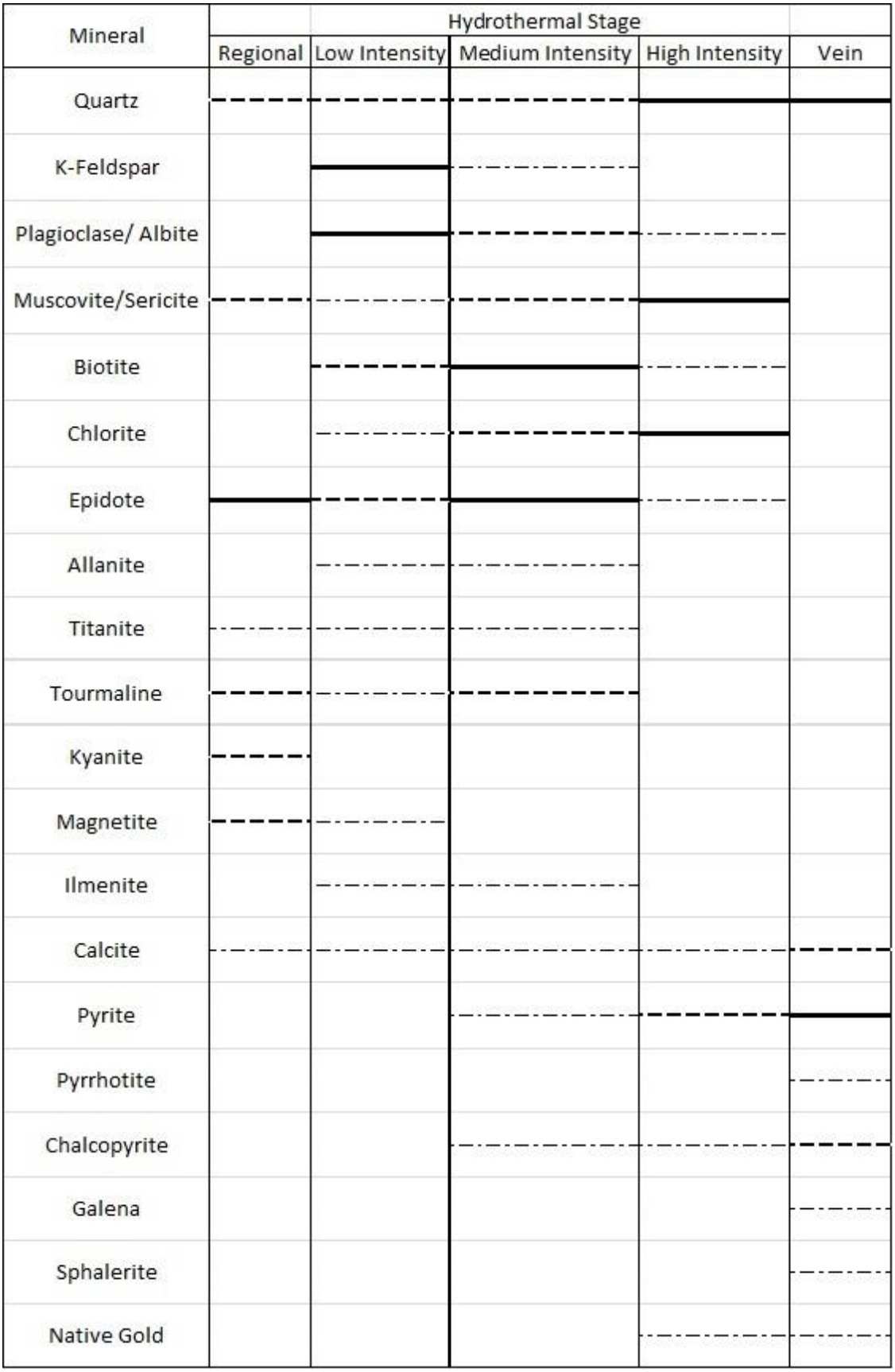

Figure 15: Paragenetic sequences of the Príncipe gold deposit, showing the five alteration stages. Each phase is represented with the abundance of each mineral, where the blank spaces indicate absence of the mineral, the fine dashed lines a small quantity, the thick dashed lines a bigger quantity and the continuous line a large quantity of the minerals.

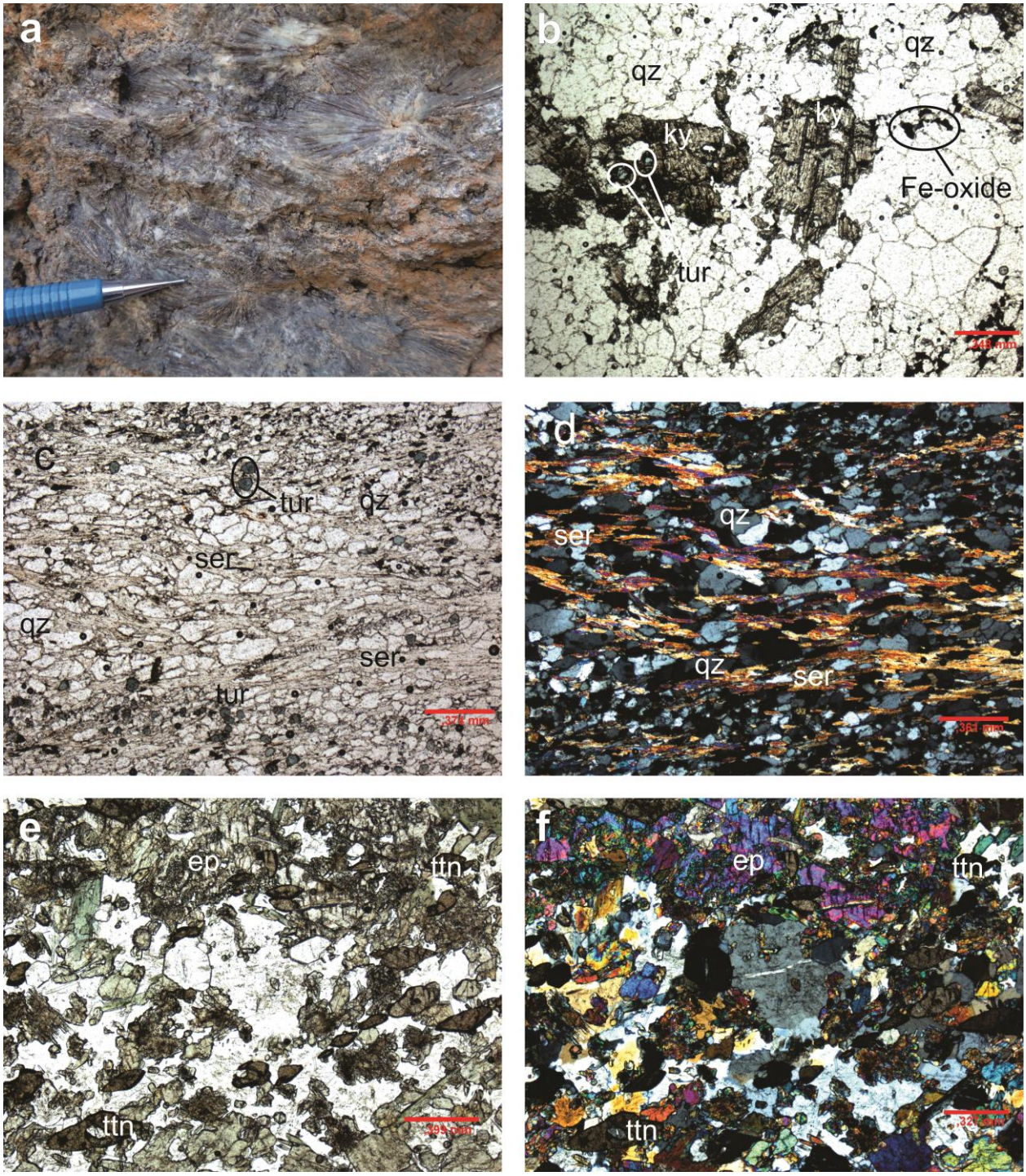

Figure 16: Regional alteration halo rocks. a: Kyanitite outcrop along the Cruz das Almas shear zone. The kyanite crystals present centimetric dimensions and radial habit with origin associated to hydrothermal processes (Oliveira et al., 2012). b: Kyanite-quartz-mylonite showing the association between kyanite, tourmaline and Fe-oxides. c-d: Tourmaline-sericite-quartz-mylonite presenting the co-genetic and syn-kinematic character of these minerals, where the aligned tourmaline crystals, the lepidoblastic texture of the sericite grains, and the stretching of the opaque minerals are parallel to the foliation. e-f: Calc-silicate rock with large amounts of hydrothermal epidote and aligned titanite grains. The mineral abbreviations are displayed according to Whitney & Evans (2010).

The remaining hydrothermal alteration stages are located inside the pressure shadow limits and depend on the reactions' intensity. The main processes identified include the primary minerals hydrolysis, especially feldspars, and the metasomatism by elements from the hydrothermal solution. Independently of the hydrothermalism intensity, the rocks inside this domain are generally green colored due to the presence of neoformed epidote and chlorite (Figure 17).

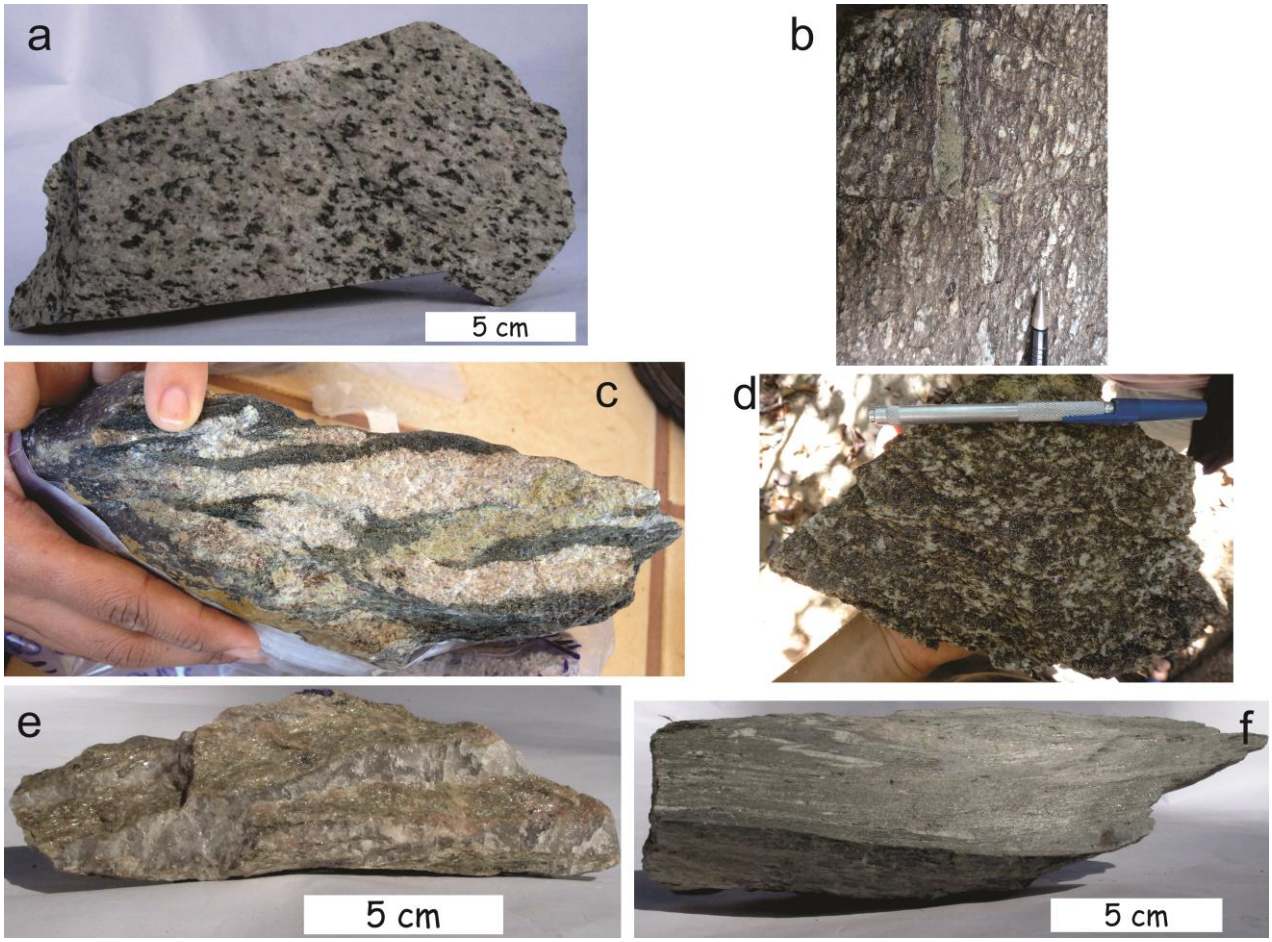

Figure 17: Macroscopic hydrothermalites samples. a-b: Low intensity stage samples. a: The rock shows the beginning of the feldspar alteration and biotite neoformation, concentrated in agglomerates. b: At this stage, the rocks still tend to preserve their igneous texture, but the minerals, however, present signs of alteration, such as porphyroclasts saussuritization and fracturing. c-d: Medium intensity stage samples. c: The rock presents a segregation between quartz-feldspar domains and phyllosilicate-rich bands. The light green area corresponds to an epidote-rich portion. d: This sample represents the intensification of the feldspars hydrolysis, presenting higher biotite and sericite concentrations. At this stage it is no longer possible to discern the feldspar variety. e-f: High intensity stage samples, with both presenting quartz segregations bordered by lepidoblastic sericite and biotite bands.

At the Low Intensity Stage (Figures 17 and 18), the igneous protoliths texture and structure is still preserved. It is characterized by the beginning of quartz-feldspar domains physicochemical destabilization, being substituted by hydrothermal minerals. The quartz presents dynamic recrystallization features, such as segregations, sutured contacts and wavy extinction. The plagioclase starts to be replaced by epidote and presents higher albite contents than the ones from adjacent rocks, while the K-feldspar alters to sericite. The feldspars still preserve their original habit, showing discrete grain rotation and stretching. The neoformed epidote and sericite occur around their borders or as little inclusions inside the crystals.

Hydrothermal phyllosilicates, such as sericite, biotite and chlorite, are common at this stage. These minerals generally appear as fine grained lamellae oriented parallel to the main mylonitic foliation, composing a lepidoblastic texture. Other common microstructures formed by these minerals are pressure shadows, microscopic shear zones and intrafoliation folds. The biotite shows a chlorite substitution, frequently appearing as reaction rims. The most common accessory minerals at this stage are carbonate, titanite, tourmaline and allanite.

The Medium Intensity Stage (Figures 17 and 19) is characterized by the enhancement of the processes described at the low intensity stage, such as silicification, saussuritization, biotitization, chloritization, sericitization and carbonatation. Although the hydrothermal minerals occur well formed, in bigger amounts and sizes, it is still possible to recognize the rock's primary features because there is no complete mineral replacement.

This stage can be identified by several diagnostic characteristics. First, the quartz static recrystallization features, where quartz agglomerates with medium to coarse grained crystals form planar contacts and triple junctions between them and compose the rocks granoblastic texture. Secondly, an increase in the feldspars alteration grade, where a distinction between plagioclase and K-feldspar is not always possible. A third feature is the start of sulfides precipitation, still being discrete at this phase. And last, the monomineralic aggregations, formed in most of the cases by biotite or epidote, occurring as bands or agglomerates.

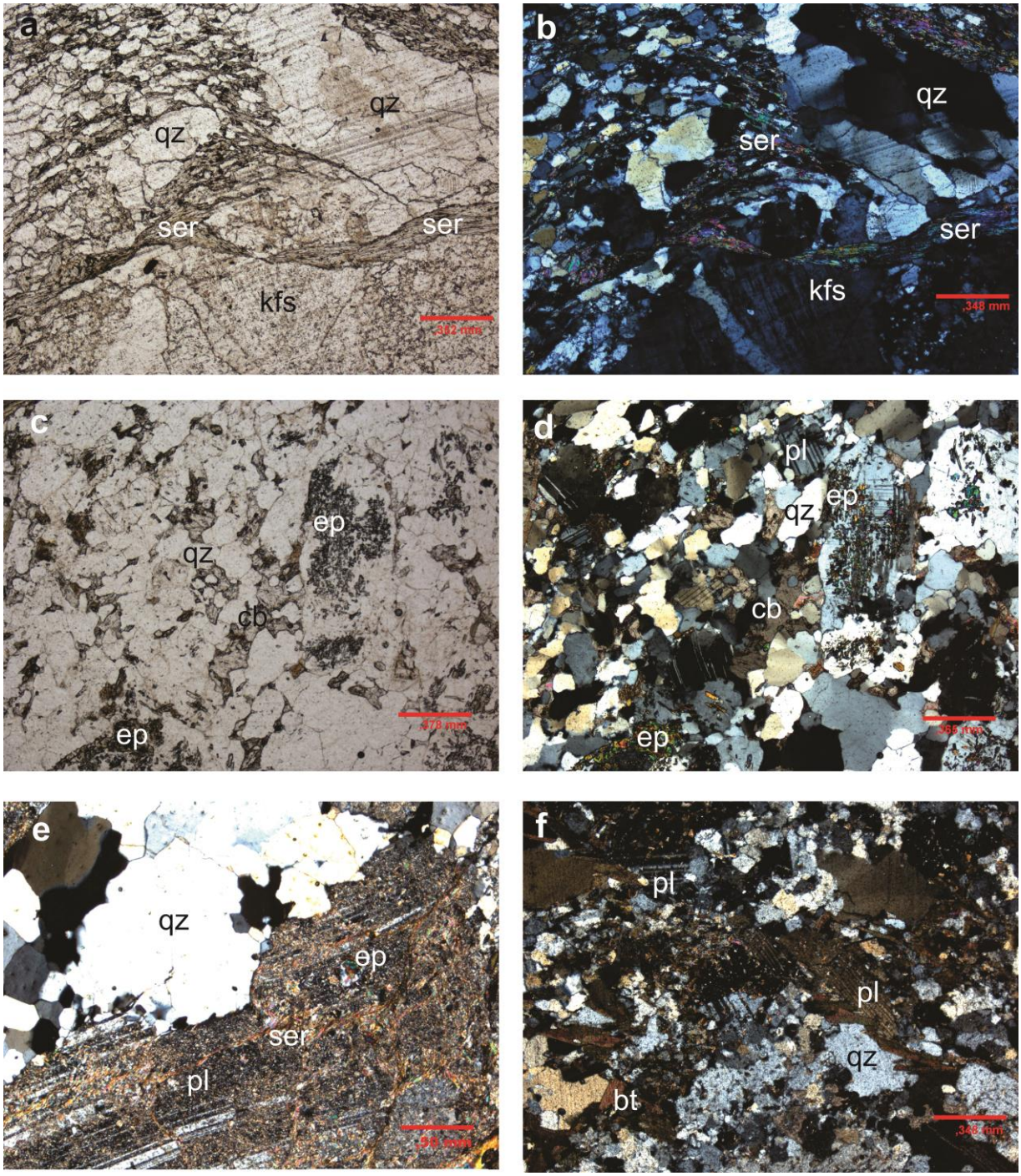

Figure 18: Low intensity stage micrographs. a-b: Rotated quartz segregation with dextral kinematics. Although the K-feldspar relict phenocryst is still preserved, the neoformed sericite already marks the rock's lepidoblastic texture. c-d: The beginning of saussuritization and carbonation processes, where the feldspars can still be identified and distinguished. e: Altered and fractured relict plagioclase porphyroclast being substituted by epidote and sericite. The alteration process is more intense at the crystal's borders than at its interior, and the microfractures are filled by sericite. f: Although part of the minerals is recrystallized or altered, the rocks at this stage still preserve their primary texture. The mineral abbreviations are displayed according to Whitney & Evans (2010).

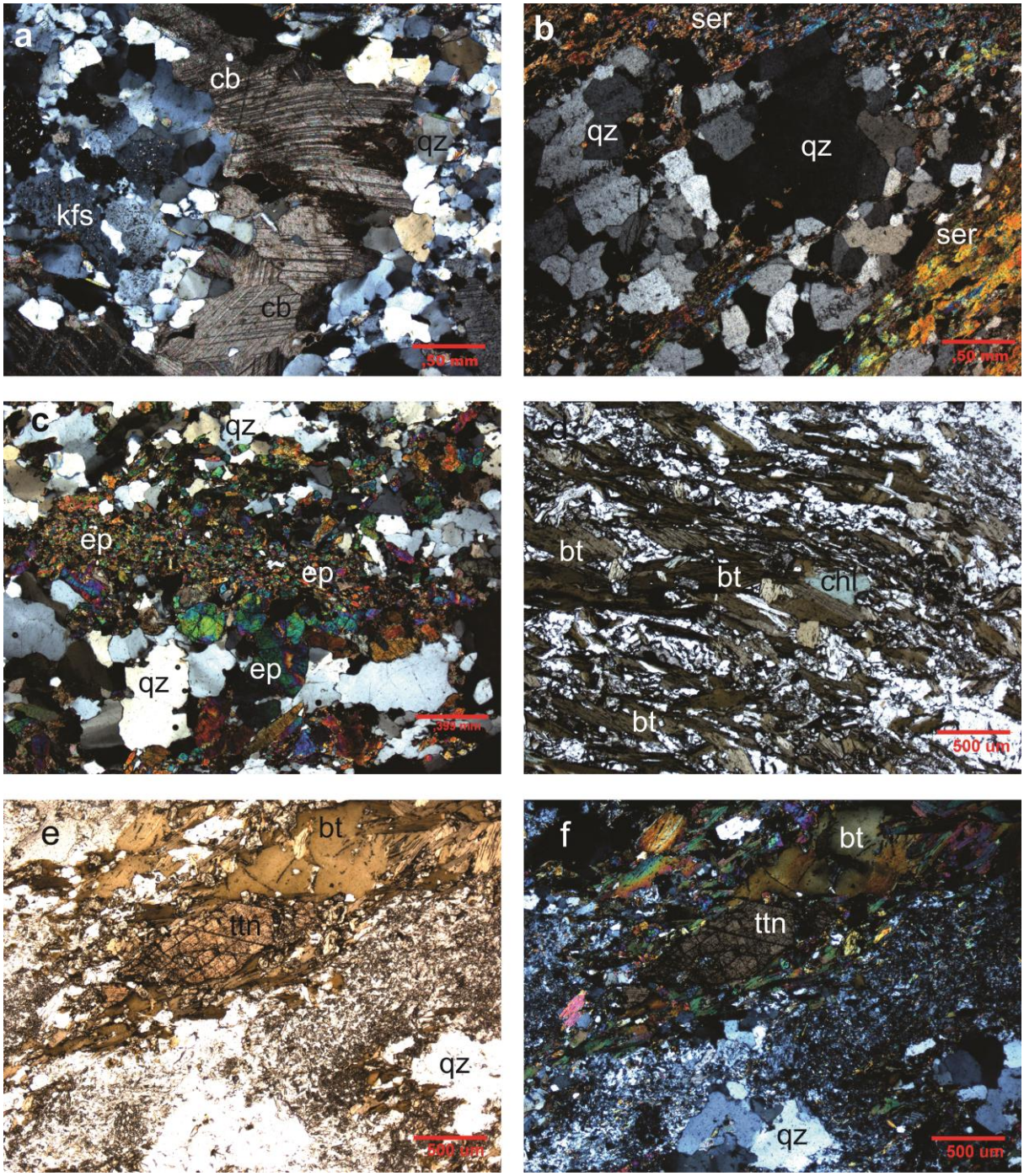

Figure 19: Medium intensity stage micrographs. a: The carbonate vein cutting the granitoid presents the intensification of the carbonation process. b: The picture shows quartz static recrystallization features and intensification of the sericitization process, where quartz agglomerates are bordered by sericite bands. c: Intensification of the epidotization process, where aggregates of well-formed and bigger grains than the low intensity stage are produced. d: Intensification of the biotitization process, with biotites parallel to the mylonitic foliation. The chloritization process is also evident, altering even the neoformed biotites. e-f: Neoformation of coarse hydrothermal titanite grains. Other common porphyroblasts at this stage are allanite and tourmaline. The mineral abbreviations are displayed according to Whitney & Evans (2010).

The High Intensity Stage (Figures 17 and 20) is defined by the extensiveness of the hydrothermal processes already described, including the sulfidation reactions. This stage is characterized by the full feldspars hydrolysis, being completely replaced by phyllosilicates. The main mineralogy is constituted by quartz, sericite, biotite, chlorite, carbonate, and sulfides.

Generally, these rocks are enriched in quartz and have less than 5% carbonate, suggesting that the hydrothermal fluid had low CO_2 contents. The sericite is the typical feldspar alteration product, frequently being the most common mineral. The kind of prevailing phyllosilicate is strongly controlled by the protolith composition, varying with the location. At more mafic protoliths, chlorite is the predominant mineral, as even the neoformed biotite shows signs of chloritization.

Under mesoscopic observations (Figures 21 and 22), the mineralized veins are constituted mainly by milky or crystalline quartz, are often banded, and have a late-deformation aspect. They are generally NS-trending, with subvertical dip angles and subparallel to the main foliation. Only the center of the veins is mineralized, with thicknesses up to 20cm, while the barren external portion may reach thickness values up to 8m. The gold unassociated to sulfides occurs stretched and placed along plans.

Microscopically, the veins are constituted by quartz, carbonate and sulfides. When recrystallized, the minerals tend to be equigranular under a granoblastic texture, with euhedric pyrite agglomerates. When more deformed, the minerals are stretched and form sutured contacts between them. More than 90% of the sulfides are pyrite, with minor proportions of chalcopyrite, pyrrhotite, galena and sphalerite (Figure 23). Three mineralogical assemblages were recognized for the veins; the quartz-carbonate-pyrite, the quartz-carbonate-pyrite-chalcopyrite-pyrrhotite-gold and the quartz-carbonate-pyrite-chalcopyrite-galena-sphalerite-gold parageneses.

Chalcopyrite, pyrrhotite and galena frequently occur associated to pyrite, as inclusions or at their borders. The pyrite sometimes appears stretched parallel to the foliation, following the phyllosilicate's lepidoblastic texture. Native gold, when visible at the microscope, frequently appears as inclusions in sulfides, and more rarely between quartz crystals.

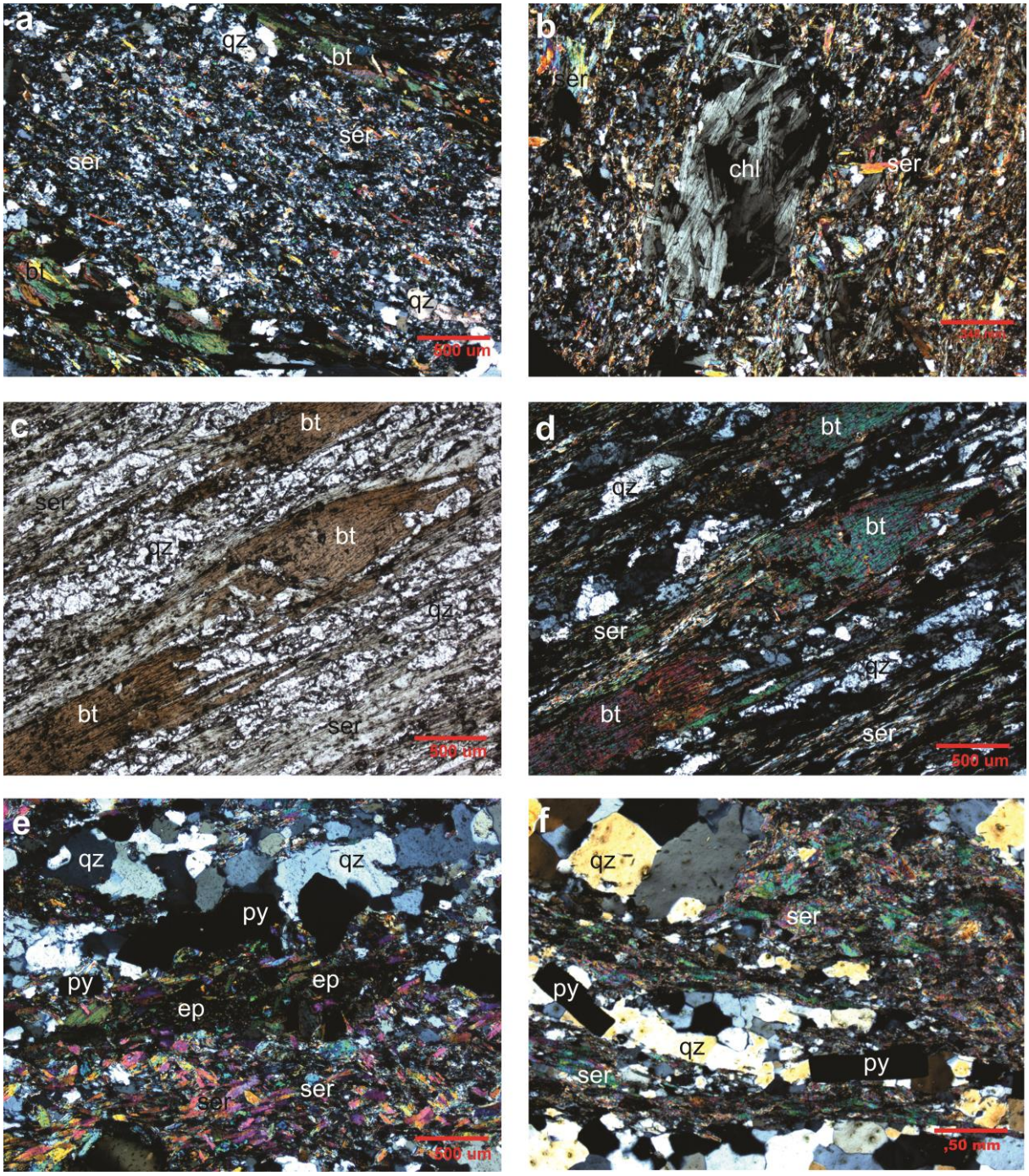

Figure 20: High intensity stage micrographs. a: Feldspars alteration matrix. At the high intensity stage, the feldspars are fully replaced by a fine grained quartz-sericite matrix. b: Hydrothermal chlorite aggregate inside the neoformed matrix and parallel to the foliation. c-d: Sericitization and biotitization processes. The rock is constituted by quartz, lepidoblastic sericite and biotite porphyroblasts. e: Microscopic monomineralic bands with quartz-, pyrite-, epidote- and sericite-rich domains. f: Typical sample of the high intensity stage, composed by quartz, sericite and pyrite. The e-f micrographs show the sulfidation process, where the pyrites occur aligned and stretched parallel to the foliation. The mineral abbreviations are displayed according to Whitney & Evans (2010).

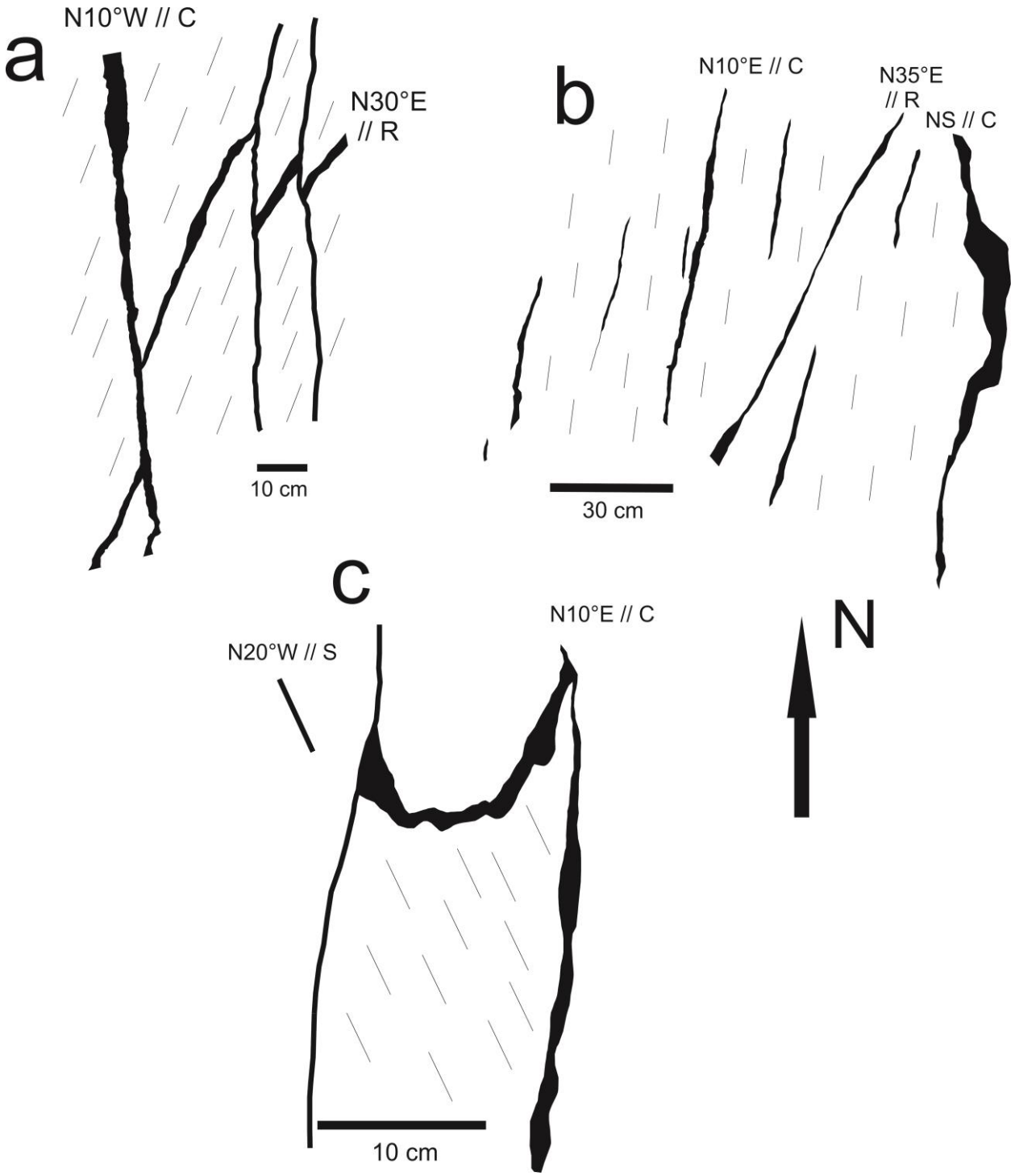

Figure 21: Quartz veins observed in outcrops along the Príncipe gold deposit. The structural trends were correlated to the Riedel system. a: N10°W-trending vein crosscutting a N30°E vein that is parallel to the foliation. b: Irregular and discontinuous N10°E, N35°E and NS veins. The N10°E vein is parallel to the mylonitic foliation. c: Minor-scale pressure shadow, where the N20°W foliation, parallel to the regional S foliation, is truncated by the N10°E veins, parallel to the C foliation.

Figure 22: Macroscopic mineralized quartz veins. a-e: Veins presenting sulfides such as pyrite (a,b,c,d,e) and galena (d), appearing with different textures. Some of the sulfides occur along sericite-biotite-rich bands parallel to the main foliation (a,b), while others appear as medium to coarse euhedral grains at agglomerates (c,d,e). Some samples present discordant monomineralic tourmaline veins (d). f: Native gold unassociated to sulfides inside a quartz vein. It appears deformed and occurs along planes.

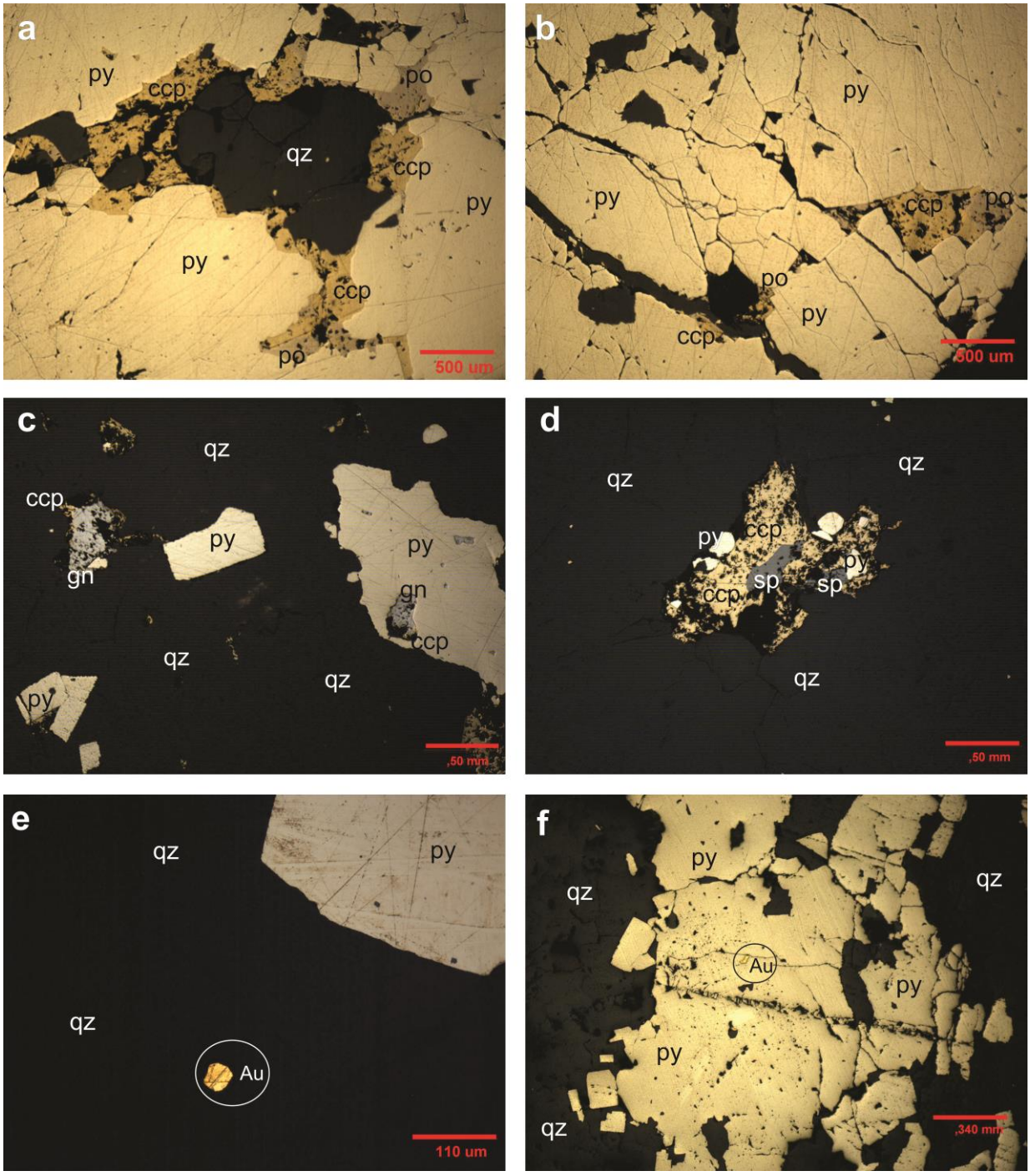

Figure 23: Mineralized quartz veins micrographs. a-b: Pyrite-chalcopyrite-pyrrhotite sulfide association, with the pyrite being the most abundant sulfide. c: Pyrite-chalcopyrite-galena sulfide association. d: Pyrite-chalcopyrite-sphalerite sulfide association. The sphalerite and galena occur at the same samples, but were not seen together with pyrrhotite. e: Native gold inside a quartz crystal. f: Native gold inclusion inside a pyrite. The gold is typically precipitated associated to sulfides. The mineral abbreviations are displayed according to Whitney & Evans (2010).

5.1.2 Mineralized Rocks Geochemistry

The tectonites and hydrothermalites present compositional contrasts with the Príncipe Granite, especially for the more mobile chemical elements (Figure 24). The geochemical analyses indicate alkalis leaching and Fe, Ca and Mg metasomatism processes occurring through hydrothermal reactions. The loss of Na and K occur due to the primary feldspars hydrolysis, producing biotite and sericite, common minerals at these neoformed rocks. The Fe, Ca and Mg metasomatism is indicated by the formation of the hydrothermal paragenesis with minerals that contain these elements, such as epidote, carbonate, titanite, chlorite and biotite.

The most hydrothermalized samples have Au and Ag contents of 25 and 4 ppm, respectively (Figure 25), with Au/Ag ratios between 5 and 10, being a typical value for this class of deposits (Dubé & Gosselin, 2007). The analyses show discrete enrichments for other base metals. The hydrothermalites REEs spidergram (Figure 8) points LREEs enrichment, a discrete Eu anomaly and decrease in HREEs contents. When compared to the Príncipe Granite, there is a decrease on the LREEs and a slight increase in the HREEs concentrations. This pattern is typical of rocks formed in island arcs (Pearce et al., 1984; Wilson, 1989), suggesting that the hydrothermalites' protoliths are possibly the Rio do Moleque tonalitic and granodiotic rocks, with their origin associated with a volcanic arc environment (Oliveira et al., 2012).

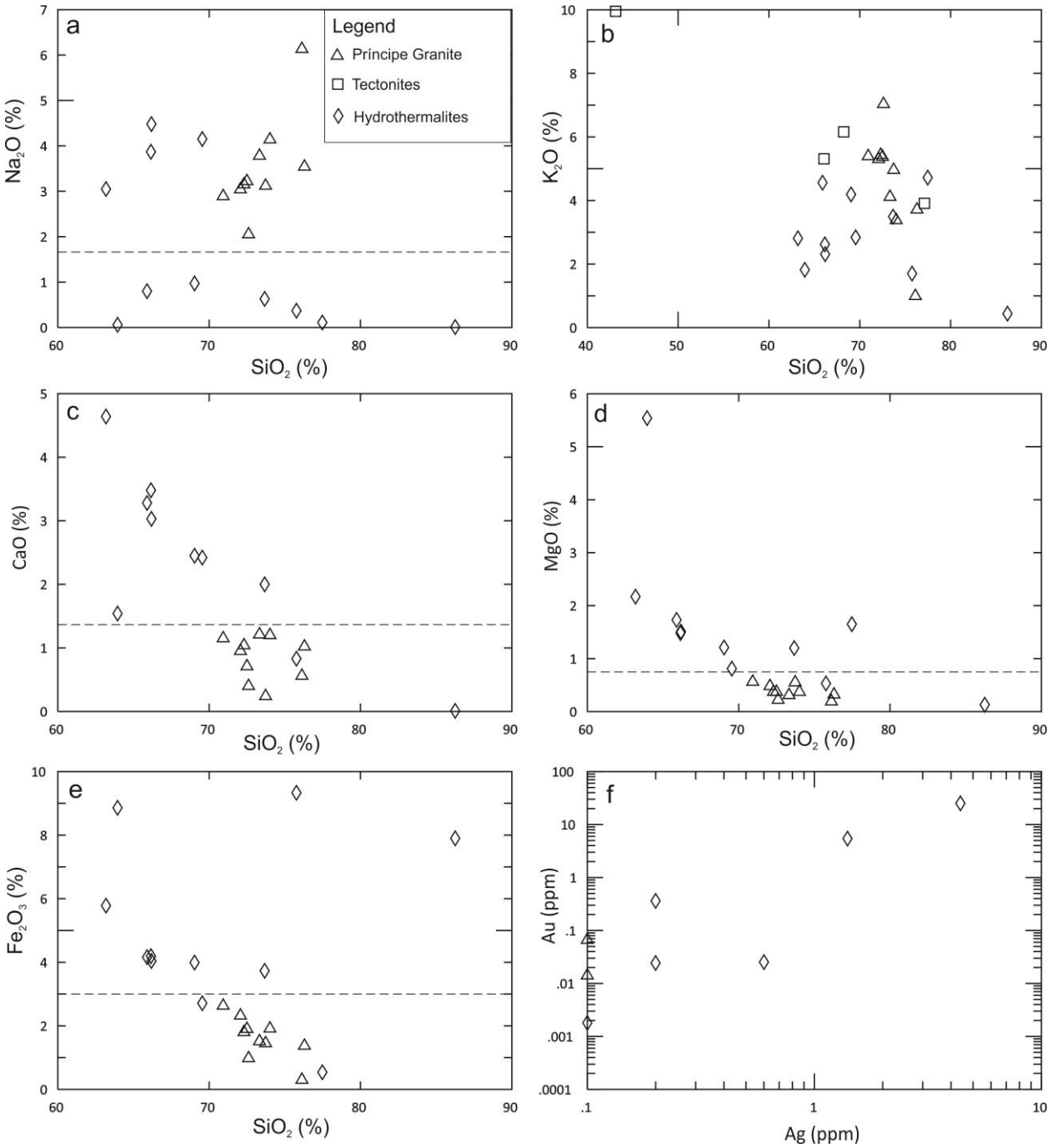

Figure 24: Binary geochemical diagrams that compare compositional and mineralogical discrepancies between the Príncipe Granite (triangles), tectonites (squares) and hydrothermalites (rhombi). The dashed lines mark arbitrary limits between the fields of each kind of rock. a-b: SiO_2xNa_2O and SiO_2xK_2O diagrams, showing the alkali loss at the hydrothermalites and enrichment at the tectonites. c-e: SiO_2xCaO, SiO_2xMgO and SiO_2xFe_2O_3 that show the Ca, Mg and Fe metasomatism at the hydrothermalites, where a whole neoformed mineral assemblage is formed. f: AgxAu diagram, showing the enrichment in these metals at the hydrothermalites, with a Au/Ag ratio between 5 and 10 for the most hydrothermalized samples.

5.1.3 Hydrothermal Minerals Chemistry

Microprobe analyses at the hydrothermalites and tectonites were used to highlight some metasomatic processes. When compared to the Príncipe Granite's plagioclases, the hydrothermalites' plagioclases present even higher Na contents (An_{1-2}). These neoformed plagioclases reveal an albitization process, supported by the loss of Ca and K from the much more calcic Rio do Moleque suite plagioclases.

Petrographic and microprobe analyses in muscovite show chemical differences between the primary and secondary varieties. It is possible to distinguish the unaltered igneous muscovites of the Príncipe Granite from the relict and the neoformed muscovites inside the tectonites (Figure 25). The magmatic muscovites present higher Ti and Fe and lower K contents than the neoformed varieties. The higher Al^{IV} values correspond to the primary muscovites, showing that structural changes occur during the hydrothermal alteration of this mineral.

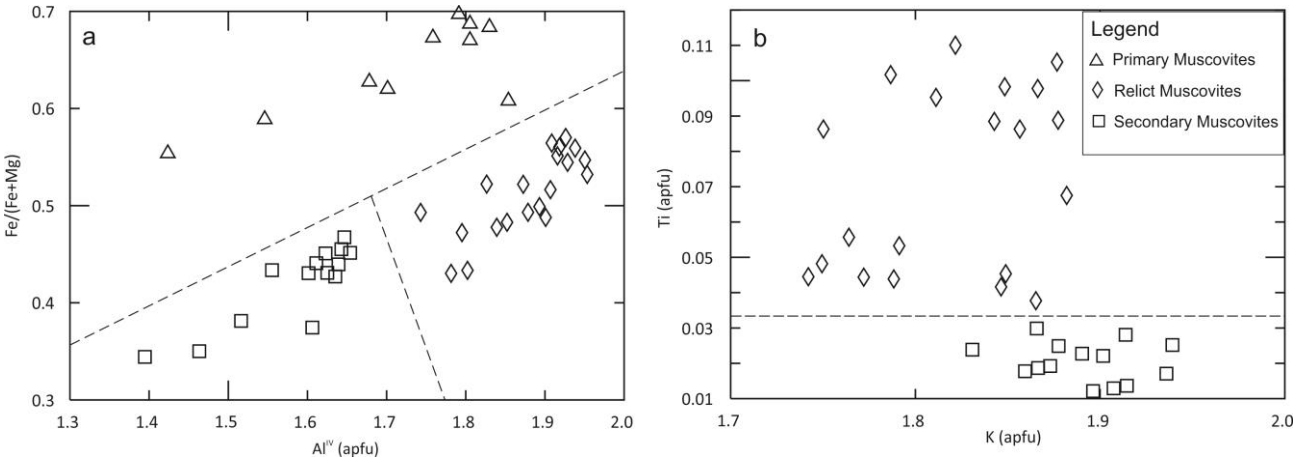

Figure 25: Microprobe diagrams for the analyzed muscovite. The dashed lines mark arbitrary limits between the mineral groups. a: Al^{IV}x(Fe/Fe+Mg) diagram for the Príncipe Granite's primary muscovites (triangles) and the tectonites' relict (rhombi) and secondary (squares) muscovites. The secondary variety can be distinguished for having lower Fe contents than the others. The relict present higher Al^{IV} values than the primary, suggesting a destabilization at their structural formula. b: KxTi diagram for the tectonites' muscovites (rhombi for the relict and squares for the secondary). The diagram shows that the igneous relicts have higher Ti and lower K contents than the secondary muscovites. The mineral formulas were calculated after Tindle & Webb (1990).

The biotite presents a behavior similar to the muscovite, with the primary being richer in Fe and the secondary in Mg (Figure 26). Although the Al^{IV} values do not point structural differences between the magmatic and the neoformed biotites, the higher Mg contents of the hydrothermal variety occur due to the chloritic alteration of this mineral.

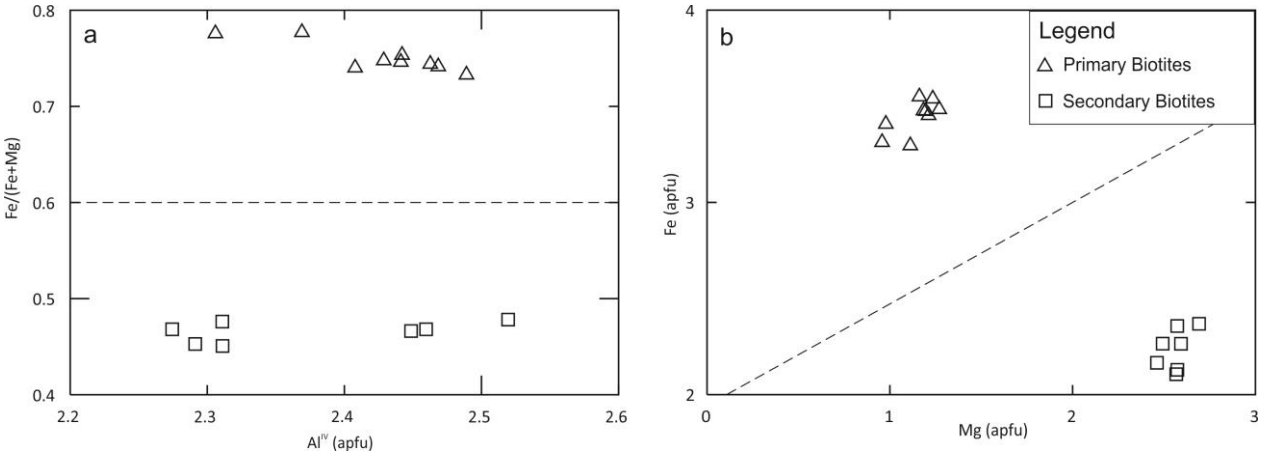

Figure 26: Microprobe diagrams for the analyzed biotite. The dashed lines mark arbitrary limits between each mineral group. a-b: Al^{IV}x(Fe/Fe+Mg) and MgxFe diagrams for magmatic (triangles) and neoformed (squares) biotites. The primary variety is Fe-rich, while the secondary is Mg-rich. The Mg endowment at the neoformed biotites occurs due to the chloritization process of this mineral. The mineral formulas were calculated after Tindle & Webb (1990) and Nachit et al. (2005).

For the chlorite analyses, two hydrothermalite samples from the medium and high intensity stages were used. There are strong compositional discrepancies between these varieties such as their Fe and Mg contents (Figure 27), where the medium intensity chlorites tend to be richer in Fe and the high intensity chlorites richer in Mg. Although there are compositional differences between them, both chlorites plot at the ripidolite field.

Chlorite geothermometer studies were performed following the procedures of Cathelineau (1988) and Caritat et al. (1993) at both groups, presenting values within the 300°C to 400°C range (Figure 28). The distinct Fe and Mg contents of the medium and high intensity chlorites did not affect the temperature data, being undistinguishable at this analysis. This fact suggests that both hydrothermal stages occurred approximately at the same temperature conditions.

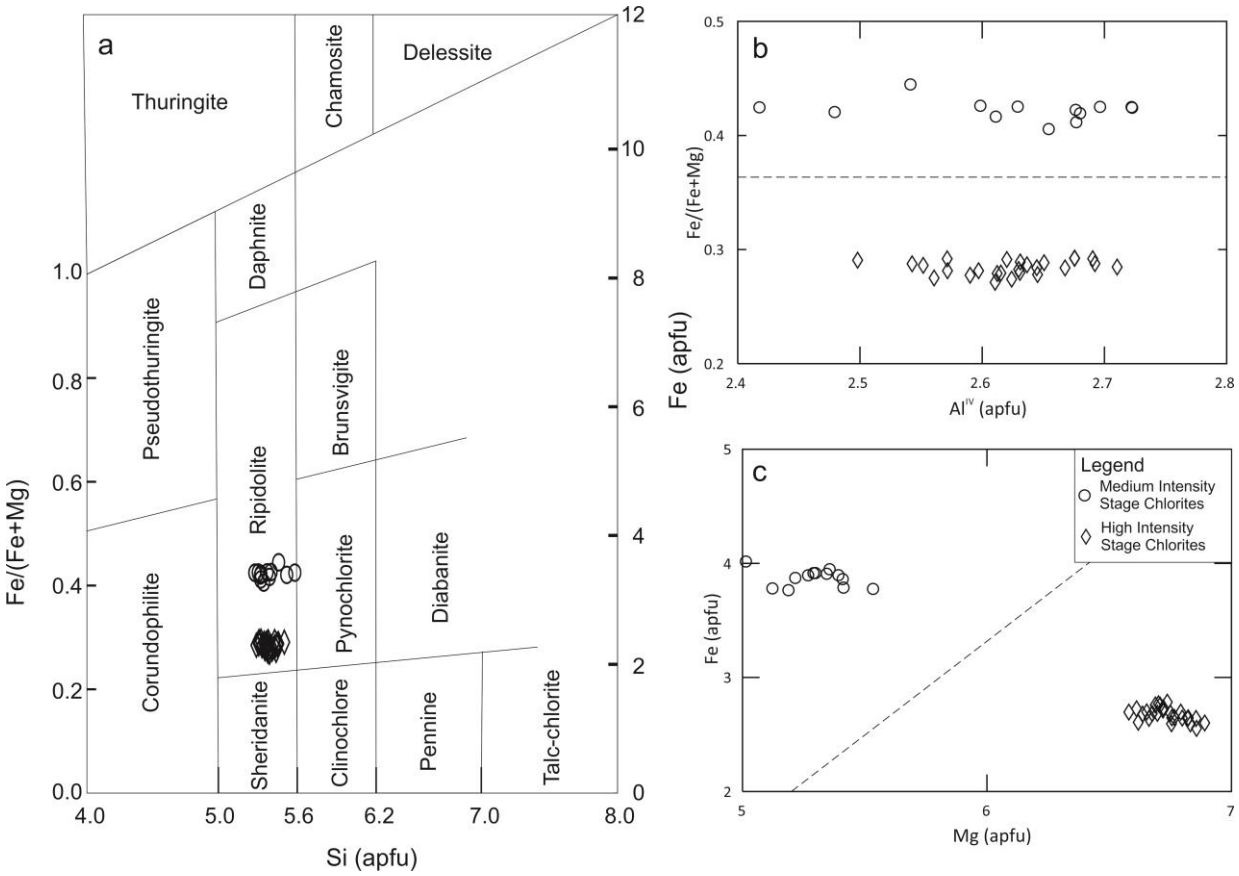

Figure 27: Chlorite (based on 28 O) diagrams for the medium (circles) and high (rhombi) intensity stages. The dashed lines mark arbitrary limits between the distinct mineral groups. a: SixFe/(Fe+Mg)xFe chlorite discrimination diagram (Hey, 1954 apud Saggerson & Turner, 1982). The chlorite data plot at the ripidolite field. b-c: Al^{IV}x(Fe/Fe+Mg) and MgxFe diagrams, showing a similar behavior to the muscovite and biotite, with a cationic exchange of Fe for Mg during the hydrothermalism progression. The mineral formulas were calculated after Nelson & Roy (1958).

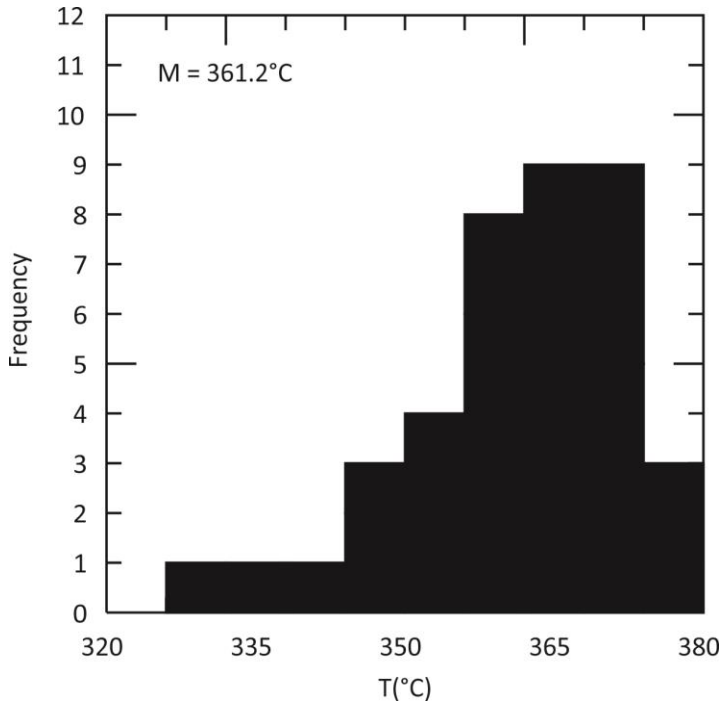

Figure 28: TemperaturexFrequency histogram after the analysis of 39 chlorite grains. The average temperature is 361.2°C. The values were obtained according to the procedures of Cathelineau (1988), Caritat et al. (1993) and Klein et al. (2007).

Carbonate and sulfides were analyzed at mineralized quartz vein samples and their formulas calculated after Deer et al. (2013). The hydrothermal carbonate composition is essentially calcitic, with minor contributions of Fe, Mg and Mn. Like the carbonate, the sulfides are also very pure, often presenting Au and Ag inclusions. The pyrite often displays anomalous Au contents up to 110 ppm. The chalcopyrite shows Ag and Au contents up to 2700 ppm and 50 ppm, respectively. The pyrrhotite presents up to 70 ppm Au and 1000 ppm Co. The galena has Ag and Bi concentrations up to 2700 ppm and 1500 ppm, respectively. Other discrete metal contributions in sulfides include Cd, As, Se, Zn, Sb, Pt and Pd.

5.1.4 Carbon, Oxygen and Sulfur Isotopes

The main purpose of the analyses by stable isotopes at the Príncipe Gold Deposit was to determine the fluid source by comparing the data with other geological materials (Thode, 1991; Hoefs, 2009; Pirajno, 2009) and orogenic gold deposits from Brazil (Klein et al., 2005; Klein et al., 2007) and around the world (Bierlein et al., 2004; Sarangi et al., 2012).

For the S isotopes analyses (Table 9), five quartz-sericite-pyrite vein samples were selected, four of them belonging to the Príncipe deposit and one to the Chapada de Natividade deposit. The $\delta^{34}S$ data show low value discrepancies for a same sample, but higher variations between samples. The restricted interval from -1‰ to 3‰ shows a low S isotopic fractionation. The low abundance of sulfide minerals other than pyrite made it difficult to form mineral pairs for thermometric studies.

For the C and O isotopes analyses (Table 10), two carbonate veins from the Príncipe deposit were selected. Both samples have calcitic composition, with one vein subparallel to the main mylonitic foliation and the other perpendicular to it. While the $\delta^{13}C_{VPDB}$ values are homogeneous, around -6‰, the $\delta^{18}O_{VPDB}$ and $\delta^{18}O_{VSMOW}$ values show a higher variance, between -13‰ and -17‰ for the $\delta^{18}O_{VPDB}$, and from 13‰ to 18‰ for the $\delta^{18}O_{VSMOW}$. Some difficulties were faced during the analyses due to the low quantity of carbonate veins, making it hard to perform larger scale studies.

At orogenic gold deposits, the $\delta^{34}S$ tend to be slightly positive, commonly between 0‰ and 10‰ (Kerrich, 1987), as well as the $\delta^{18}O_{VSMOW}$ values, between 6‰ and 13‰ (Mccuaig & Kerrich, 1998), while the $\delta^{18}O_{VPDB}$ show negative values within the 0‰ to -10‰ range (Goldfarb et al., 2005). These intervals suggested by the literature are typical of magmatic or metamorphic fluids and fit the Príncipe gold deposit isotopic data, always pointing to low fractionation rates.

5.1.5 Hydrothermal Solution Studies

To determine the physicochemical conditions during the entrapment of the mineralizing fluid, four samples of mineralized quartz veins were analyzed. Three of these samples belong to the Príncipe deposit and one to the Chapada de Natividade deposit, sharing similar petrographic and microthermometric characteristics. The fluid inclusions were identified and classified in families according to their shape, system type, color, number of phases and phase proportion. All analyzed inclusions occur inside the quartz crystals without being aligned along fractures and are correlated to the mineralization process. Some of the inclusions present irregular borders such as sutures, while others have polygonized walls, like negative crystals. Five families were described, three monophasic (aqueous, carbonic and solid), one aqueous biphasic and one aqueous-carbonic triphasic (Figure 29). Temporal relationships between the inclusion groups were not observed.

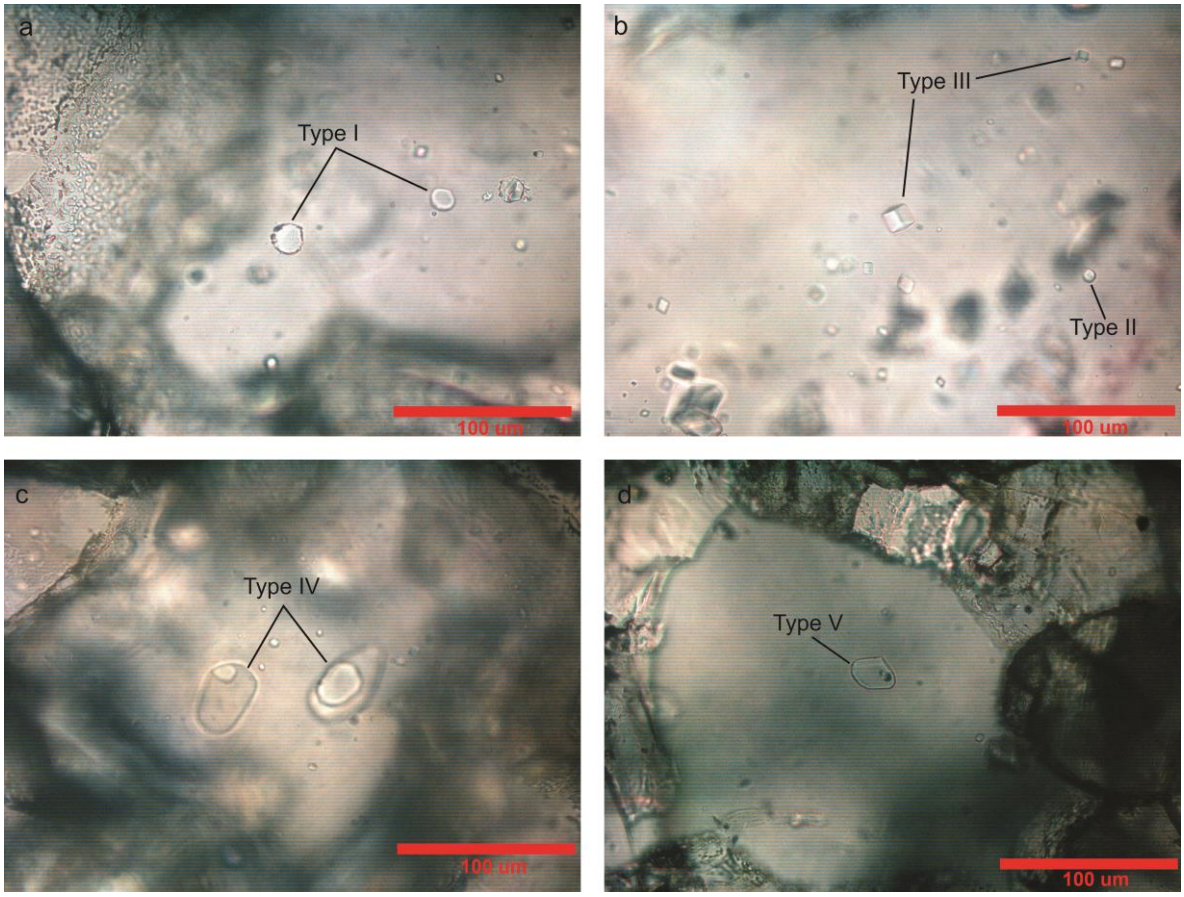

Figure 29: Fluid inclusions micrographs. a: Circular and ellipsoidal Type I inclusions. b: Circular Type II and cubic Type III inclusions. c: Ellipsoidal Type IV inclusions. d: Ellipsoidal Type V inclusion. Only few quartz grains are translucent as the one at the center.

The aqueous monophasic inclusions (Type I) belong to the H_2O-NaCl system and are the most common family, representing more than 90% of the observed inclusions. They are the biggest sized variety, with some inclusions reaching 50 µm, and present circular, elliptical

and rectangular shaped inclusions. The carbonic monophasic (Type II) family belongs to the CO_2 system. The inclusions are rare and tiny, smaller than 10 µm, circular and elliptical, darker than the Type I group. The solid monophasic family (Type III) occurs as scarce cubes or prisms smaller than 10 µm, possibly corresponding to halite crystals that precipitated from the hydrothermal fluid.

The aqueous biphasic inclusions (Type IV) belong to the H_2O-NaCl system, are the second most abundant group and were the only family studied at the microthermometric analyses. They appear as circular and elliptical inclusions, their size ranging from 5 µm to 20 µm. The liquid phase occupies 90-70% of the inclusion volume, while the vapor phase corresponds to 10-30%. The aqueous-carbonic triphasic family (Type V) belongs to the H_2O-CO_2-NaCl system and occurs as rare inclusions with dimensions smaller than 10 µm. They present circular, elliptical and rectangular shaped inclusions where the carbonic phase occupies 20-40% of the volume, with 80-90% volume belonging to the liquid phase and 20-10% to the vapor phase.

During the microthermometric phase, 50 Type IV inclusions were analyzed through cooling and heating processes. At the cooling stage, the ice melting temperatures (Tmice) were registered, occurring within the -8.4°C and -0.7°C interval, with an average of -3.1°C. The eutectic temperature and hydrohalite formation were not observed in these inclusions. During the heating stage, the total homogenization temperatures (Th) were registered, with the homogenization always occurring at the liquid phase, within the 212.7°C to 297.5°C interval, with an average of 249.1°C (Figure 30).

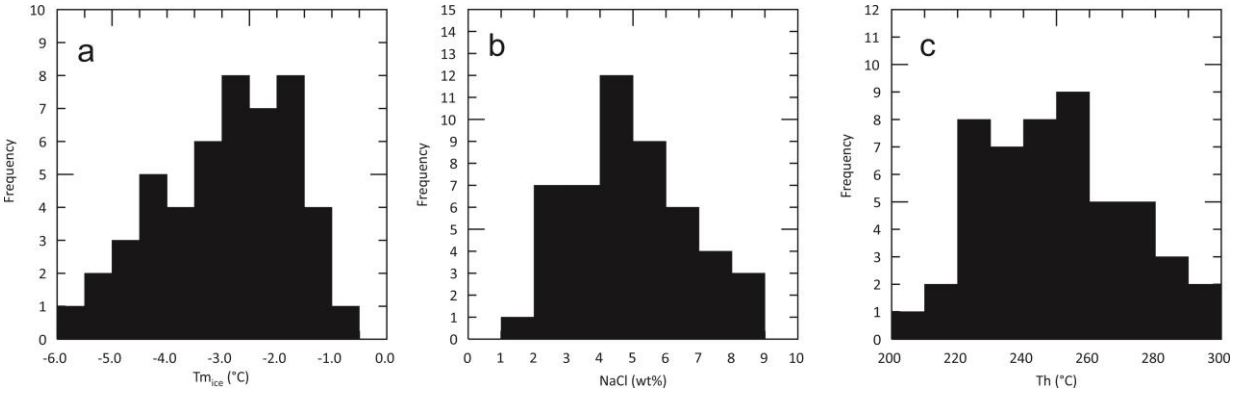

Figure 30: Ice melting temperature (a), salinity (b) and total homogenization temperature (c) frequency histograms using the data of 49 fluid inclusions. For visual purposes, one measurement was excluded from the histograms.

After the microthermometric stage, the fluid salinity and density, and the entrapment pressure were calculated. The salinity values ranged from 1.2% to 12.2%, with an average of 5% NaCl equivalent weight. The solution density occur in the 0.76g/cm³ to 0.93g/cm³ interval, with an average of 0.84g/cm³. The pressure values for each inclusion range from 14.7

bar to 78.6 bar, with an average of 37.3 bar. The isochore was calculated by applying the measured average values at a theoretical pure H_2O-NaCl system (Knight & Bodnar, 1989), with a temperature interval from 250°C to 400°C (Figure 31).

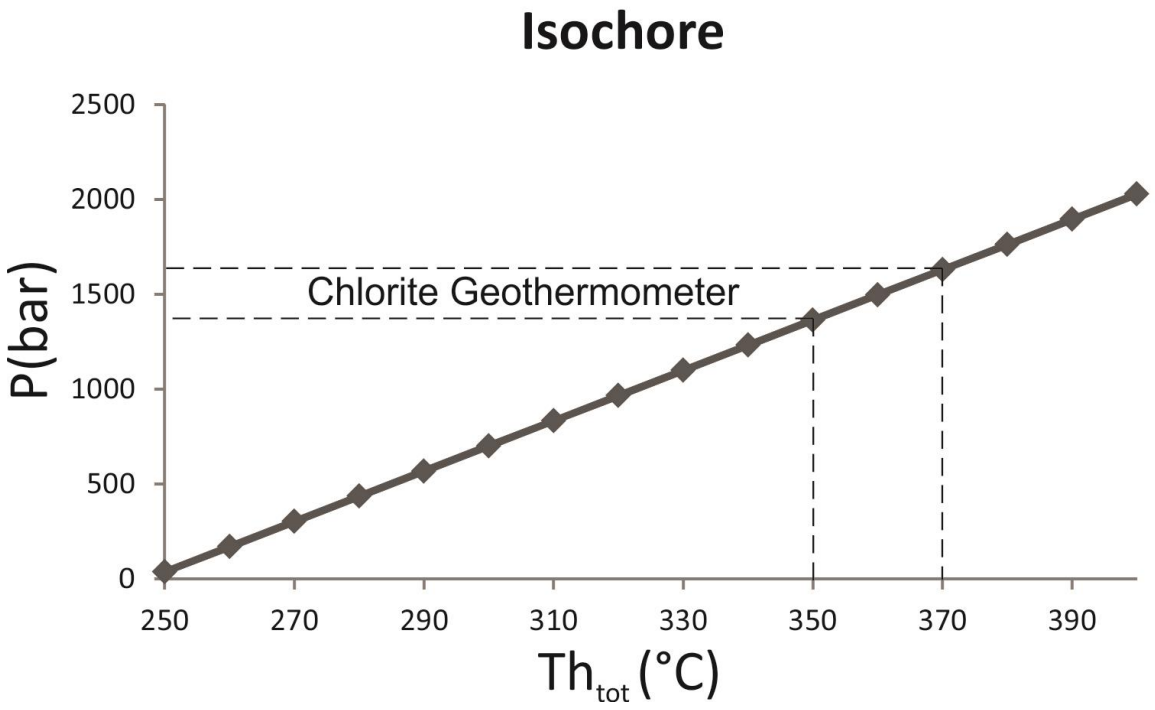

Figure 31: System isochore (Bakker, 2003) based on theoretical models for a pure H_2O-NaCl fluid (Knight & Bodnar, 1989) with 5.1 NaCl wt%, density of 0.848 g/cm³ and initial total homogenization temperature of 249.1°C. The data from the chlorite geothermometer analyses are also plotted and indicate average pressure values around 1.5 kbar.

The variety of inclusion types can be explained by the fluid immiscibility hypothesis (Diamond, 1996; Diamond, 2001), where an initially homogeneous fluid produces other phases after its physicochemical destabilization. A low-NaCl aqueous-carbonic fluid (Type V), typical for this kind of deposits (Diamond, 1990), would precipitate salts (Type III) and exsolute a carbonic (Type II) and an aqueous phase (types I and IV), when submitted to physicochemical changes.

5.2 Pressure Shadow-Controlled Gold Mineralization Model

The Príncipe gold deposit (Figure 32) was strongly affected by the metamorphic, deformational and hydrothermal events implemented under the Brasiliano Cycle's (Schobbenhaus et al., 2004) strike-slip regime. The anomaly shown by the Matched Filtering analyses (Figure 10) at the depth of 11340 m corresponds to the regional Transbrasiliano Lineament direction (Strieder & Suita, 1999; Peri et al., 2013; Santos et al., 2013), responsible for the formation of several deposits along its influence zone, including the Príncipe gold deposit. It presents similar metallogenetic implications to other areas of the world such as the Central Asian (Pirajno, 2010) and Variscan (de Boorder, 2012) orogenic belts, with the mineralization associated to translithospheric strike-slip structures.

The shear zones and the high deformation bands present sigmoid morphology and dextral kinematics, representing a regional scale S-C fabric (Figure 2). These structures form a linked system that acted as a pathway for the channelized hydrothermal fluid migration. The metamorphic tectonites represent the materialization of minor scale shear zones, where the intense fluid percolation caused the complete substitution of the primary mineral assemblage for the neoformed biotite-sericite-quartz paragenesis (Figure 7). The shear zones were formed under a brittle-ductile regime, characterized by quartz recrystallization and feldspars fracturing.

The Euler Deconvolution data (Figure 33) show that the EW-trending anomalies are the shallowest structures, while the NS-N30°E the deepest ones. This fact is supported by field work observations, where the NS-N30°E faults are dextral, have a brittle-ductile nature and are correlated to the mineralization process, while the EW faults have a brittle nature and present sinistral kinematics, being late- to post-mineralization. The distinct depths pointed by the Matched Filtering (Figure 10) and Euler Deconvolution (Figure 33) techniques occur due to the fact that the Euler Deconvolution identifies the top of the magnetometric sources while the Matched Filtering shows the magnetometric values at selected depths.

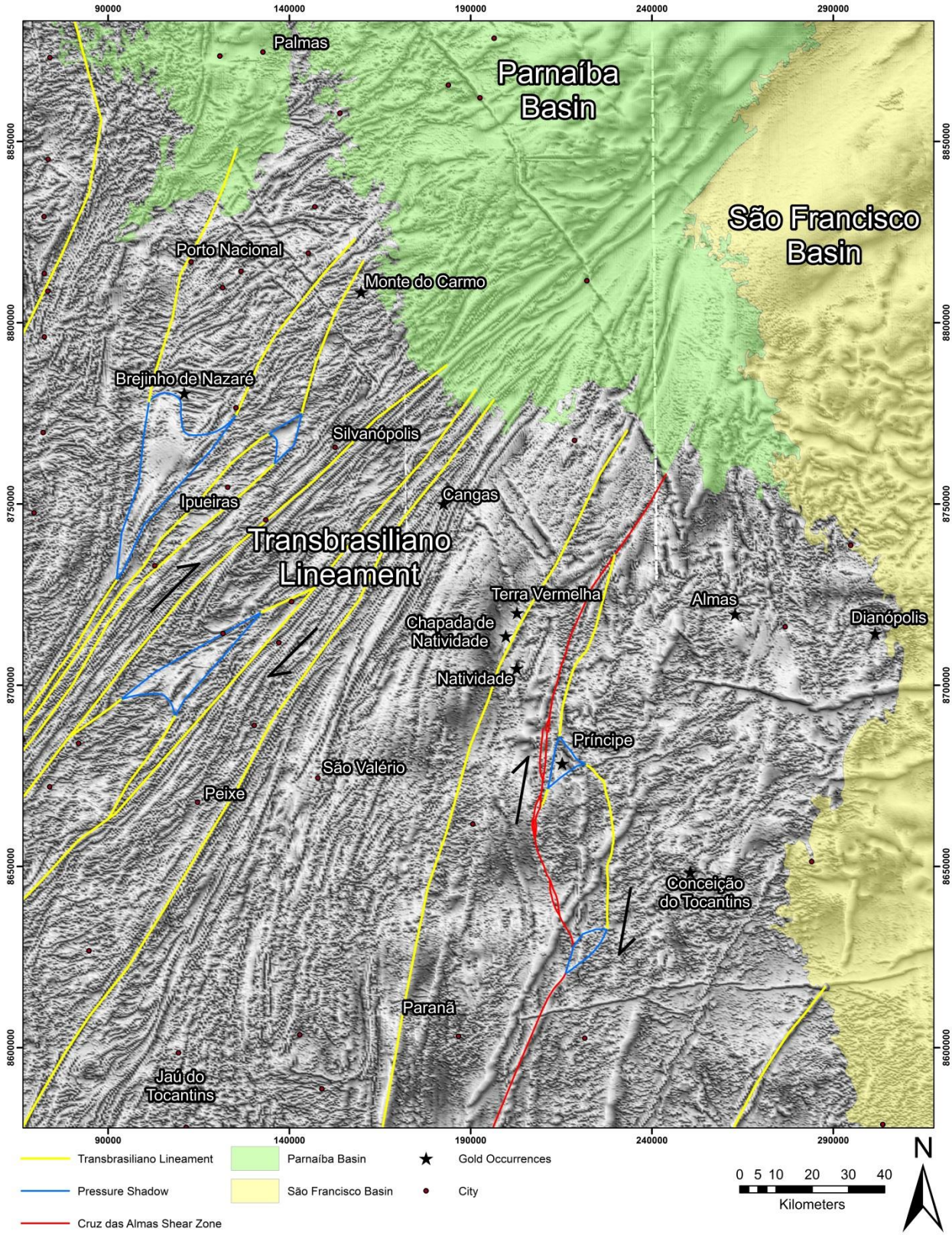

Figure 32: Regional Tilt Derivative image showing the Transbrasiliano Lineament. The Brasiliano cycle was responsible not only for the formation, but also for the reactivation and/or rotation of previous structures, where the hydrothermal fluids percolation was more intense. Several gold deposits and occurrences that originated during the Brasiliano cycle are distributed along this regional structure, including the Príncipe gold deposit, located at the southern part of the figure. Some potential pressure shadows are highlighted in the map, characterized by low magnetic anomalies. Some cities and well-known gold occurrences are also shown on the map.

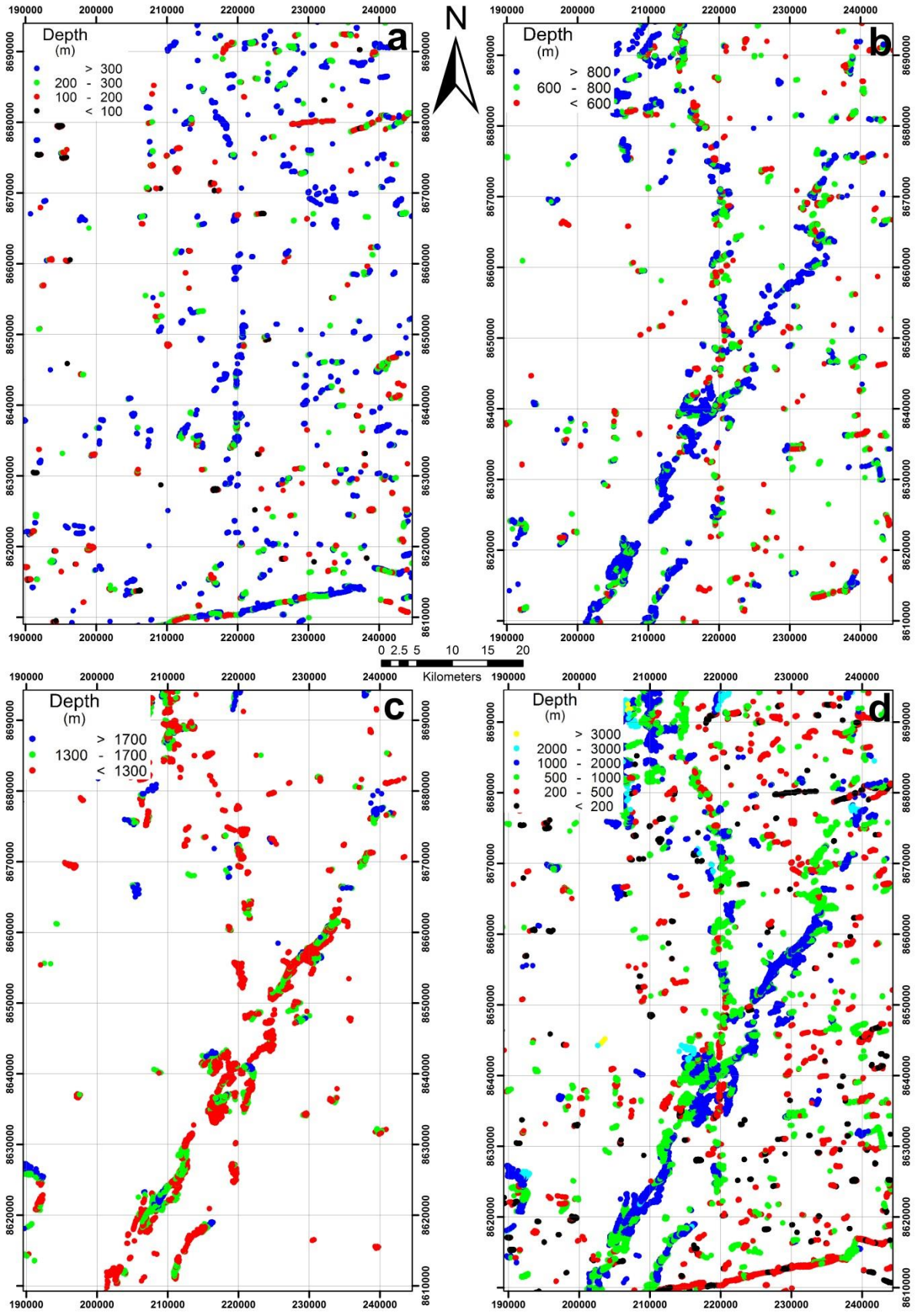

Figure 33: Euler Deconvolution analyses applied to four depth intervals. Several structural families can be identified in each of the products, such as the shallower EW-trending and the deeper N10°W-N20°E and N30°E structures. a: 0-500m interval. b: 500-1000m interval. c: 1000-2000m interval. d: Total data.

These four fault families are correlated to the Riedel shear structures system (Tchalenko, 1970; Davis et al., 2000; Katza et al., 2004; Zerfass & Chemale, 2011). The N10°W-N20°E family correspond to the C foliation, the N50°W-N30°W to P fractures, the N30°E-N50°E to R fractures and the N70°E-EW to R' fractures. Other structures identified in the field are N60°W T-type (tension gashes), being rarer and more restrict than the other fractures. This structure system suggests a brittle-ductile regime for the deformation. Synchronous to the shear zones, these structures also contributed for the fluid migration, leading to the gold mineralization.

Both pressure shadows were formed after the Príncipe Granite's resistance to the deformational and hydrothermal processes that affected the area. In microscopic dimensions, these structures are typically formed at the borders of porphyroclasts (Etchecopar & Malavieille, 1987; Trouw et al., 2010), and the Príncipe Granite played a similar role in a much broader scale. Both pressure shadows are bordered by shear zones, with their centers acting as stress relief zones. Inside the northern pressure shadow, where the Príncipe gold deposit is located, the ore occurs along quartz veins that form an interconnected network due to the pervasive hydrothermal solution migration (Figure 34). These veins are discontinuous, amalgamated, with thickness ranging from millimeters to meters and extension from meters to hundreds of meters (Figure 21).

According to the stable isotopes data, the hydrothermal solution was possibly formed after the metamorphic devolatilization of several source rocks, carrying Au and other metals through reduced S complexes (Stefánsson & Seward, 2004; Phillips & Powell, 2010). This gold bearing low salinity low CO_2 aqueous-carbonic fluid was transported through the interconnected system of faults, fractures and shear zones of different orders and scales (Figure 34), promoting a channelized flow with low fluid-wall rock interaction (Sibson & Scott, 1998; Goldfarb et al., 2005). At higher order structures, such as the Cruz das Almas shear zone, processes like transport and leaching of chemical elements prevailed, while at lower order structures the main processes were formation of quartz veins and metal precipitation along them (Goldfarb et al., 2001; Groves & Bierlein, 2007). The heterogeneous nature of the deformation under a brittle-ductile regime led to the deposit rocks mylonitization in different grades.

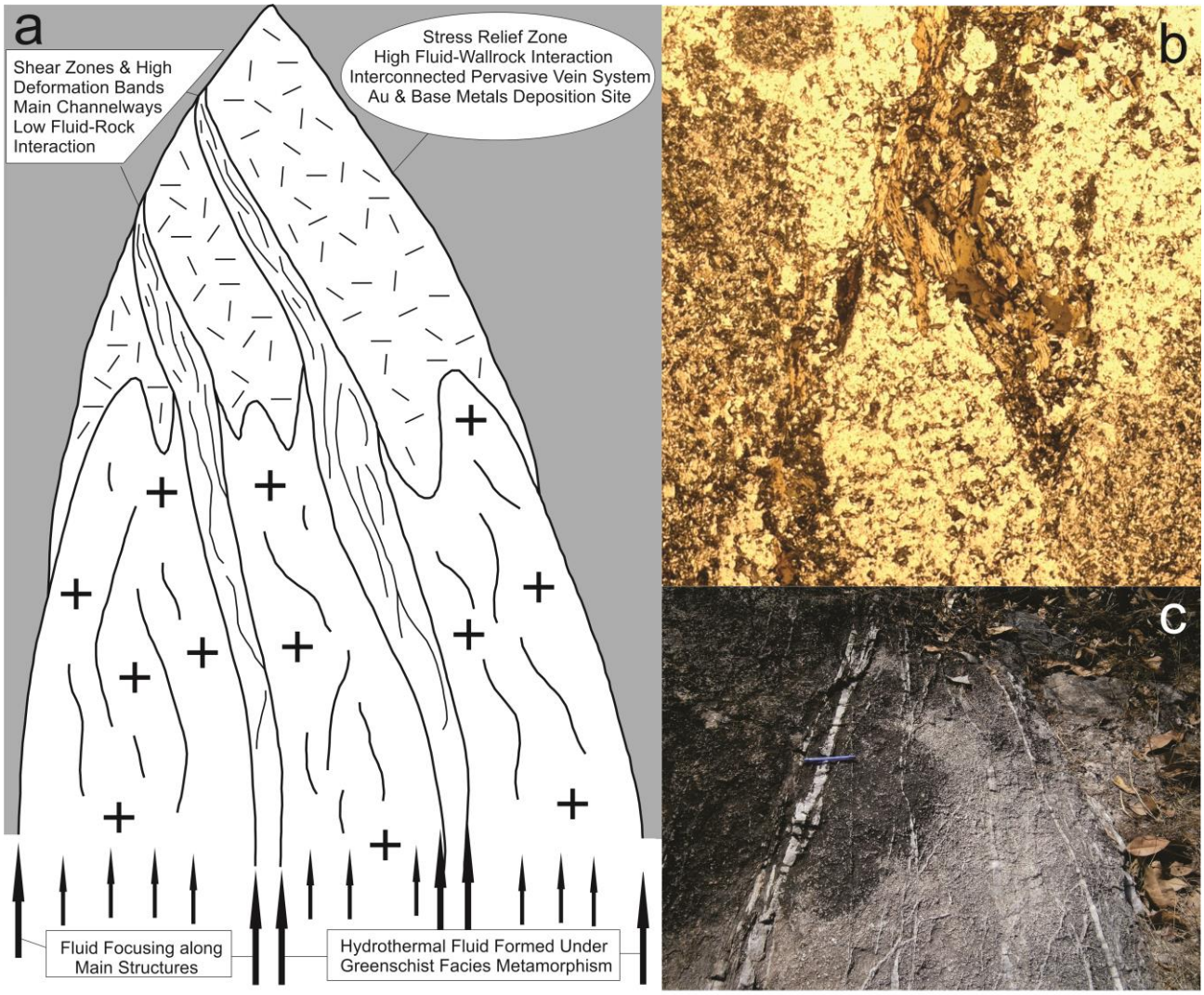

Figure 34: The Príncipe Gold Deposit Mineralization Model. a: Schematic figure showing the fluid migration system, which is more intense at the high deformation bands and at the granite's borders. The pressure shadow domain is characterized by the zone constituted by the Rio do Moleque suite's (gray) hydrothermally altered (lines) rocks. b: Fractal pattern of the Príncipe Gold Deposit represented at a microscopic scale, with the quartz segregation corresponding to the Príncipe Granite, the biotite-rich pressure shadow to the hydrothermalites area and the altered quartz-feldspar matrix to the hydrothermally altered rocks at the Príncipe Granite's borders. c: Quartz vein system presenting the pervasive hydrothermal fluid migration inside the regional-scale pressure shadow.

The metasomatic rocks and minerals present petrographic and geochemical discrepancies with the primary lithologies. The K, Na, Fe, Ca and Mg metasomatism pointed by the analyses confirms the petrographic evidence for alteration and substitution processes, such as hydrolysis, sericitization, saussuritization, silicification, biotitization, chloritization, carbonatation and sulfidation.

Thermometric data of the mineralization by fluid inclusions and chlorite geothermometry define the temperature interval between 220°C and 370°C, values that are typical for this class of deposits (Witt & Vanderhor, 1998; Groves et al., 1998). The calculated pressure values after the fluid inclusions data, however, are below the typical values for this kind of deposits (Dubé & Gosselin, 2007). This fact may be associated to the pressure shadow, acting as a stress relaxation zone and presenting low barometric values. A second hypothesis is based on the fact that the total homogenization temperature of the inclusions represents the minimum entrapment temperature (Shepherd et al., 1985). The formulated isochore for the system shows that at slightly higher temperatures (e.g. 320°C), such as the ones obtained for the chlorite geothermometer, the pressure values fit the expected barometric conditions for orogenic deposits, above 1kbar (Mccuaig & Kerrich, 1998).

The gold precipitation occurred after the hydrothermal fluid physicochemical destabilization. The gold unassociated to sulfides was possibly precipitated by the pressure lowering inside the pressure shadow domain. The gold inclusions in sulfides possibly got deposited after the reaction with the Rio do Moleque tonalitic-granodioritic suite rocks. The gold and reduced S complexes of the hydrothermal solution reacted with the Fe-bearing minerals of this lithology, precipitating the ore. The pervasive fluid percolation inside the pressure shadow zone caused rock alteration at different intensities, culminating in the mineralized quartz veins.

This model can be applied to locations along the Transbrasiliano Lineament zone of influence, where several structures were formed, reactivated and rotated (Figure 32). They are potential exploration targets, since many of them acted as channels for hydrothermal fluids transportation and ore precipitation.

6. CONCLUSIONS

When compared to previous works, the mineralogical, textural, deformational, geochemical, and geochronological characteristics presented in this paper suggest that the Príncipe Granite is an intrusion that belongs, can be correlated or is syn-genetic to the Aurumina suite (Botelho & Silva, 2005). This hypothesis highlights the magnitude and importance of this Transamazonic peraluminous granitogenesis (Botelho et al., 2002), occurring for over 200 km at the states of Goiás and Tocantins.

The Príncipe deposit, as well as several deposits of the Natividade Gold District (Corrêa et al., 2013) and the Almas-Dianópolis terrane (Alvarez, 2006), present features common among the orogenic gold deposits (Groves et al., 1998). One of the most relevant of these characteristics is that the mineralization happened during the Brasiliano Cycle (Brito Neves & Fuck, 2013; Brito Neves & Fuck, 2014), the orogenetic event that metamorphosed the area under greenschist conditions and developed the transcurrent shear zones of the region. Another typical aspect is the epigenetic character of the deposit, due to the hydrothermal processes altering the Paleoproterozoic magmatic protoliths, generating a neoformed paragenesis after a K, Na, Ca, Fe and base metals metasomatism. A third factor is the strong structural control, where the metal deposition was concentrated inside a regional-scale pressure shadow, producing a pervasive vein system constituted by quartz, carbonate, sulfides and gold.

CAPÍTULO III

1. DISCUSSÕES E CONCLUSÕES

1.1 Dificuldades Analíticas

A partir de trabalhos de campo e de uma *mélange* de técnicas analíticas, o Depósito de Príncipe foi descrito e caracterizado, contribuindo para a evolução do conhecimento na região. Alguns problemas, entretanto, foram enfrentados durante os procedimentos de amostragem e processamento para algumas análises, tais como os estudos de inclusões fluidas, geocronologia e isótopos estáveis. A principal causa destes problemas está relacionada a dificuldades de amostragem, envolvendo empecilhos como o estado de conservação de amostras, que frequentemente encontram-se intensamente alteradas por processos intempéricos, hidrotermais ou deformacionais. Outra dificuldade associada é a da escassez de determinadas rochas ou minerais, que impossibilitam trabalhos em larga escala, focando apenas em localidades restritas.

Para o caso das inclusões fluidas, deve-se ressaltar que o potencial máximo das análises por microtermometria não pôde ser explorado devido às dificuldades causadas pelas condições das amostras, como a recristalização e o fraturamento dos grãos de quartzo, além do tamanho diminuto da maioria das inclusões. Medições dos pontos eutético e de fusão do CO_2 auxiliariam em suposições acerca da composição do fluido, que possivelmente possui contribuições de KCl e $CaCl_2$, como sugerido por Queiroz (2001). Análises posteriores de todos os tipos de inclusões por espectroscopia Raman possibilitariam ter maiores certezas sobre os componentes da solução hidrotermal.

Para as análises geocronológicas de U-Pb em zircão, houve dificuldade para o processamento e interpretação dos dados devido à qualidade dos grãos deste mineral, que apresentavam grandes discordâncias entre suas razões e idades. Apenas foram utilizados cristais que apresentassem concordâncias entre 90% e 110%, o que reduziu bastante a quantidade de grãos nos diagramas da concórdia. No caso do Sm-Nd, há dúvidas com relação às amostras de Hidrotermalitos e Tectonitos devido a um possível metassomatismo de ETRs durante o hidrotermalismo.

Houve grandes dificuldades para realizar as análises de isótopos de C e O devido à escassez de veios de carbonato e à baixa quantidade de carbonato nos veios de quartzo, impossibilitando análises em grande quantidade. Para isótopos de S, trabalhos de microtermometria não foram possíveis devido à grande proporção de pirita presente nos veios, o que dificultou a seleção de grãos de outros sulfetos, não havendo, assim, pares minerais para o cálculo do fracionamento isotópico.

1.2 Correlações entre o Granito Príncipe e a Suíte Aurumina

Ao serem comparadas com trabalhos pretéritos, as características mineralógicas, texturais, deformacionais, geoquímicas e geocronológicas apresentadas neste trabalho levam à sugestão de que o Granito Príncipe seja uma intrusão pertencente, correlacionada ou sin-genética à Suíte Aurumina (Botelho & Silva, 2005). Esta proposta ressalta a importância e extensão de uma granitogênese peraluminosa Transamazônica (Botelho et al., 2002) ou Franciscana (Cordeiro, 2014), que ocorre desde o norte do estado de Goiás até o Tocantins.

O caráter peraluminoso do Granito Príncipe é ressaltado pela presença de granada, biotita e muscovita ígneos juntamente com os dados geoquímicos, que apresentam elevados valores no índice de saturação em Al. A natureza ígnea dos cristais de muscovita e granada foi averiguada pelas suas feições texturais e por dados de microssonda, onde os elevados teores de Ti e Mn, respectivamente, sugerem que estes minerais possuam origem magmática. Diagramas geoquímicos para identificar o contexto tectônico de formação indicam ambiente de colisão continental para esta litologia, estando de acordo com a Suíte Aurumina. Os dados geocronológicos U-Pb apontam idades paleoproterozoicas, com T_{DM} por Sm-Nd ligeiramente mais velhos e ε_{Nd} indicando leve retrabalhamento crustal.

1.3 Classificação do Tipo de Depósito

O Depósito Aurífero de Príncipe, assim como os demais depósitos do Distrito Aurífero Natividade e do Terreno Almas-Dianópolis (Alvarez, 2006), apresenta feições que se adequam ao modelo de Ouro Orogênico (Phillips & Powell, 2010). Entre estas características, se destacam as de que a mineralização ocorreu durante o Ciclo Brasiliano (Brito Neves & Fuck, 2013; Brito Neves & Fuck, 2014), que é o evento orogenético que produziu as zonas de cisalhamento transcorrentes da área e submeteu a região a metamorfismo regional sob fácies xisto verde. Outro aspecto é o caráter epigenético deste depósito, onde o hidrotermalismo neoproterozoico alterou rochas magmáticas paleoproterozoicas, originando uma paragênese neoformada a partir de metassomatismo em K, Na, Ca, Fe e metais base. Um terceiro fator é o forte controle estrutural, onde a precipitação de metais se concentrou no interior de uma sombra de pressão de escala regional, formando veios compostos essencialmente por quartzo, com menores proporções de carbonato, sulfetos e ouro.

1.4 Modelo Metalogenético

O sistema transcorrente do tipo *strike-slip* que se estabeleceu durante o Ciclo Brasiliano deu origem ao Depósito Aurífero de Príncipe, em que rochas paleoproterozoicas foram fortemente afetadas por eventos de metamorfismo, deformação e hidrotermalismo. De

acordo com os resultados de isótopos estáveis, o fluido hidrotermal possivelmente foi originado a partir da devolatilização metamórfica de rochas de diferentes origens, levando consigo Au e outros metais complexados a S reduzido.

Os estudos de inclusões fluidas apontam que o fluido hidrotermal possuía natureza aquo-carbônica, com baixa salinidade e baixo conteúdo de CO_2. Esta solução foi transportada através do sistema interconectado de falhas, fraturas e zonas de cisalhamento de diferentes ordens e escalas. Nas estruturas de 1ª ordem, tais como a Zona de Cisalhamento Cruz das Almas, predominaram processos como transporte e lixiviação de elementos químicos, enquanto nas estruturas de 2ª e 3ª ordem ocorreu a precipitação de metais e alojamento do minério em veios de quartzo. O processo de deformação ocorreu de maneira heterogênea de modo que, sob regime dúctil-rúptil, as rochas foram submetidas a milonitização em diferentes graus.

As rochas neoformadas apresentam discrepâncias geoquímicas com as litologias primárias, com seus minerais seguindo este mesmo padrão, observado pelos dados de microssonda. O metassomatismo em K, Na, Fe, Ca e Mg apontado por estes dados em combinação com as observações petrográficas indica reações hidrotermais de hidrólise, sericitização, saussuritização, silicificação, biotitização, cloritização, carbonatação e sulfetação.

Os valores de pressão calculados através dos estudos de inclusões fluidas encontram-se muito abaixo dos valores comuns para esta classe de depósitos, e a partir disso duas hipóteses foram levantadas. A primeira é de que este fato pode estar associado à sombra de pressão, que apresenta baixos valores barométricos por atuar como uma zona de alívio. Outra possibilidade parte da premissa de que a temperatura de homogeneização total das inclusões representa a temperatura mínima da mineralização, podendo, portanto, corresponder a valores mais elevados. A isócora formulada para o sistema aponta pressões de 699 bar para temperaturas de 300°C, que são próximas à temperatura máxima medida de 297°C, e de 964 bar para 320°C, mostrando que temperaturas ligeiramente maiores que a temperatura máxima obtida já se adequam às pressões esperadas para este tipo de depósito. Com respeito à temperatura da mineralização aurífera, dados de geotermometria de clorita e de inclusões fluidas incluem a maioria dos valores no intervalo entre 220°C e 370°C, correspondendo a valores típicos para esta modalidade de depósito (Witt & Vanderhor, 1998).

A precipitação do minério ocorreu a partir da desestabilização físico-química do fluido hidrotermal. O Au na sua forma livre possivelmente se depositou a partir da queda do

gradiente barométrico, causada pela sombra de pressão. Para o caso do Au incluso nos sulfetos, a precipitação ocorreu através da reação com as rochas tonalíticas-granodioríticas da Suíte Rio do Moleque. A percolação pervasiva da solução hidrotermal provocou a alteração das rochas em diferentes intensidades, culminando nos veios mineralizados.

1.5 Sugestões para Trabalhos Futuros

Para melhor entender as características das mineralizações auríferas e correlaciona-las com depósitos ou ocorrências nas proximidades do Depósito de Príncipe, estudos devem ser feitos ao longo do Distrito Aurífero Natividade, no Terreno Almas-Dianópolis e ao longo do Lineamento Transbrasiliano. Recomenda-se estudos de detalhe nos depósitos de Serra de Natividade e ao longo das zonas de cisalhamento que cortam esta área de estudo. O que se espera com estas sugestões envolve compreender as diferenças e semelhanças entre os mecanismos que levam às mineralizações auríferas em diferentes escalas e profundidades.

Uma série de potenciais depósitos orogênicos correlacionados ao Depósito Aurífero de Príncipe aguarda para ser descoberta, visto que eles são formados a partir dos mesmos mecanismos que os descritos para este depósito. Estruturas brasilianas canalizadoras de fluidos hidrotermais se estendem por centenas de quilômetros e certamente devem ser encaradas como guias exploratórios. Campanhas prospectivas nos arredores deste e de outros depósitos do Distrito Aurífero Natividade devem seguir as zonas de cisalhamento de *trend* N10°W-N20°E, buscando *traps* estruturais, interseções de estruturas e contatos litológicos, por serem ambientes eficientes para precipitação de metais.

2. REFERÊNCIAS

ABDALLAH, S. 2011. Interpretação litoquímica das rochas graníticas do embasamento da folha arraias. Anais do XIII Congresso Brasileiro de Geoquímica, Gramado, Rio Grande do Sul, Brasil.

ABDALLAH, S., MENEGHINI, P.F.V.B. 2013. Carta Geológica 1:250.000 da Folha SD.23-V-A Arraias. Serviço Geológico do Brasil (CPRM), Goiânia, Brasil.

AGP-LA - AeroGeoPhysica LatinoAmerica. 2006. Relatório Final do Levantamento e Processamento dos Dados Magnetométricos e Gamaespectométricos do Projeto Aerogeofísico do Tocantins.

ALLÈGRE, C.J. 2008. Isotope Geology. Cambridge University Press, New York, United States. 534 p.

ALMEIDA, F.F.M., HASUI, Y., BRITO NEVES, B.B., FUCK, R.A., 1981. Brazilian structural provinces: an introduction. Earth Science Reviews, 17, 1-29.

ALVARENGA, C.J.S., DARDENNE, M.A., BOTELHO, N.F., MACHADO, M.A., LIMA, O.N.B., ALMEIDA, T. 2007. Relatório Final das Folhas Monte Alegre, Cavalcante e Nova Roma. Programa Geologia do Brasil (PGB/LGB), Convenio UNB/FINATEC/CPRM.

ALVAREZ, M.C.A. 2006. Mineralizações de ouro no terreno Almas-Dianópolis-TO: guias de exploração mineral. Dissertação (Mestrado em Geologia)-Universidade de Brasília, Brasília. 67 p.

ALYIARI, F., RASTAD, E., GOLDFARB, R.J., SHARIF, J.A. 2014. Geochemistry of hydrothermal alteration at the Qolqoleh gold deposit, northern Sanandaj–Sirjan metamorphic belt,

northwestern Iran: Vectors to high-grade ore bodies. Journal of Geochemical Exploration, 140, 111-125.

ARAÚJO FILHO, J.O. 2000. The Pirineus Syntaxis: na example of the intersection between Brasiliano fold-trust belts in Central Brazil and implications for the tectonic evolution of western Gondwana. Revista Brasileira de Geociências, 30, 144-148.

BAKKER, R.J. 2003. Package FLUIDS 1. Computer programs for analysis of fluid inclusion data and for modelling bulk fluid properties. Chemical Geology, 194, 3-23.

BARBOSA, V.C.F., SILVA, J.B.C.D. 2005. Deconvolução de Euler: passado, presente e futuro - um tutorial. Revista Brasileira de Geofísica, 23, 243-250.

BARBOSA, V.C.F., SILVA, J.B.C.D., MEDEIROS, W.E. 1999. Stability analysis and improvement of structural index estimation in Euler deconvolution. GEOPHYSICS, 64(1), 48–60.

BARLEY, M.E., GROVES, D.I. 1992. Supercontinent cycles and the distribution of metal deposits through time. Geology, 20, 291-294.

BIERLEIN, F.P., ARNE, D.C., CARTWRIGHT, I. 2004. Stable isotope (C, O, S) systematics in alteration haloes associated with orogenic gold mineralization in the Victorian gold province, SE Australia. Geochemistry: Exploration, Environment, Analysis, 4, 191–211.

BIERLEIN, F.P., GROVES, D.I., GOLDFARB, R.J., DUBÉ, B. 2006. Lithospheric controls on the formation of provinces hosting giant orogenic gold deposits. Mineralium Deposita, 40, 874-886.

BIERLEIN, F.P., GROVES, D.I., CAWOOD, P.A. 2009. Metallogeny of accretionary orogens – The connection between lithospheric processes and metal endowment. Ore Geology Reviews, 36, 282-292.

BLAKELY, R.J. 1995. Potential theory in gravity and magnetic applications. Cambridge University Press, Cambridge, XIX + 441 p.

BLUM M.L.B., JOST H., MORAES R.A.V. & PIRES A.C.B. 2003. Caracterização dos complexos ortognáissicos arqueanos de Goiás por gamaespectrometria aérea. Revista Brasileira de Geociências, 33, 147-152.

BODNAR, R.J. 1993. Revised equation and table for determining the freezing point depression of H_2O-NaCl solutions. Geochimica et Cosmochimica Acta, 57, 683-684.

BODNAR, R.J. 2003. Introduction to aqueous fluid systems. In: SAMSON, I., ANDERSON, A., MARSHALL, D. Eds. Fluid Inclusions: Analysis and interpretation. Mineralogical Association of Canada, short course 32, 81-99.

BOTELHO, N.F., ALVARENGA, C.J.S., MENESES, P.R., D'EL-REY SILVA, L.J.H. 1995. Mapa geológico da região de Teresina de Goiás, GO. Brasília, Universidade de Brasília.

BOTELHO, N.F., ALVARENGA, C.J.S., DARDENNE, M.A., CAMPOS, J.E.G. 1998. Mapa geológico da região de Cavalcante, GO. Brasília, Universidade de Brasília.

BOTELHO, N.F., ALVARENGA, C.J.S., MENEZES, P.R., D'EL-REY SILVA, L.J.H. 1999. Suíte Aurumina: Uma suíte de granitos paleoproterozoicos, peraluminosos e sin-tectônicos na Faixa Brasília. Anais do VII Simpósio de Geologia do Centro-Oeste e X Simpósio de Geologia de Minas Gerais, Brasília, Brasil. 1 p.

BOTELHO, N.F., MOURA, M.A., ALVARENGA, C.J.S., DANTAS, E.L., DARDENNE, M.A., CAMPOS, J.E.G., MENESES, P.R., BRITO, A.P. 2002. Granitogênese peraluminosa Transamazônica no embasamento da Faixa Brasília e seu significado tectônico. Anais do 41° Congresso Brasileiro de Geologia, João Pessoa, Brasil. 1 p.

BOTELHO, N.F., SILVA, D.V.G. 2005. Mineralizações de Au e PGE hospedadas em rochas graníticas peraluminosas do nordeste de goiás: discussão sobre depósitos não convencionais de platinoides. Anais do I Simpósio de Metalogenia, Gramado, Brasil.

BOTELHO, N.F., FUCK, R.A., DANTAS, E.L., LAUX, J.L., JUNGES, S.L. 2006. The paleoproterozoic peraluminous aurumina granite suite, Goiás and Tocantins: whole rock chemistry and Sm-Nd isotopic constraints. The Paleoproterozoic record of the São Francisco craton, Brazil. IGCP 509, Brazil, September 9-21.

BRITO NEVES, B.B., CORDANI, U.G. 1991. Tectonic evolution of South America during the Late Proterozoic. In: STERN, R.J., VAN SCHMUS, W.R. Crustal evolution in the late Proterozoic. Precambrian Research, 53, 23-40.

BRITO NEVES, B.B., SA, J.M., NILSON, A.A., BOTELHO, N.F. 1995. A tafrogênese estateriana nos blocos paleoproterozoicos da América do Sul e processos subsequentes. Genomos, 3, 1-21.

BRITO NEVES, B. B., WINGE, M., CARNEIRO, M. A. 1996. Orogêneses precedendo e tafrogêneses sucedendo Rodínia na América do Sul. Boletim IG-USP, Série Científica [online] 27, 1-40.

BRITO NEVES, B.B. FUCK, R.A. 2013. Neoproterozoic evolution of the basement of the South-American platform. Journal of South American Earth Sciences, 47, 72-89.

BRITO NEVES, B.B. FUCK, R.A. 2014. The basement of the South American platform: Half Laurentian (N-NW) + half Gondwanan (E-SE) domains. Precambrian Research, 244, 75-86.

BÜHN, B., SANTOS, R.V., DARDENNE, M.A., OLIVEIRA, C.G. 2012. Mass-dependent and mass-independent sulfur isotope fractionation ($\delta^{34}S$ and $\delta^{33}S$) from Brazilian Archean and Proterozoic sulfide deposits by laser ablation multi-collector ICP-MS. Chemical Geology 312–313, 163–176.

CARITAT, P., HUTCHEON, I., WALSHE, J.L. 1993. Chlorite geothermometry: A review. Clays and Clay Minerals, 41, 219-239.

CATHELINEAU, M. 1988. Cation site occupancy in chlorites and illites as a function of temperature. Clay Minerals, 23, 471-485.

CAWOOD, P.A., BUCHAN, C. 2007. Linking accretionary orogenesis with supercontinent assembly, Earth-Science Reviews, 82, 217-256.

CHAPPEL, B.W., WHITE, J.R. 2001. Two contrasting granite types: 25 years later. Australian Journal of Earth Sciences, 48, 489-499.

COPLEN, T.B. 1994. Reporting of stable hydrogen, carbon, and oxygen isotopic abundances (technical report). Pure & Applied Chemistry, 66, 273-276.

CORDEIRO, P.F.O. 2014. Compartimentação geológica e geocronológica dos terrenos do embasamento norte da Faixa Brasília. Tese de Doutorado da Universidade de Brasília, 156 p.

CORRÊA, R.S., SOUSA, L. A. 2012. Projeto Natividade: Subárea IX. In: OLIVEIRA, C.G., VIDOTTI, R.M., DANTAS, E.L., SOUZA, V.S., CHEMALE, F.J. Projeto Natividade: Relatório de Graduação do Curso de Geologia da Universidade de Brasília, Brasil.

CORRÊA, R.S., SOUSA, I.M.C., FILGUEIRAS, B.C., OLIVEIRA, C.G. 2013. O Distrito aurífero Natividade, Faixa Brasília Setentrional. Anais do XVIII Simpósio de Geologia do Centro-Oeste, Cuiabá, Brasil, 4 p.

CORRÊA, R.S., OLIVEIRA, C.G., VIDOTTI, R.M. 2014. Regional-scale auriferous pressure shadow controlled by Transbrasiliano strike-slip shear zones, Tocantins Province, Brazil. Anais do VI Simpósio Brasileiro de Exploração Mineral, Ouro Preto, Brasil, 2p.

CORREIA FILHO, F.C.L., SA, A.M. 1980. Projeto Natividade. Goiania, DNPM/CPRM. Vol. 6.

CRUZ, E.L.C.C., KUYUMJIAN, R.M. 1993. O embasamento da porção norte da Faixa Brasília na região de Almas-Dianópolis (TO) e seu posicionamento geodinâmico durante o brasiliano. Anais do II Simpósio sobre o Craton do São Francisco, Bahia, Brasil. 3p.

CRUZ, E.L.C.C., KUYUMJIAN, R.M. 1998. Geology and tectonic evolution of the Tocantins granite-greenstone terrane: Almas-Dianópolis region, Tocantins State, central Brasil. Revista Brasileira de Geociências, 28, 173-172.

CRUZ, E.L.C.C., KUYUMJIAN, R.M. 1999. Mineralizações Auríferas Filoneanas do Terreno Granito-Greenstone do Tocantins. Revista Brasileira de Geociências, 29, 291-298.

DAHLQUIST, J.A., GALINDO, C., PANKHURST, R.J., RAPELA, C.W., ALASINO, P.H., SAAVEDRA, J., FANNING, C.M. 2007. Magmatic evolution of the Peñón Rosado granite: Petrogenesis of garnet-bearing granitoids. Lithos, 95, 177-207.

DAVIS, G.H., BUMP, A.P., GARCÍA, P.E., AHLGREN, S.G. 2000. Conjugate Riedel deformation band shear zones. Journal of Structural Geology, 22, 169–190.

DAVIS, J.C. 1973. Statistics and data analysis in geology. Kansas Geological Survey. 550 p.

DE BOORDER, H. 2012. Spatial and temporal distribution of the orogenic gold deposits in the Late Palaeozoic Variscides and Southern Tianshan: How orogenic are they? Ore Geology Reviews, 46, 1-31.

DE LA ROCHE, H., LETERRIER, J., GRANDCLAUDE, P., MARCHAL, M. 1980. A classification of volcanic and plutonic rocks using R_1R_2-diagram and major element analyses – its relationships with current nomenclature. Chemical Geology, 29, 183-210.

DEER, W.A., HOWIE, R.A. & ZUSSMAN, J. 2013. An introduction to the rock forming minerals, 3rd edition. Mineralogical Society. 510 p.

DIAMOND, L.W. 1990. Fluid inclusion evidence for P-V-T-X evolution of hydrothermal solutions in Late-Alpine gold-quartz veins at Brusson, Val d'Ayas, NW Italian Alps. American Journal of Science, 290, 912-958.

DIAMOND, L.W. 1996. Isochoric paths in immiscible fluids and the interpretation of multicomponent fluid inclusions. Geochimica et Cosmochimica Acta, 60, 3825-3834.

DIAMOND, L.W. 2001. Review of the systematics of CO_2–H_2O fluid inclusions. Lithos, 55, 69-99.

DING, T., VALKIERS, S., KIPPHARDT, H. DE BRIÈVE, P., TAYLOR, P.D.P., GONFIANTINI, R., KROUSE, R. 2001. Calibrated sulfur isotope abundace ratios of three IAEA sulfur isotope reference materials and V-CDT with a reassessment of the atomic weight of sulfur. Geochimica et Cosmochimica Acta, 65, 2433–2437.

DUBÉ, B., GOSSELIN, P. 2007. Greenstone-hosted quartz-carbonate vein deposits (orogenic, mesothermal, lode gold, shear-zone-related quartz-carbonate or gold-only deposits). In: Goodfellow, W.D., ed., Mineral Deposits of Canada: A Synthesis of Major Deposit-Types, District Metallogeny, the Evolution of Geological Provinces, and Exploration Methods: Geological Association of Canada, Mineral Deposits Division, Special Publication No. 5, 49-73.

ETCHECOPAR, A. MALAVIEILLE, J. 1987. Computer models of pressure shadows: a method for strain measurement and shear-sense determination. Journal of Structural Geology, 9, 667-677.

FIANCO, C.B., VIDOTTI, R.M., PIRES, A.C.B., CARMELO, A.C. 2012. Prospecting phosphorites using airborne geophysics in northeastern Goiás state – Brazil. Revista Brasileira de Geofísica, 30, 459-471.

FRIMMEL, H.E. 2008. Earth's continental crustal gold endowment. Earth and Planetary Science Letters, 267, 45–55.

FROST, B.R., BARNES, C.G., COLLINS, W.J., ARCULUS, R.J., ELLIS, D.J., FROST, C.D. 2001. A geochemical classification for granitic rocks. Journal of Petrology, 42, 2033-2048.

FUCK, R.A. 1994. A Faixa Brasília e a Compartimentação Tectônica na Província Tocantins. Anais do IV Simpósio de Geologia do Centro-Oeste, Brasília, Brasil. 4 p.

FUCK, R.A., DANTAS, E.L., PIMENTEL, M.M., BOTELHO, N.F., ARMSTRONG, R., LAUX, J.H., JUNGES, S.L., SOARES, J.E., PRAXEDES, I.F. 2014. Paleoproterozoic crust-formation and reworking events in the Tocantins Province, central Brazil: A contribution for Atlantica supercontinent reconstruction. Precambrian Research, 244, 53-74.

FUCK, R.A., PIMENTEL, M.M., SOARES, J.E.P., DANTAS, E.L. 2005. Compartimentação da Faixa Brasília. Anais do IX Simpósio de Geologia do Centro-Oeste, Goiânia, Brasil. 2 p.

GOLDFARB, R.J., GROVES, D.I., GARDOLL, S. 2001. Orogenic gold and geologic time: a global synthesis. Ore Geology Reviews, 18, 1–75.

GOLDFARB, R.J., BAKER, T., DUBÉ, B., GROVES, D.I., HART, C.J.R., GOSSELIN, P. 2005. Distribution, character, and genesis of gold deposits in metamorphic terranes. Economic Geology 100th anniversary volume, 407-450.

GOLDFARB, R.J., BRADLEY, D., LEACH, D.L. 2010. Secular variation in economic geology. Economic Geology, 105, 459-465.

GORAYEB, P.S.S., COSTA, J.B.S., LEMOS, R.L., GAMA JUNIOR, T., BEMERGUY, R.L., HASUI, Y. 1988. O pré-cambriano da região de Natividade, GO. Revista Brasileira de Geociências, 18, 391-397.

GROVES, D.I., GOLDFARB, R.J., GEBRE-MARIAM, M., HAGEMANN, S., ROBERT, F., 1998. Orogenic gold deposits: A proposed classification in the context of their crustal distribution and relationship to other gold deposit types. Ore Geology Reviews, 13, 7–27.

GROVES, D.I., BIERLEIN, F.P. 2007. Geodynamic settings of mineral deposit systems. Journal of the Geological Society, 164, 19-30.

HEY, M.H. 1954. A new review of the chlorites. Mineralogical Magazine, 30, 277-292.

HOEFS, J. 2009. Stable Isotope Geochemistry. Springer, Berlin, Germany. 293 p.

HRONSKY, J.M.A., GROVES, D.I., LOUCKS, R.R., BEGG, G.C. 2012. A unified model for gold mineralization in accretionary orogens and implications for regional-scale exploration target methods. Mineralium Deposita, 47, 339-358.

IBGE (Instituto Brasileiro de Geografia e Estatística). 2007. Mapa Geológico 1:1.000.000 do estado do Tocantins, Pará, Brasil.

JAQUES, A.L., WELLMAN, P., WHITAKER, A. & WYBORN, D. 1997. High-resolution Geophysics in Modern Geological Mapping. AGSO Journal of Australian Geology & Geophysics, 17, 159-173.

KATZA, Y., WEINBERGERB, R., AYDINC, A. 2004. Geometry and kinematic evolution of Riedel shear structures, Capitol Reef National Park, Utah. Journal of Structural Geology, 26, 491–501.

KERRICH, R. 1987. The stable isotope geochemistry of Au-Ag vein deposits in metamorphic rocks. Mineralogical Association of Canada Short Course Handbook, 13, 287–336.

KLEIN, E.L., HARRIS, C., GIRET, A., MOURA, C.A.V. 2007. The Cipoeiro gold deposit, Gurupi Belt, Brazil: Geology, chlorite geochemistry, and stable isotope study. Journal of South American Earth Sciences, 23, 242-255.

KLEIN, E.L., HARRIS, C., GIRET, A., MOURA, C.A.V., ANGÉLICA, R.S. 2005. Geology and stable isotope (O, H, C, S) constraints on the genesis of the Cachoeira gold deposit, Gurupi Belt, northern Brazil. Chemical Geology, 221, 188-206.

KNIGHT, C.L., BODNAR, R.J. 1989. Synthetic fluid inclusions: IX. Critical PVTX properties of $NaCl-H_2O$ solutions. Geochimica et Cosmochimica Acta, 53, 3-8.

KUYUMJIAN, R.M., ARAÚJO FILHO, J.O. 2005. Depósitos e ocorrências de ouro no terreno arqueano-paleoproterozoico de Almas-Dianópolis (TO): Evidências da importância metalogenética do Evento Brasiliano. Revista Brasileira de Geociências, 35, 611-614.

KUYUMJIAN, R.M., CRUZ, E.L.C.C., ARAÚJO FILHO, J.O., MOURA, M.A., GUIMARÃES, E.M., PEREIRA, K.M.S. 2012. Geologia e ocorrências de ouro do Terreno Granito-Greenstone do Tocantins, TO: síntese do conhecimento e parâmetros para exploração mineral. Revista Brasileira de Geociências, 42, 213-228.

LE BAS, M.J., STRECKEISEN, A.L. 1991. The IUGS systematics of igneous rocks. Journal of the Geological Society, 148, 825-833.

LUDWIG, K.R. 2008. User's manual for Isoplot 3.70. Berkeley Geochronology Center Special Publication No. 4. 76 p.

MANIAR, P.D., PICCOLI, P.M. 1989. Tectonic discrimination of granitoids. Geological Society of America Bulletin, 101, 635-643.

MARQUES, G.C., 2009. Geologia dos grupos Araí e Serra da Mesa e seu embasamento no sul do Tocantins. Dissertação de Mestrado da Universidade de Brasília, 122 p.

MCCUAIG, T.C., KERRICH, R. 1998. P—T—t—deformation—fluid characteristics of lode gold deposits: evidence from alteration systematics. Ore Geology Reviews, 12, 381-453.

MILLER, C.F., STODDARD, E.F. 1981. The role of manganese in the paragenesis of magmatic garnet: an example from the Old Woman Piute Range, California. J. Geol. 89, 233–246.

MILLER, H.G., SINGH, V. 1994. Potential field tilt - a new concept for location of potential field sources. Journal of Applied Geophysics, 32, 213-217.

NACHIT, H., IBHI, A., ABIA, E.H., OHOUD, M.B. 2005. Discrimination between primary magmatic biotites, reequilibrated biotites and neoformed biotites. Compters Rendus Geoscience, 337, 1415-1420.

NELSON, B.W., ROY, R. 1958. Synthesis of the chlorites and their structural and chemical constitution. The American Mineralogist, 43, 707-725.

PEARCE, J.A., HARRIS, N.B.W., TINDLE, A.G. 1984. Trace element discrimination diagrams for the tectonic interpretation of granitic rocks. Journal of Petrology, 25, 956-983.

PERI, V.G., POMPOSIELLO, M.C., FAVETTO, A., BARCELONA, H. ROSSELLO, E. A. 2013. Magnetotelluric evidence of the tectonic boundary between the Río de La Plata Craton and the Pampean terrane (Chaco-Pampean Plain, Argentina): The extension of the Transbrasiliano Lineament. Tectonophysics, 608, 685-699.

PHILLIPS, J.D. 1997. Potential-field geophysical software for the PC, version 2.2. US Geological Survey Open-File Report 97-725.

PHILLIPS, J.D. 2001. Designing matched bandpass and azimuthal filters for the separation of potential-field anomalies by source region and source type. Australian Society of Exploration Geophysicists, 15th Geophysical Conference and Exhibition, Expanded Abstracts CD-ROM, 4p.

PHILLIPS, G.N., EVANS, K.A. 2004. Role of CO2 in the formation of gold deposits. Nature, 429, 860–863.

PHILLIPS, G.N., POWELL, R., 2009. Formation of gold deposits: Review and evaluation of the continuum model. Earth Science Reviews, 94, 1–21.

PHILLIPS, G.N., POWELL, R., 2010. Formation of gold deposits: a metamorphic devolatilization model. Journal of Metamorphic Geology, 28, 689–718.

PIMENTEL, M.M., FUCK, R.A. 1992. Neoproterozoic crustal accretion in central Brazil. Geology, 20, 375-379.

PIMENTEL, M.M., FUCK, R.A., BOTELHO, N.F., 1999. Granites and the geodynamic history of the neoproterozoic Brasília Belt, Central Brazil: a review. Lithos, 46, 463–483.

PIRAJNO, F. 2009. Hydrothermal processes and mineral systems. Springer, Berlin, 1250 p.

PIRAJNO, F. 2010. Intracontinental strike-slip faults, associated magmatism, mineral systems and mantle dynamics: examples from NW China and Altay Sayan (Siberia). Journal of Geodynamics, 50, 325-346.

PIRES, A.C.B. 1995. Identificação geofísica de áreas de alteração hidrotermal, Crixás-Guarinos, Goiás. Revista Brasileira de Geociências, 25, 61-68.

OLIVEIRA, C.G., VIDOTTI, R.M., DANTAS, E.L., SOUZA, V.S., CHEMALE, F.J. 2012. Projeto Natividade: Relatório de Graduação do Curso de Geologia da Universidade de Brasília, Brasil.

QUEIROZ, J.P.C., 2001. Geologia e mineralização aurífera da área de Chapada-TO. Dissertação de Mestrado da Universidade Federal do Pará, 118 p.

REID, A.B., ALLSOP, J.M., GRANSER, H., MILLETT, A.J., SOMERTON, I.W. 1990. Magnetic interpretation in three dimensions using Euler deconvolution. Geophysics, 55, 80-91.

ROBB, L. 2005. Introduction to ore-forming processes. Blackwell Publishing, Oxford, 386 p.

ROEDDER, E., BODNAR, R.J. 1980. Geologic pressure determinations from fluid inclusion studies. Annual Reviews Earth Planetary Sciences, 8, 263-301.

ROEST, W.R., VERHOEF, J., PILKINGTON, M. 1992. Magnetic interpretation using the 3D analytic signal. Geophysics, 57, 116-125.

SABOIA, A.M., 2009. O vulcanismo em Monte do Carmo e litoestratigrafia do grupo Natividade, estado de Tocantins. Dissertação de Mestrado da Universidade de Brasília, 96 p.

SAGGERSON, E.P., TURNER, L.M. 1982. General comments on the identification of chlorites in thin sections. Mineralogical Magazine, 46, 469-473.

SANTOS, R.V., OLIVEIRA, C.G., PARENTE, C.V., GARCIA, M.G.M., DANTAS, E.L. 2013. Hydrothermal alteration related to a deep mantle source controlled by a Cambrian intracontinental strike-slip fault: Evidence for the Meruoca felsic intrusion associated with the Transbraziliano Lineament, Northeastern Brazil. Journal of South American Earth Sciences, 43, 33-41.

SARANGI, S., SARKAR, A., SRINIVASAN, R., PATEL, S.C. 2012. Carbon isotope studies of auriferous quartz carbonate veins from two orogenic gold deposits from the Neoarchean Chitradurga schist belt, Dharwar craton, India: Evidence for mantle/magmatic source of auriferous fluid. Journal of Asian Earth Sciences. 52, 1-11.

SCHOBBENHAUS, C., CAMPOS, D.A., DERZE, G.R. & ASMUS, H.E. 1984. Geologia do Brasil: Departamento Nacional da Produção Mineral, Brasília, 501 p.

SHAND, S.J. 1943. The Eruptive Rocks, 2nd edition. New York: John Wiley, 444p.

SHEPHERD, T.J., RANKIN, A.H., ALDERTON, D.H.M. 1985. A practical guide to fluid inclusion studies. British Library, London. 239 p.

SIBSON, R.H. 1994. Crustal stress, faulting and fluid flow. Geological Society, 78, 69-84.

SIBSON, R.H. 1996. Structural permeability of fluid-driven fault-fracture meshes. Journal of Structural Geology, 18, 1031-1042.

SIBSON, R.H., SCOTT, J. 1998. Stress/fault controls on the containment and release of overpressured fluids: Examples from gold-quartz vein systems in Juneau, Alaska; Victoria, Australia and Otago, New Zealand. Ore Geology Reviews, 13, 293-306.

SOUSA, I.M.C., OLIVEIRA, C.G. 2013. A Zona de cisalhamento Cruz das Almas e seu contexto tectônico, Faixa Brasília Setentrional. Anais do XVIII Simpósio de Geologia do Centro-Oeste, Cuiabá, Brasil, 5 p.

STEFÁNSSON, A., SEWARD, T.M. 2004. Gold(I) complexing in aqueous sulphide solutions to 500°C at 500 bar. Geochimica Cosmochimica Acta, 68, 4121–4143.

STRIEDER, A.J. & SUITA, M.T.F. 1999. Neoproterozoic geotectonic evolution of Tocantins Structural Province, central Brazil. J. Geodynamics, 28, 267-289.

SUN, S.S., MCDONOUGH, W.F. 1989. Chemical and Isotopic Systematics of oceanic basalts: implications for Mantle Composition and Processes. In A.D. Saunders and M.J. Norry (eds.) Magmatism in the Ocean Basins , Spec. Publ. Vol. Geol. Soc. Lond., 42, 313-345.

TCHALENKO, J.S. 1970. Similarities between shear zones of different magnitudes. Geological Society of America Bulletin, 81,1625-1639.

THODE, H.G. 1991. Sulphur isotopes in nature and the environment: An overview. In: KROUSE, H.R., GRINENKO, V.A. Stable Isotopes in the Assessment of Natural and Anthropogenic Sulphur in the Environment. 26 p.

THOMPSON, D. 1982. ”EULDPH: A new technique for making computer-assisted depth estimates from magnetic data.” Geophysics, 47, 31–37.

TINDLE, A.G. & WEBB, P.C. 1990. Estimation of lithium contents in trioctahedral micas using microprobe data: application to micas from granitic rocks. European Journal of Mineralogy, 2, 595-610.

TROUW, R.A.J., PASSCHIER, C.W., WIERSMA, D.J. 2010. Atlas of Mylonites– and related microstructures. Springer, Heidelberg, 336 p.

WILLIAMS-JONES, A.E., BOWELL, R.J., MIGDISOV, A.A. 2009. Gold in Solution. Elements, 5, 281-287.

WILSON, M. 1989. Igneous Petrogenesis: A Global Tectonic Approach. Springer, Dordrecht, 466 p.

WHITNEY, D.L., EVANS, B.W. 2010. Abbreviations for names of rock-forming minerals. American Mineralogist, 95, 185-187.

WITT, W.K., VANDERHOR, F. 1998. Diversity within a unified model for Archaean gold mineralization in the Yilgarn Craton of Western Australia: An overview of the late-orogenic, structurally-controlled gold deposits. Ore Geology Reviews, 13, 29–64.

ZERFASS, H., CHEMALE, F.J. 2011. Geologia estrutural em ambiente rúptil: fundamentos físicos, mecânica de fraturas e sistemas de falhas naturais. Terræ Didatica, 7, 75-85.

ZEZIN, D.Y., MIGDISOV, A.A., WILLIAMS-JONES, A.E. 2007. The solubility of gold in hydrogen sulfide gas: An experimental study. Geochimica et Cosmochimica Acta, 71, 3070-3081.

ZHANG, Y.G., FRANTZ, J.D. 1987. Determination of homogenization temperatures and densities of supercritical fluids in the system NaCl-KCl-$CaCl_2$-H_2O using synthetic fluid inclusions. Chemical Geology, 64, 335-350.

ZHU, Y., AN, F., TAN, J. 2011. Geochemistry of hydrothermal gold deposits: A review. Geoscience Frontiers, 2, 367-37.

TABELAS/TABLES

Table 1. Príncipe Granite's Whole Rock Geochemical Data

Rock	PG	PG	PG	PG	PG	PG	PG	PG	PG	PG
SiO_2	72.50	73.73	72.07	74.02	73.33	72.30	70.93	76.3	76.13	72.61
Al_2O_3	14.38	13.97	14.06	13.23	13.90	14.19	14.33	12.23	14.41	15.26
Fe_2O_3	1.90	1.45	2.32	1.91	1.51	1.80	2.63	1.37	0.3	0.98
TiO_2	0.28	0.13	0.28	0.19	0.14	0.24	0.37	0.17	<0.01	0.11
MgO	0.37	0.55	0.48	0.37	0.31	0.37	0.56	0.32	0.19	0.22
MnO	0.03	0.02	0.03	0.03	0.04	0.02	0.02	0.02	<0.01	0.01
CaO	0.71	0.24	0.95	1.20	1.21	1.04	1.15	1.02	0.56	0.4
Na_2O	3.22	3.12	3.04	4.14	3.78	3.15	2.89	3.54	6.13	2.05
K_2O	5.37	4.96	5.30	3.38	4.11	5.43	5.39	3.71	0.99	7.03
P_2O_5	0.21	0.04	0.14	0.07	0.08	0.10	0.24	0.03	0.08	0.05
Cr_2O_3	0.002	<0.002	<0.002	<0.002	<0.002	<0.002	-	-	-	-
LOI %	0.8	1.5	1.0	1.2	1.3	1.1	1.2	1.1	1.9	1.1
TOT %	99.79	99.75	99.67	99.69	99.77	99.78	99.69	99.81	99.9	99.82
Ag	0.1	<0.1	<0.1	<0.1	<0.1	<0.1	0.2	0.1	0.1	0.2
As	<0.5	<0.5	1.0	<0.5	<0.5	0.6	<0.5	<0.5	10.7	0.6
Au	14.1	11.9	0.9	2.3	6.3	<0.5	<0.5	<0.5	66.1	<0.5
Ba	523	465	902	748	624	784	807	417	150	431
Be	3	5	2	2	2	1	<1	2	4	<1
Bi	0.6	<0.1	<0.1	<0.1	0.1	<0.1	<0.1	<0.1	0.4	<0.1
Cd	0.1	<0.1	<0.1	<0.1	<0.1	<0.1	<0.1	<0.1	<0.1	<0.1
Ce	180.3	37.0	167.1	82.8	19.7	140.1	140.6	121.6	9.9	36
Co	41.2	132.8	102.8	138.9	117.4	51.6	92.1	64.2	53.5	84.1
Cr	-	-	-	-	-	-	<20	<20	<20	<20
Cs	7.3	5.7	1.9	1.7	2.5	5.4	1.4	2.2	0.9	2.1
Cu	7.3	0.5	6.0	3.6	1.7	0.2	8.2	0.8	5.7	0.3
Dy	2.87	2.98	2.90	6.20	2.71	1.86	1.68	1.47	1.22	0.67
Er	0.96	1.45	1.53	3.62	2.06	0.75	0.67	0.48	0.56	0.1
Eu	0.68	0.48	0.65	0.80	0.31	0.58	0.43	0.51	0.34	0.47
Ga	27.3	25.6	22.3	18.1	18.7	21.0	21.2	16.2	16.5	23.8
Gd	6.52	4.06	5.12	6.96	1.98	4.17	3.96	4.4	1.04	2.87
Hf	5.8	3.5	5.7	5.0	3.8	5.0	7	5.2	1.5	0.8
Hg	<0.01	<0.01	<0.01	<0.01	<0.01	<0.01	<0.01	<0.01	<0.01	<0.01
Ho	0.43	0.51	0.56	1.27	0.63	0.27	0.27	0.18	0.25	0.06
La	97.2	46.2	90.3	57.9	3.8	66.2	42	52	6.3	17.9
Lu	0.14	0.19	0.16	0.44	0.36	0.10	0.1	0.07	0.08	0.01
Mo	0.1	0.1	0.2	<0.1	0.1	0.1	0.9	0.3	0.2	0.1
Nb	12.8	13.7	12.8	14.3	18.0	8.2	9.4	6.2	5.6	6.3
Nd	83.5	27.4	58.4	35.6	4.1	50.0	34.4	44	4.4	15.9
Ni	2.0	1.4	2.6	2.2	2.3	2.1	3.7	1.4	0.6	1.2
Pb	8.1	3.4	12.2	6.8	10.4	8.1	10.2	6.5	3.9	7.7
Pr	23.58	8.31	17.74	10.42	0.95	14.70	10.04	12.39	1.07	4.25
Rb	399.5	395.6	278.8	119.7	142.2	286.7	263.7	169.3	45.8	196
Sb	<0.1	<0.1	<0.1	<0.1	<0.1	<0.1	<0.1	<0.1	<0.1	<0.1
Sc	3	3	5	4	3	3	4	3	<1	4
Se	<0.5	<0.5	<0.5	<0.5	<0.5	<0.5	<0.5	<0.5	<0.5	<0.5
Sm	12.48	4.76	8.28	6.77	1.45	7.58	6.47	6.99	0.87	3.83
Sn	5	6	2	3	4	3	<1	2	2	2
Sr	86.8	55.0	155.2	154.6	150.3	134.2	166	185.4	80	102.4
Ta	1.4	1.8	0.9	1.6	2.1	0.8	0.5	0.9	1.3	0.6
Tb	0.65	0.56	0.59	1.06	0.39	0.42	0.39	0.37	0.23	0.22
Th	52.5	31.4	56.0	16.3	18.6	49.5	63.8	46	2.4	10.7
Tl	0.6	0.6	0.7	0.3	0.2	0.5	0.6	0.4	<0.1	<0.1
Tm	0.15	0.20	0.21	0.56	0.33	0.10	0.1	0.07	0.08	0.01
U	11.7	6.8	3.5	2.7	6.7	4.3	3.7	9	11.3	1.7
V	29	20	22	16	13	15	30	11	<8	<8
W	286.9	949.7	814.4	1006.4	791.1	306.9	865.6	561.1	569.4	821.1
Y	14.7	17.9	16.7	42.0	20.2	9.0	6.9	4.7	6.6	3
Yb	0.92	1.28	1.14	3.12	2.28	0.81	0.64	0.45	0.59	0.11
Zn	69	47	80	63	39	51	94	38	4	20
Zr	185.0	109.1	214.3	149.8	108.1	172.6	260.5	163.1	23.7	18.5

Table 2. Tectonites' Whole Rock Geochemical Data

Rock	TECT	TECT	TECT	TECT
SiO_2	43.12	77.12	68.23	66.06
Al_2O_3	21.83	13.24	18.2	15.44
Fe_2O_3	5.72	0.36	2.19	6.05
TiO_2	0.31	0.02	0.18	0.51
MgO	14.87	0.09	1.1	1.23
MnO	0.04	0.02	0.01	0.06
CaO	0.02	0.19	0.02	0.64
Na_2O	0.17	4.03	0.21	0.13
K_2O	9.95	3.91	6.16	5.31
P_2O_5	<0.01	0.06	0.02	0.12
Cr_2O_3	<0.002	<0.002	-	-
LOI %	3.6	0.9	3.5	4.1
TOT %	99.65	99.93	99.82	99.64
Ag	<0.1	<0.1	0.1	0.2
As	<0.5	<0.5	11.7	0.8
Au	<0.5	<0.5	<0.5	<0.5
Ba	355	44	735	729
Be	5	6	4	3
Bi	<0.1	0.8	<0.1	<0.1
Cd	<0.1	<0.1	<0.1	<0.1
Ce	12.8	8.2	35.5	79.2
Co	15.9	52.2	48	189.8
Cr	-	-	14	54.72
Cs	10.1	1.8	3.2	10.5
Cu	0.8	2.2	3.5	3.8
Dy	0.88	0.88	2.9	2.81
Er	0.70	0.60	1.44	1.88
Eu	0.04	0.09	1.04	0.8
Ga	36.9	25.3	29.2	22.6
Gd	0.84	0.71	3.77	3.72
Hf	6.5	1.4	4.4	4
Hg	<0.01	<0.01	<0.01	<0.01
Ho	0.23	0.16	0.47	0.63
La	4.6	3.3	33.7	25.4
Lu	0.16	0.12	0.21	0.24
Mo	<0.1	<0.1	<0.1	0.9
Nb	11.0	12.1	9.2	10.3
Nd	3.8	2.5	23.1	22.3
Ni	16.0	0.3	3	28.5
Pb	2.3	2.2	4.4	3.3
Pr	0.93	0.85	7.46	5.69
Rb	808.7	360.4	204	243.4
Sb	<0.1	<0.1	<0.1	<0.1
Sc	4	<1	15	13
Se	<0.5	<0.5	<0.5	<0.5
Sm	0.58	0.72	4.65	4.19
Sn	4	8	5	2
Sr	4.1	34.1	24.8	57.8
Ta	1.0	3.1	0.6	1.3
Tb	0.14	0.13	0.57	0.53
Th	49.0	5.8	8.4	12.2
Tl	2.8	0.1	0.1	0.8
Tm	0.11	0.10	0.21	0.25
U	8.5	2.2	2.4	3.6
V	23	<8	31	83
W	17.9	375.4	396.3	1356.1
Y	8.2	6.3	10.7	14.3
Yb	0.73	0.78	1.39	1.55
Zn	65	2	8	103
Zr	232.1	18.0	129	143

Table 3. Hydrothermalites' Whole Rock Geochemical Data

Rock	HDTM	HDTM	HDTM	HDTM	HDTM	HDTM	HDTM	HDTM	HDTM	HDTM	HDTM
SiO_2	77.48	73.67	69.04	75.77	86.26	66.16	63.95	66.19	65.9	63.19	69.55
Al_2O_3	12.87	11.89	14.37	6.04	1.12	14.85	11.86	15.74	15.82	14.4	14.85
Fe_2O_3	0.54	3.73	3.99	9.33	7.9	4.19	8.86	4.04	4.16	5.78	2.71
TiO_2	0.05	0.42	0.46	0.20	0.12	0.52	1.87	0.52	0.52	0.74	0.31
MgO	1.65	1.20	1.21	0.53	0.13	1.48	5.54	1.51	1.73	2.17	0.81
MnO	<0.01	0.05	0.06	0.02	<0.01	0.07	0.11	0.05	0.11	0.09	0.05
CaO	<0.01	2.00	2.45	0.83	0.01	3.48	1.54	3.03	3.28	4.64	2.42
Na_2O	0.11	0.63	0.97	0.37	0.01	3.87	0.06	4.48	0.8	3.05	4.15
K_2O	4.72	3.49	4.19	1.70	0.44	2.62	1.82	2.31	4.56	2.81	2.84
P_2O_5	0.02	0.16	0.18	0.08	0.01	0.17	0.19	0.19	0.18	0.24	0.11
Cr_2O_3	<0.002	<0.002	<0.002	<0.002	-	-	-	-	-	-	-
LOI %	2.4	2.6	2.8	4.9	3.9	2.2	4	1.6	2.7	2.6	1.9
TOT %	99.80	99.79	99.76	99.75	99.86	99.59	99.79	99.65	99.73	99.7	99.67
Ag	<0.1	0.2	1.4	4.4	0.6	<0.1	<0.1	0.1	0.2	0.1	0.1
As	<0.5	1.4	2.0	6.3	15.4	0.6	127	<0.5	1.7	<0.5	<0.5
Au	<0.5	360.8	5430.7	25052.6	25.3	<0.5	7.5	1.8	24.3	<0.5	<0.5
Ba	418	666	674	377	80	695	259	778	833	689	1143
Be	<1	1	<1	<1	<1	2	4	2	7	3	2
Bi	<0.1	0.3	1.2	2.0	1.7	<0.1	<0.1	<0.1	<0.1	<0.1	<0.1
Cd	<0.1	<0.1	0.8	0.2	<0.1	<0.1	<0.1	<0.1	<0.1	<0.1	<0.1
Ce	16.2	64.3	75.8	41.1	16.9	98.3	26.6	73.8	83.2	146.7	89.7
Co	99.3	54.1	61.7	113.2	175.8	86.2	35.9	75.4	62.5	48	66.7
Cr	-	-	-	-	<20	<20	61.56	<20	14	<20	<20
Cs	0.5	1.0	0.8	0.4	<0.1	1.9	2.9	1.4	1.3	2.7	0.5
Cu	0.4	19.7	51.3	704.7	14.8	3.4	2.6	10.7	18.4	6.9	3.3
Dy	2.99	1.86	2.38	0.58	2.37	2.5	5.32	2.48	2.67	4.5	1.95
Er	1.49	0.87	1.02	0.24	1.72	1.38	4.67	1.27	1.43	2.36	1.04
Eu	0.05	0.96	1.14	0.52	0.27	1.52	1.99	1.46	1.29	2.05	1.08
Ga	19.3	16.6	19.8	10.2	0.7	17.8	18.4	18	20.5	18.1	17.2
Gd	3.11	2.86	3.99	1.50	1.65	4.16	4.91	3.97	4.56	7.03	3.07
Hf	4.3	3.1	3.4	1.2	1.3	4.5	5.6	4.2	3.5	5.2	4.1
Hg	<0.01	<0.01	<0.01	<0.01	<0.01	<0.01	<0.01	<0.01	<0.01	<0.01	<0.01
Ho	0.52	0.33	0.38	0.10	0.57	0.51	1.46	0.47	0.54	0.83	0.39
La	7.3	30.1	36.0	19.6	8	48.5	10	34.5	39.6	71	44.2
Lu	0.19	0.13	0.14	0.04	0.25	0.22	0.86	0.21	0.19	0.34	0.15
Mo	0.3	0.8	1.4	5.5	3.6	0.6	1	0.3	0.5	<0.1	0.2
Nb	6.9	5.0	6.1	2.7	3.6	8.3	15	6.9	7.1	11.3	5.9
Nd	10.9	26.4	35.2	16.2	6.9	39.4	15.6	34.2	35.1	58.9	32.5
Ni	0.5	9.1	8.1	11.8	4.1	10.5	19.9	11.1	7.9	16.2	2.6
Pb	2.7	1.9	18.9	2.4	3.2	4	0.5	3.1	2.1	3.5	5.1
Pr	2.41	7.20	8.66	4.36	1.84	10.65	3.54	8.73	9.44	16.67	9.15
Rb	167.1	95.6	114.4	42.6	6.8	83.1	82.7	72.4	119.6	89.8	54.8
Sb	<0.1	<0.1	<0.1	<0.1	0.4	<0.1	<0.1	<0.1	<0.1	<0.1	<0.1
Sc	3	6	7	3	1	8	23	7	6	12	4
Se	<0.5	<0.5	<0.5	0.6	<0.5	<0.5	<0.5	<0.5	<0.5	<0.5	<0.5
Sm	3.19	4.12	5.41	2.39	1.58	6.2	4.06	4.93	5.86	9.89	4.44
Sn	1	<1	1	<1	<1	1	4	1	1	2	<1
Sr	5.3	201.2	191.0	100.4	8.7	618.7	11.8	698.5	136.4	624.4	594.1
Ta	0.6	0.5	0.6	0.4	0.5	1.2	1.2	0.8	0.8	0.9	0.5
Tb	0.47	0.36	0.42	0.15	0.34	0.55	0.87	0.49	0.54	0.83	0.38
Th	50.9	5.7	8.6	4.2	1.7	14.9	6.6	9.7	11.4	13.2	6.6
Tl	0.2	0.2	0.1	<0.1	<0.1	0.3	0.1	0.3	0.2	0.4	<0.1
Tm	0.20	0.13	0.14	0.03	0.26	0.21	0.75	0.21	0.22	0.35	0.17
U	9.0	1.0	2.7	0.6	0.5	3	2	3.6	3.3	2.7	0.9
V	<8	53	68	31	11	59	108	61	61	82	31
W	760.1	377.6	384.0	679.6	848.6	1293.3	182.4	789.4	617.8	294.3	561.1
Y	14.7	10.6	10.8	2.9	15.4	12.6	35.2	11.3	14.5	21.5	11.1
Yb	1.17	1.08	1.02	0.28	1.54	1.51	5.51	1.4	1.36	2.33	1.1
Zn	5	28	54	24	10	62	99	61	34	92	33
Zr	82.2	123.7	134.6	51.5	53	159.3	201.1	163.6	141.5	203.2	170.3

Table 4. Zircon U-Pb Geochronological Data for the Hydrothermally Altered Granitoid (HAG)

Sample	7/6 ratio	1s(%)	7/5 ratio	1s(%)	6/8 ratio	1s(%)	Rho	7/6 age	1s(Ma)	7/5 age	1s(Ma)	6/8 age	1s(Ma)
HAG	0.070721532	3.210970015	1.111222608	3.621749577	0.113958869	1.675333269	0.70	949.4	65.7	758.8	19.4	695.7	11.0
HAG	0.072337392	1.217359922	1.16628746	1.580915337	0.116934182	1.00862685	0.62	995.4	24.7	784.9	8.6	712.9	6.8
HAG	0.074653205	3.157141966	1.162927532	3.69562368	0.112980351	1.920960435	0.76	1059.2	63.5	783.3	20.2	690.0	12.6
HAG	0.12688133	6.946566067	7.323903983	7.372789618	0.418642818	2.470474979	0.33	2055.2	122.6	2151.7	65.9	2254.3	47.0
HAG	0.127141633	1.135703133	3.994593907	2.074394617	0.227868124	1.73588347	0.83	2058.8	20.0	1633.1	16.8	1323.3	20.8
HAG	0.130110871	4.379386506	3.982011796	5.350586422	0.221966627	3.074044385	0.81	2099.5	76.9	1630.5	43.4	1292.3	36.0
HAG	0.135838586	0.669915132	5.54444687	1.993673055	0.296028688	1.87775024	0.94	2174.8	11.7	1907.5	17.2	1671.6	27.6
HAG	0.136489504	0.504918489	4.86093188	2.105787142	0.258296788	2.044357309	0.97	2183.1	8.8	1795.5	17.7	1481.1	27.1
HAG	0.136736811	0.759661978	3.022738339	2.941161905	0.160329646	2.841363587	0.97	2186.3	13.2	1413.4	22.4	958.6	25.3
HAG	0.137664412	0.507358325	4.644377536	1.445170369	0.244683428	1.353183256	0.93	2198.0	8.8	1757.3	12.1	1411.0	17.1
HAG	0.140331744	0.524921237	6.026562394	1.535290764	0.311467301	1.442766587	0.94	2231.3	9.1	1979.7	13.4	1747.9	22.1
HAG	0.141544107	0.814664969	6.313458411	1.660479281	0.323499978	1.44689752	0.87	2246.2	14.1	2020.3	14.6	1806.8	22.8
HAG	0.141698397	0.590935967	5.942666435	1.808542624	0.304169134	1.709275023	0.94	2248.1	10.2	1967.5	15.7	1711.9	25.7
HAG	0.142521309	5.066020859	6.089400078	5.397899275	0.309879918	1.863531388	0.58	2258.1	87.4	1988.7	47.1	1740.1	28.4
HAG	0.143631923	0.578306199	6.209341621	2.165446362	0.313540253	2.086796561	0.96	2271.5	10.0	2005.8	18.9	1758.1	32.1
HAG	0.144348361	0.741288124	7.090997309	2.396211597	0.356282252	2.278666701	0.95	2280.0	12.8	2122.9	21.3	1964.5	38.6
HAG	0.145090459	1.177567646	6.563735815	2.746170098	0.328103577	2.480883844	0.90	2288.9	20.3	2054.5	24.2	1829.2	39.5
HAG	0.14858475	0.780193865	7.502674873	2.093165084	0.366218782	1.942327882	0.93	2329.7	13.4	2173.3	18.8	2011.6	33.6
HAG	0.152943318	1.012844027	8.221042251	3.392237748	0.38984781	3.237502728	0.98	2379.1	17.3	2255.7	30.7	2122.1	58.5
HAG	0.15364656	0.572835448	7.996341765	1.971430605	0.377456782	1.886371697	0.96	2386.9	9.8	2230.6	17.8	2064.4	33.3
HAG	0.153975741	0.503978683	2.707865772	5.103874583	0.127547971	5.078931112	1.00	2390.6	8.6	1330.6	37.8	773.9	37.0
HAG	0.153996508	1.267988629	8.097218133	3.759263464	0.381349948	3.538964061	0.94	2390.8	21.6	2241.9	34.0	2082.6	63.0
HAG	0.154482766	0.767978497	6.533867234	1.97661232	0.306753123	1.821319657	0.92	2396.1	13.1	2050.5	17.4	1724.7	27.6
HAG	0.155808307	2.763035025	6.230973098	4.182381568	0.290044072	3.139737734	0.75	2410.7	46.9	2008.8	36.6	1641.7	45.5
HAG	0.159251935	8.195199148	6.771075636	8.437420403	0.308369681	2.007180606	0.43	2447.7	138.7	2082.0	74.6	1732.7	30.5
HAG	0.160242768	0.726150363	5.681863038	2.886233971	0.257164518	2.793394384	0.97	2458.2	12.3	1928.6	24.9	1475.3	36.8
HAG	0.167343016	2.110160343	4.190319867	7.446727982	0.181609394	7.141497109	0.96	2531.2	35.4	1672.1	61.0	1075.8	70.8
HAG	0.167969659	5.731741006	3.737289747	6.240785963	0.161370689	2.468715147	0.65	2537.5	96.1	1579.4	50.0	964.4	22.1
HAG	0.17042861	2.140451908	6.942055427	3.004219755	0.295422997	2.108032725	0.70	2561.9	35.8	2104.0	26.7	1668.6	31.0
HAG	0.172799565	1.730649913	5.709585018	2.996799167	0.239640725	2.446560059	0.81	2584.9	28.9	1932.8	25.9	1384.8	30.5
HAG	0.237198246	3.820051832	2.781491819	4.308832037	0.085048183	1.993298151	0.71	3101.3	60.9	1350.6	32.2	526.2	10.1
HAG	0.261374517	2.562455129	8.862904012	4.806729637	0.24593001	4.066752207	0.85	3255.0	40.3	2324.0	43.9	1417.5	51.7

Table 5. Zircon U-Pb Geochronological Data for the Príncipe Granite's Fine Grained Facies (FGPG)

Sample	7/6 ratio	1s(%)	7/5 ratio	1s(%)	6/8 ratio	1s(%)	Rho	7/6 age	1s(Ma)	7/5 age	1s(Ma)	6/8 age	1s(Ma)
FGPG	0.067796809	0.776949855	1.071026794	1.131142599	0.114574985	0.822090325	0.70	862.3	16.1	739.2	5.9	699.3	5.4
FGPG	0.079022408	0.812026629	1.913641241	1.752808551	0.175634161	1.553367493	0.88	1172.7	16.1	1085.9	11.7	1043.1	15.0
FGPG	0.092552283	5.812024038	1.530427024	5.938620751	0.119929	1.219669219	0.37	1478.7	110.2	942.7	36.5	730.2	8.4
FGPG	0.101121273	36.40095928	4.311674748	40.35691293	0.309244645	17.42557271	0.69	1644.8	675.3	1695.6	332.6	1737.0	265.3
FGPG	0.120653368	6.409698058	4.98431481	6.589413581	0.299615819	1.528444358	0.23	1965.9	114.3	1816.7	55.7	1689.4	22.7
FGPG	0.126168383	0.416135366	5.222845082	1.796912538	0.300230861	1.748063508	0.97	2045.3	7.4	1856.4	15.3	1692.5	26.0
FGPG	0.127659811	0.861161076	3.739645742	2.901851131	0.212458931	2.771126412	0.95	2066.0	15.2	1579.9	23.2	1241.9	31.3
FGPG	0.128591648	1.965949473	4.890929721	3.646249828	0.275852793	3.070859892	0.95	2078.8	34.6	1800.7	30.7	1570.4	42.8
FGPG	0.129860053	0.522900573	6.758300169	1.769393181	0.377451039	1.690363044	0.95	2096.1	9.2	2080.3	15.7	2064.4	29.9
FGPG	0.130120138	0.821870008	6.433277211	2.007837346	0.358580341	1.831922623	0.91	2099.6	14.4	2036.8	17.6	1975.4	31.2
FGPG	0.132539054	1.065817437	6.932034305	1.533765983	0.379328576	1.102937569	0.87	2131.9	18.7	2102.8	13.6	2073.1	19.6
FGPG	0.133156776	1.216710703	7.181235556	1.705683695	0.391142157	1.195396141	0.69	2140.0	21.3	2134.2	15.2	2128.1	21.7
FGPG	0.133926423	0.780234201	4.711903285	2.393358113	0.255169537	2.262608593	0.94	2150.1	13.6	1769.4	20.0	1465.1	29.7
FGPG	0.133968862	1.414905785	4.975736241	2.802225244	0.269371849	2.418782325	0.95	2150.6	24.7	1815.2	23.7	1537.6	33.1
FGPG	0.134699136	0.629268868	7.370704174	1.920305297	0.396865087	1.814274821	0.94	2160.1	11.0	2157.4	17.2	2154.6	33.2
FGPG	0.135179054	0.447595152	7.291934886	1.602813736	0.391229958	1.539048554	0.96	2166.3	7.8	2147.8	14.3	2128.5	27.9
FGPG	0.136712431	0.472047436	8.137445302	1.844933454	0.431696772	1.783521984	0.97	2186.0	8.2	2246.4	16.7	2313.4	34.7
FGPG	0.136889787	0.475751788	7.362015189	1.203494505	0.390053687	1.105467892	0.91	2188.2	8.3	2156.4	10.8	2123.1	20.0
FGPG	0.138055914	0.570312627	6.082849972	1.959249215	0.319558824	1.874406837	0.96	2203.0	9.9	1987.8	17.1	1787.6	29.3
FGPG	0.140810798	0.434232106	7.196492699	1.634113074	0.370666772	1.575362821	0.96	2237.2	7.5	2136.1	14.6	2032.5	27.5
FGPG	0.144739973	0.561083001	6.255787127	1.891387245	0.313467269	1.806247928	0.95	2284.7	9.7	2012.3	16.6	1757.7	27.8
FGPG	0.145892917	6.229026534	4.419971343	6.656910782	0.219727276	2.348124698	0.35	2298.3	107.0	1716.1	55.1	1280.4	27.3
FGPG	0.14684925	1.170056322	4.596146652	1.82227509	0.226997393	1.397016358	0.76	2309.6	20.1	1748.6	15.2	1318.7	16.7
FGPG	0.152452601	5.853538528	8.224540715	6.08013493	0.391269092	1.644423142	0.27	2373.6	99.8	2256.0	55.0	2128.7	29.8
FGPG	0.154204022	4.066124805	2.529675933	13.58679029	0.118978342	12.96408498	0.95	2393.1	69.2	1280.6	98.9	724.7	88.9
FGPG	0.156006828	1.979982078	5.792152917	2.851068045	0.269274444	2.051404389	0.88	2412.8	33.6	1945.2	24.7	1537.1	28.1
FGPG	0.167466019	1.117762622	7.19893334	4.61844021	0.311774205	4.481137879	0.97	2532.5	18.8	2136.4	41.2	1749.4	68.7
FGPG	0.168581344	1.103071422	3.56953834	6.516865276	0.15356819	6.422831654	1.00	2543.6	18.5	1542.8	51.7	920.9	55.1
FGPG	0.182103639	2.651088513	11.02914612	3.099043181	0.439260339	1.604929386	0.51	2672.1	43.9	2525.6	28.9	2347.3	31.6
FGPG	0.189213057	6.771261581	9.701980328	7.67437719	0.371884444	3.611936027	0.73	2735.3	111.4	2406.9	70.6	2038.3	63.1
FGPG	0.191376508	2.221520601	5.773213868	3.540176	0.21879014	2.756391179	0.78	2754.0	36.5	1942.4	30.6	1275.5	31.9
FGPG	0.192376783	7.045506127	3.817566892	8.030647199	0.143923835	3.853847149	0.48	2762.6	115.7	1596.5	64.6	866.8	31.3

Table 6. Zircon U-Pb Geochronological Data for the Príncipe Granite's Medium Porphyritic Facies (MPPG-a)

Sample	7/6 ratio	1s(%)	7/5 ratio	1s(%)	6/8 ratio	1s(%)	Rho	7/6 age	1s(Ma)	7/5 age	1s(Ma)	6/8 age	1s(Ma)
MPPG-a	0.090768314	1.981137253	1.521707372	2.235606405	0.121589369	1.035872185	0.45	1441.7	37.8	939.2	13.7	739.7	7.2
MPPG-a	0.13063375	0.398218051	6.800999969	1.168263151	0.377586191	1.098299219	0.94	2106.5	7.0	2085.9	10.3	2065.0	19.4
MPPG-a	0.131461213	1.718611873	3.903720262	7.002386974	0.215367308	6.788210115	0.97	2117.6	30.1	1614.5	56.6	1257.3	77.5
MPPG-a	0.132599611	0.441824627	7.870218199	1.050126043	0.430470354	0.952657182	0.90	2132.7	7.7	2216.3	9.5	2307.8	18.5
MPPG-a	0.135926436	0.630821994	6.305631182	2.309102709	0.336452191	2.221265165	0.96	2175.9	11.0	2019.2	20.2	1869.6	36.0
MPPG-a	0.136449627	0.835640741	3.145376069	2.943521609	0.167185632	2.822414571	0.99	2182.6	14.5	1443.9	22.7	996.6	26.1
MPPG-a	0.142479391	0.504471682	8.076331521	1.447674431	0.411112625	1.356933889	0.93	2257.6	8.7	2239.6	13.1	2220.0	25.5
MPPG-a	0.143976204	0.764151355	7.968299687	1.207985649	0.401396578	0.935575778	0.87	2275.6	13.2	2227.4	10.9	2175.5	17.3
MPPG-a	0.146011728	0.514889582	5.743987301	2.073008297	0.285314901	2.008046842	0.97	2299.7	8.8	1938.0	17.9	1618.1	28.7
MPPG-a	0.146677067	0.749282409	7.305141594	1.811740064	0.361214475	1.649538702	0.96	2307.5	12.9	2149.4	16.2	1987.9	28.2
MPPG-a	0.147761625	0.44409157	7.385481693	1.637565801	0.362506578	1.576199362	0.96	2320.2	7.6	2159.2	14.6	1994.0	27.0
MPPG-a	0.148429718	0.367360667	8.68691742	1.988332135	0.424466633	1.954101026	0.98	2327.9	6.3	2305.7	18.1	2280.7	37.5
MPPG-a	0.148505348	0.414563401	7.540282772	1.276427153	0.36825128	1.207229664	0.94	2328.8	7.1	2177.8	11.4	2021.2	20.9
MPPG-a	0.149352823	0.357847834	9.414513494	1.604313458	0.457175734	1.56389469	0.97	2338.5	6.1	2379.2	14.7	2427.1	31.6
MPPG-a	0.149904969	0.397675785	9.398379607	1.113173882	0.454711227	1.039716337	0.93	2344.8	6.8	2377.7	10.2	2416.2	21.0
MPPG-a	0.149943938	0.660349603	7.701042056	2.099922378	0.372494023	1.993392183	0.98	2345.3	11.3	2196.7	18.9	2041.1	34.9
MPPG-a	0.150246698	0.432749082	7.602536143	1.375772997	0.366988354	1.305940111	0.95	2348.7	7.4	2185.2	12.3	2015.2	22.6
MPPG-a	0.151250806	0.627852425	8.600516926	2.423796758	0.412406576	2.341066436	0.97	2360.1	10.7	2296.6	22.0	2225.9	44.1
MPPG-a	0.153908054	0.741530528	7.590993119	1.472096602	0.357714033	1.271692133	0.94	2389.8	12.6	2183.8	13.2	1971.3	21.6
MPPG-a	0.159498022	0.492340472	7.802621002	2.211167306	0.354800265	2.15565807	0.97	2450.3	8.3	2208.5	19.9	1957.5	36.4

Table 7. Zircon U-Pb Geochronological Data for the Príncipe Granite's Medium Porphyritic Facies (MPPG-b)

Sample	7/6 ratio	1s(%)	7/5 ratio	1s(%)	6/8 ratio	1s(%)	Rho	7/6 age	1s(Ma)	7/5 age	1s(Ma)	6/8 age	1s(Ma)
MPPG-b	0.111638755	0.698845868	2.282683097	1.93315864	0.167474976	1.834786601	0.96	1602.6	10.2	1206.9	13.6	998.2	17.1
MPPG-b	0.123417048	0.491187902	2.851478786	1.374427663	0.204902331	0.893096747	0.80	1641.3	19.2	1369.2	10.3	1201.6	9.9
MPPG-b	0.109851554	0.510174046	3.482653196	2.902512104	0.244114037	2.689636782	0.93	1687.3	19.3	1523.3	22.6	1408.0	34.1
MPPG-b	0.109053603	0.580261104	3.323054877	1.175565041	0.224551249	0.871918802	0.87	1754.6	14.2	1486.5	9.1	1305.9	10.4
MPPG-b	0.11781744	0.382497041	3.756715296	0.853995485	0.250732449	0.740825256	0.85	1777.2	7.6	1583.5	6.8	1442.3	9.6
MPPG-b	0.103470417	1.054406471	4.061225667	1.204086445	0.270094555	1.0550456	0.87	1783.7	10.6	1646.6	9.8	1541.3	14.5
MPPG-b	0.100930395	1.038922326	4.218476264	1.006797238	0.278514705	0.867964932	0.85	1796.9	9.3	1677.6	8.3	1583.9	12.2
MPPG-b	0.125154329	0.808987345	3.908658744	1.157111229	0.253928528	0.917077222	0.78	1826.3	12.6	1615.5	9.3	1458.7	12.0
MPPG-b	0.112879966	1.205982337	5.386920107	1.997349216	0.346116568	1.586935425	0.92	1846.3	21.7	1882.8	17.0	1916.0	26.3
MPPG-b	0.116874077	0.497732938	4.082512356	1.314699071	0.259708187	1.242516009	0.94	1864.3	7.8	1650.8	10.7	1488.3	16.5
MPPG-b	0.114009382	0.429636608	4.090781897	2.974872025	0.253855662	2.913850438	0.99	1909.0	8.9	1652.5	24.0	1458.3	38.2
MPPG-b	0.12373534	0.554845139	5.320637287	1.189700038	0.32910948	0.951664303	0.89	1914.8	12.8	1872.2	10.2	1834.1	15.2
MPPG-b	0.09885404	0.549329021	4.700362415	0.830485964	0.289348001	0.7371587	0.87	1923.4	6.9	1767.3	7.0	1638.3	10.7
MPPG-b	0.107329909	0.779359611	4.93124225	1.301379725	0.293369897	1.233644945	0.95	1984.4	7.4	1807.6	11.0	1658.3	18.0
MPPG-b	0.108666697	0.419115072	4.97105967	1.314875116	0.292127571	1.219684802	0.92	2006.2	8.7	1814.4	11.1	1652.2	17.8
MPPG-b	0.121910052	0.414378254	6.61292964	0.916714235	0.38761348	0.729734102	0.83	2010.8	9.8	2061.1	8.1	2111.8	13.1
MPPG-b	0.117252466	0.713947642	6.10636042	1.854940203	0.353863104	1.669234146	0.90	2031.0	14.3	1991.2	16.2	1953.0	28.1
MPPG-b	0.136655169	0.513014579	4.671728753	1.407104778	0.247942104	1.304869041	0.93	2185.2	8.9	1762.2	11.7	1427.9	16.8
MPPG-b	0.141014295	1.312499222	6.586313674	1.664061124	0.338748979	1.022959049	0.78	2239.7	22.7	2057.5	14.7	1880.6	16.7

Table 8. Sm-Nd Geochronological Data for the Príncipe Granite's (PG), Tectonites' (TECT) and Hydrothermalites' (HDTM) Samples

Sample	PG	PG	PG	PG	PG	TECT	TECT	HDTM	HDTM
Sm (ppm)	5.383	7.311	14.33	7.484	8.602	0.787	0.868	2.389	5.935
Nd (ppm)	28.337	35.223	97.146	47.352	59.812	3.987	3.259	15.593	35.933
$(^{143}Nd/^{144}Nd)_i$	0.509741	0.51	0.509846	0.509760	0.509849	0.510887	0.511385	0.51076	0.510872
$(^{143}Nd/^{144}Nd)_{iDM}$	0.509517	0.509431	0.509776	0.509616	0.509783	0.509178	0.508823	0.509624	0.509659
$(^{147}Sm/^{144}Nd)_o$	0.511377	0.511513	0.511117	0.511121	0.511087	0.511293	0.511933	0.51108	0.511212
$^{147}Sm/^{144}Nd$	0.1148	0.1255	0.0892	0.0955	0.0869	0.1193	0.1609	0.0926	0.0998
T_{DM} (Ga)	2.457719396	2.515986522	2.282218042	2.390232413	2.277103786	2.687445141	2.927299263	2.384777128	2.361584309
T (Ga)	2.16	2.16	2.16	2.16	2.16	0.52	0.52	0.52	0.52
ε_{Nd} **(0)**	-24.60	-21.95	-29.67	-29.59	-30.26	-26.24	-13.75	-30.39	-27.82
ε_{Nd} **(T)**	-1.85	-2.17	0.21	-1.48	0.26	-21.12	-11.39	-23.50	-21.41
I(T)	0.50984	0.50984	0.50984	0.50984	0.50984	0.51197	0.51197	0.51197	0.51197
ε_{Nd} (T_{DM})	2.64	2.53	2.96	2.76	2.96	2.24	1.86	2.77	2.81

Table 9. Sulphur Stable Isotopes Data for pyrite grains from the Príncipe and Chapada de Natividade Gold Deposits

Sample	Standard	$\delta^{34}S$ (‰)	2σ SD (‰)
PRÍNCIPE-I	IAEA-S1	2.76	0.16
PRÍNCIPE-I	IAEA-S1	2.40	0.19
PRÍNCIPE-II	IAEA-S1	0.32	0.19
PRÍNCIPE-II	IAEA-S1	0.33	0.14
PRÍNCIPE-III	IAEA-S1	0.63	0.18
PRÍNCIPE-III	IAEA-S1	1.04	0.15
PRÍNCIPE-IV	IAEA-S1	0.92	0.29
PRÍNCIPE-IV	IAEA-S1	1.11	0.18
PRÍNCIPE-IV	IAEA-S1	-1.12	0.16
PRÍNCIPE-IV	IAEA-S1	0.83	0.20
CHAPADA	IAEA-S1	-0.01	0.16
CHAPADA	IAEA-S1	0.06	0.15

Table 10. Carbon and Oxygen Stable Isotopes Data for Parallel and Perpendicular Carbonate Veins

Standard		**V-PDB**	**V-PDB**	**V-SMOW**
Isotope		**$\delta^{13}C$ ‰**	**$\delta^{18}O$ ‰**	**$\delta^{18}O$ ‰**
Sample	Parallel	-6.55	-16.49	13.86
	Perpendicular	-6.14	-13.22	17.23

Table 11. Microprobe Data for the Príncipe Granite's Feldspars

Rock	**PG**	**PG**	**PG**	**PG**	**PG**	**PG**	**PG**	**PG**	**PG**	**PG**	**PG**	**PG**	**PG**	**PG**	**PG**	**PG**	**PG**	**PG**
Mineral	**KFS**	**KFS**	**KFS**	**KFS**	**KFS**	**KFS**	**KFS**	**KFS**	**KFS**	**KFS**	**KFS**	**PL**	**PL**	**PL**	**PL**	**PL**	**PL**	**PL**
SiO_2	62.168	62.671	62.752	62.948	62.98	62.946	62.524	63.067	62.704	63.01	62.772	65.887	66.052	65.935	66.889	66.239	66.817	66.766
Al_2O_3	18.448	18.766	18.672	19.141	18.946	18.594	18.68	18.9	18.809	19.062	18.582	20.024	20.148	20.541	20.008	20.208	20.259	20.292
TiO_2	0	0	0	0	0	0.013	0	0	0	0	0	0	0	0	0	0	0	0
K_2O	15.57	15.41	15.948	15.522	15.402	16.01	15.931	15.753	16.327	15.775	16.343	0.101	0.099	0.115	0.108	0.101	0.103	0.125
Na2O	0.754	0.904	0.738	0.734	0.821	0.729	0.773	0.617	0.509	0.785	0.38	11.69	12.06	11.735	11.6	11.911	11.804	11.945
FeO	0.046	0	0	0.05	0	0.009	0	0	0.012	0.028	0.009	0.013	0	0.02	0	0.031	0.022	0.053
MgO	0	0.001	0	0	0	0	0.005	0	0	0.025	0	0	0.002	0	0	0	0	0.01
CaO	0.002	0	0.008	0.026	0	0.014	0.026	0	0.003	0	0.004	0.427	0.432	0.526	0.294	0.495	0.388	0.567
MnO	0.047	0.034	0.045	0	0	0	0	0	0	0.011	0.007	0	0	0.029	0	0	0	0
SrO	0	0.131	0	0.026	0.054	0.028	0.116	0.044	0.035	0	0.058	0	0.055	0.054	0.059	0.066	0	0.076
BaO	0.045	0.155	0.243	0.145	0.167	0.288	0.354	0.355	0.233	0.499	0.156	0	0	0	0	0	0	0
Cr_2O_3	0	0.007	0	0.023	0	0.007	0	0.029	0.027	0.008	0	0.01	0.039	0	0	0.015	0	0.005
V_2O_3	0.039	0	0	0.004	0	0	0	0	0.002	0.02	0	0	0.018	0	0.037	0.067	0.041	0.044
F	0	0	0	0	0	0	0	0	0	0	0	0	0	0	0	0	0	0
Cl	0	0.01	0	0.022	0.014	0.008	0.007	0.024	0.019	0.009	0	0.004	0.01	0.009	0.01	0.005	0.01	0.002
Total	97.119	98.087	98.406	98.636	98.381	98.644	98.414	98.784	98.676	99.23	98.311	98.155	98.913	98.962	99.003	99.137	99.442	99.885

Table 12. Microprobe Data for the Príncipe Granite's Muscovite and Biotite Grains

Rock	PG	PG	PG	PG	PG	PG	PG	PG	PG	PG	PG	PG	PG	PG	PG	PG	PG	PG	PG
Mineral	MS	MS	MS	MS	MS	MS	MS	MS	MS	MS	BT	BT	BT	BT	BT	BT	BT	BT	BT	BT
SiO_2	45.52	46.99	47.03	45.52	45.30	45.13	44.83	44.41	45.45	45.45	35.54	35.22	34.54	35.13	47.03	34.96	35.42	34.94	34.74	34.98
Al_2O_3	30.45	29.83	28.06	30.26	31.69	30.79	31.45	31.95	33.43	32.26	18.13	17.87	16.87	17.39	29.55	16.91	18.45	16.97	16.80	16.79
TiO_2	0.834	0.116	0.138	0.578	0.921	0.751	0.768	0.869	1.053	1.051	0.814	0.771	1.726	1.577	0.226	1.573	1.437	1.483	1.587	1.511
K_2O	11.07	10.87	11.18	10.97	11.09	11.16	11.03	10.67	10.59	10.81	9.50	8.92	9.50	9.54	11.02	9.69	8.86	9.52	9.77	9.61
Na2O	0.208	0.164	0.146	0.257	0.329	0.23	0.21	0.322	0.669	0.418	0.106	0.14	0.091	0.081	0.242	0.106	0.09	0.052	0.092	0.033
FeO	4.06	4.20	3.98	4.21	4.41	4.68	4.37	3.75	2.59	3.48	25.71	24.49	25.91	26.56	4.28	26.75	25.05	26.68	25.98	25.82
MgO	1.395	1.646	1.802	1.403	1.127	1.277	1.206	0.973	0.936	0.849	4.142	3.974	5.004	5.434	1.583	5.237	4.744	4.901	4.964	5.087
CaO	0.002	0.014	0.03	0.041	0	0.029	0	0	0	0	0.079	0.056	0.018	0.019	0	0.049	0.043	0	0.036	0.009
MnO	0.049	0.046	0.122	0.078	0.105	0.031	0	0	0	0.034	0.602	0.591	0.377	0.408	0.046	0.387	0.474	0.436	0.43	0.372
SrO	0.07	0.083	0	0	0	0	0.104	0.022	0.061	0	0	0.063	0.077	0.001	0.088	0.039	0	0.036	0.06	0
BaO	0.108	0.24	0.011	0.055	0.034	0.065	0.132	0.044	0.11	0.012	0.168	0.083	0.106	0.084	0.012	0	0.085	0	0	0.095
Cr_2O_3	0	0.016	0.024	0.008	0	0.007	0	0	0.052	0.011	0	0.006	0.023	0	0	0.005	0.012	0.054	0.031	0
V_2O_3	0.045	0.004	0.022	0.072	0.029	0.045	0.021	0.002	0	0	0.01	0	0.014	0.019	0	0.049	0.016	0	0.02	0.032
F	0.731	0.861	0.783	0.712	0.369	0.454	0.472	0.348	0.265	0.474	0.874	0.911	1.197	1.208	0.629	1.299	0.975	1.186	1.165	1.295
Cl	0.005	0	0.004	0.009	0.016	0.003	0	0.039	0.002	0	0.08	0.081	0.047	0.037	0.006	0.031	0.046	0.053	0.066	0.048
Total	94.25	94.72	93.00	93.88	95.26	94.46	94.39	93.24	95.09	94.66	95.36	92.78	94.98	96.97	94.45	96.53	95.28	95.80	95.23	95.12

Table 13. Microprobe Data for the Príncipe Granite's Garnet Grains and Hydrothermalites' Carbonate Crystals

Rock	**PG**	**PG**	**PG**	**PG**	**PG**	**PG**	**PG**	**PG**	**PG**	**PG**	**PG**	**HDTM**	**HDTM**	**HDTM**	**HDTM**
Mineral	**GRT**	**GRT**	**GRT**	**GRT**	**GRT**	**GRT**	**GRT**	**GRT**	**GRT**	**GRT**	**GRT**	**CB**	**CB**	**CB**	**CB**
SiO_2	37.007	95.194	36.713	36.964	36.855	63.247	37.244	37.331	36.95	36.753	37.711	0.105	0.048	0.207	0.05
Al_2O_3	21.79	0.035	21.199	21.661	21.525	18.614	21.446	21.849	21.35	21.497	21.996	0	0	0.023	0.009
TiO_2	0.018	0	0.025	0.012	0	0	0.071	0	0.032	0.086	0.064	0	0.014	0	0.001
K_2O	0.007	0.006	0.028	0.041	0.017	16.504	0.022	0	0	0	0.023	0	0	0	0.015
Na2O	0	0	0.002	0.035	0	0.278	0.009	0	0.012	0.015	0.001	0	0.014	0.001	0.025
FeO	17.308	0.194	16.464	20.848	20.776	0.129	15.104	17.841	17.347	14.643	16.346	0.815	0	1.447	0.111
MgO	0.105	0.003	0.097	0.235	0.188	0	0.048	0.156	0.17	0.043	0.127	0.15	0.304	0.132	0.099
CaO	18.23	0.049	18.749	14.242	14.662	0.042	19.346	17.778	18.118	19.853	18.735	56.886	56.473	57.183	57.381
MnO	5.934	0.095	5.766	6.3	6.223	0.04	6.629	6.265	6.17	6.577	6.441	0.645	0.707	0.224	0.972
SrO	0	0.088	0.063	0	0.02	0.099	0	0.121	0.147	0.076	0.02	0.068	0.007	0.087	0
BaO	0.108	0.022	0.032	0.053	0.034	0.2	0	0	0	0	0.108	0.012	0.001	0	0.223
Cr_2O_3	0	0.016	0.011	0.013	0.001	0.001	0	0	0	0.058	0	0	0.047	0.024	0
V_2O_3	0.005	0.005	0.033	0	0	0	0	0.019	0.011	0.043	0	0	0.07	0	0.04
F	0.07	0	0.338	0.019	0.075	0	0.224	0.001	0.284	0.347	0.188	0	0	0	0
Cl	0	0.01	0.009	0.008	0	0.005	0	0	0.008	0.023	0.002	0.01	0	0.003	0.017
Total	100.553	95.715	99.385	100.421	100.344	99.158	100.049	101.361	100.477	99.863	101.683	58.689	57.685	59.33	58.939

Table 14. Microprobe Data for the Hydrothermalites' Feldspars and Micas

Rock	HTM	HTM	HTM	HTM	HTM	HTM	HTM	HTM	HTM	HTM	HTM	HTM	HTM	HTM	HTM	HTM	HTM	HTM	HTM	HTM
Min.	KF	KF	KF	PL	PL	PL	PL	PL	PL	PL	PL	MS	MS	MS	MS	MS	MS	BT	BT	BT	BT
SiO_2	66.65	67.30	66.91	66.12	66.51	66.50	66.90	66.46	67.01	66.79	96.59	46.76	46.50	46.16	46.56	46.55	46.85	37.70	35.92	36.20	36.55
Al_2O_3	19.88	19.91	20.13	20.00	20.02	20.12	19.92	20.04	19.80	20.11	0.01	32.08	32.86	32.53	32.63	32.57	31.84	25.77	16.99	16.45	17.17
TiO_2	0	0	0	0	0	0	0	0	0	0.012	0	0.999	0.623	0.54	0.537	0.503	0.723	0.823	2.244	1.669	1.958
K_2O	0.11	0.09	0.09	0.10	0.11	0.09	0.10	0.13	0.09	0.11	0.02	11.21	11.03	11.16	10.69	10.90	10.87	5.47	9.76	9.79	9.48
Na2O	11.95	11.99	12.01	11.90	12.12	11.74	12.05	11.86	11.89	11.99	0.03	0.38	0.36	0.41	0.48	0.44	0.42	0.12	0.09	0.15	0.13
FeO	0	0	0.003	0.022	0.033	0	0.021	0	0.004	0.02	0	2.952	3.54	3.241	3.079	3.223	3.19	12.115	18.469	18.504	17.829
MgO	0	0	0	0	0	0	0	0	0.023	0	0	2.156	1.696	2.007	2.063	2.07	2.175	7.799	11.31	11.8	11.454
CaO	0.16	0.122	0.137	0.35	0.313	0.245	0.273	0.173	0.266	0.234	0.036	0.027	0.011	0.013	0	0	0.021	0.043	0.004	0.057	0.018
MnO	0	0	0.043	0.003	0.05	0	0	0	0.051	0	0	0.036	0	0.028	0.044	0	0.002	0.163	0.15	0.118	0.11
SrO	0.032	0	0.07	0.021	0	0.071	0.176	0	0.026	0.136	0.05	0.053	0	0	0	0.158	0.02	0.062	0	0.109	0.005
BaO	0	0.109	0	0	0	0.132	0.032	0.143	0.055	0.066	0	0.157	0	0.189	0.089	0.045	0.068	0.459	0.361	0.19	0.361
Cr_2O_3	0	0	0	0	0.004	0.041	0	0	0.005	0	0.013	0	0	0	0	0	0.009	0.031	0.039	0.007	0.026
V_2O_3	0	0	0	0.05	0.058	0.005	0.026	0	0	0.016	0.011	0.067	0.061	0.029	0.085	0.067	0.023	0.044	0.018	0.123	0.109
F	0	0	0	0	0	0	0	0	0	0	0	0	0	0	0	0	0	0.016	0.236	0.363	0.263
Cl	0.001	0.02	0.014	0.012	0.025	0.016	0	0	0	0.008	0	0.001	0.003	0	0.032	0.043	0.006	0.087	0.01	0.039	0.028
Total	98.78	99.53	99.40	98.58	99.24	98.96	99.50	98.82	99.22	99.49	96.76	96.88	96.69	96.29	96.28	96.57	96.21	90.67	95.50	95.40	95.38

Table 15. Microprobe Data for the Hydrothermalites' Chlorites

Rock	HTM	HTM	HTM	HTM	HTM	HTM	HTM	HTM	HTM	HTM	HTM	HTM	HTM	HTM	HTM	HTM	HTM	HTM	HTM	HTM
Mineral	CHL	CHL	CHL	CHL	CHL	CHL	CHL	CHL	CHL	CHL	CHL	CHL	CHL	CHL	CHL	CHL	CHL	CHL	CHL	CHL
SiO_2	25.35	25.39	25.48	24.87	25.60	27.36	25.25	26.01	25.85	26.45	25.01	25.66	27.26	25.68	27.88	27.65	27.37	27.54	27.20	27.16	27.02
Al_2O_3	21.72	21.53	21.34	21.64	21.15	22.85	21.28	21.38	21.53	21.40	21.44	22.18	21.14	21.51	22.31	22.35	23.13	22.12	22.50	22.02	22.63
TiO_2	0.05	0.00	0.03	0.09	0.09	0.09	0.04	0.02	0.04	0.03	0.03	0.06	0.09	0.03	0.01	0.03	0.00	0.03	0.04	0.05	0.03
K_2O	0.07	0.04	0.12	0.06	0.03	1.74	0.12	0.11	0.12	0.12	0.08	0.11	1.31	0.11	0.01	0.03	0.04	0.07	0.07	0.13	0.04
Na2O	0.06	0.07	0.07	0.01	0.05	0.23	0.04	0.10	0.03	0.01	0.09	0.05	0.04	0.09	0.00	0.03	0.06	0.02	0.04	0.05	0.03
FeO	21.57	22.29	21.84	22.05	21.94	18.69	22.11	22.88	22.53	21.56	22.37	22.54	22.08	21.69	16.25	16.24	16.21	16.15	16.91	16.54	16.52
MgO	17.29	17.10	16.51	16.75	17.24	15.10	17.17	16.03	17.08	16.67	17.02	17.10	16.78	17.83	23.28	23.50	22.94	23.14	22.96	22.81	22.95
CaO	0.02	0.01	0.00	0.04	0.00	0.03	0.07	0.00	0.05	0.03	0.01	0.01	0.01	0.00	0.01	0.00	0.04	0.01	0.00	0.00	0.04
MnO	0.21	0.18	0.26	0.27	0.20	0.25	0.29	0.33	0.23	0.20	0.26	0.22	0.23	0.17	0.31	0.25	0.21	0.27	0.31	0.30	0.27
SrO	0.00	0.00	0.05	0.02	0.00	0.08	0.00	0.00	0.12	0.00	0.04	0.13	0.00	0.00	0.00	0.00	0.00	0.00	0.00	0.14	0.00
BaO	0.10	0.13	0.00	0.00	0.00	0.20	0.00	0.08	0.02	0.02	0.00	0.00	0.08	0.00	0.00	0.00	0.06	0.00	0.11	0.00	0.11
Cr_2O_3	0.00	0.00	0.00	0.00	0.03	0.00	0.02	0.00	0.00	0.04	0.01	0.00	0.00	0.03	0.03	0.00	0.00	0.01	0.01	0.00	0.00
V_2O_3	0.02	0.06	0.00	0.00	0.03	0.01	0.03	0.06	0.06	0.05	0.02	0.05	0.03	0.00	0.04	0.03	0.05	0.04	0.05	0.03	0.04
F	0.00	0.08	0.00	0.03	0.00	0.00	0.05	0.00	0.08	0.05	0.07	0.04	0.00	0.00	0.00	0.02	0.00	0.05	0.00	0.04	0.01
Cl	0.02	0.01	0.07	0.00	0.01	0.04	0.03	0.04	0.03	0.03	0.02	0.05	0.07	0.03	0.01	0.01	0.01	0.02	0.02	0.01	0.02
Total	86.47	86.85	85.75	85.81	86.38	86.64	86.47	87.03	87.73	86.62	86.43	88.16	89.12	87.16	90.14	90.11	90.12	89.44	90.21	89.23	89.69

Rock	HTM	HTM	HTM	HTM	HTM	HTM	HTM	HTM	HTM	HTM	HTM	HTM	HTM	HTM	HTM	HTM	HTM	HTM	HTM	HTM
Mineral	CHL	CHL	CHL	CHL	CHL	CHL	CHL	CHL	CHL	CHL	CHL	CHL	CHL	CHL	CHL	CHL	CHL	CHL	CHL	CHL
SiO_2	27.19	27.51	28.49	27.73	27.52	27.93	27.22	27.84	28.01	27.82	27.86	27.74	27.44	27.29	27.57	28.08	27.23	27.87	27.91	
Al_2O_3	22.37	22.56	22.22	22.30	22.79	23.50	21.99	22.59	22.22	22.45	22.60	22.41	22.44	23.01	22.96	22.30	22.78	22.79	22.25	
TiO_2	0.00	0.00	0.03	0.04	0.00	0.00	0.03	0.00	0.00	0.03	0.00	0.00	0.02	0.00	0.06	0.00	0.00	0.00	0.02	
K_2O	0.07	0.01	0.57	0.15	0.03	0.01	0.03	0.04	0.06	0.04	0.01	0.01	0.04	0.02	0.00	0.03	0.05	0.09	0.08	
Na2O	0.03	0.00	0.00	0.03	0.02	0.02	0.03	0.00	0.05	0.00	0.02	0.00	0.00	0.01	0.03	0.00	0.04	0.01	0.04	
FeO	17.00	16.56	16.70	16.65	16.46	16.21	16.68	15.77	16.50	16.30	15.97	16.05	16.18	16.57	16.63	16.01	16.91	16.41	16.38	
MgO	23.08	23.41	22.86	22.65	22.98	23.09	22.77	23.76	23.09	23.63	23.34	23.85	23.57	23.36	23.00	23.66	23.01	23.67	22.77	
CaO	0.05	0.00	0.03	0.02	0.01	0.02	0.05	0.02	0.03	0.04	0.04	0.01	0.00	0.00	0.00	0.01	0.00	0.01	0.03	
MnO	0.28	0.22	0.25	0.24	0.27	0.24	0.22	0.25	0.36	0.27	0.22	0.27	0.27	0.22	0.29	0.35	0.35	0.24	0.28	
SrO	0.03	0.00	0.00	0.04	0.00	0.09	0.01	0.00	0.04	0.03	0.01	0.00	0.09	0.00	0.06	0.08	0.02	0.04	0.00	
BaO	0.05	0.00	0.04	0.03	0.00	0.00	0.04	0.00	0.00	0.02	0.00	0.00	0.00	0.00	0.08	0.01	0.07	0.00	0.00	
Cr_2O_3	0.03	0.02	0.01	0.06	0.02	0.00	0.00	0.01	0.00	0.01	0.02	0.00	0.01	0.00	0.00	0.00	0.03	0.00	0.00	
V_2O_3	0.04	0.00	0.00	0.05	0.01	0.00	0.00	0.04	0.01	0.04	0.00	0.00	0.03	0.01	0.07	0.00	0.06	0.04	0.04	
F	0.02	0.00	0.00	0.00	0.00	0.00	0.00	0.04	0.00	0.00	0.04	0.05	0.00	0.09	0.00	0.00	0.00	0.01	0.00	
Cl	0.01	0.00	0.02	0.01	0.03	0.00	0.07	0.01	0.00	0.03	0.00	0.00	0.00	0.01	0.00	0.00	0.01	0.00	0.02	
Total	90.23	90.28	91.21	90.00	90.14	91.10	89.13	90.34	90.36	90.69	90.11	90.38	90.10	90.54	90.73	90.51	90.55	91.17	89.80	

Table 16. Microprobe Data for the Tectonites' Micas

Rock	TCT	TCT	TCT	TCT	TCT	TCT	TCT	TCT	TCT	TCT	TCT	TCT	TCT	TCT	TCT	TCT	TCT	TCT	TCT	TCT
Mineral	MS	MS	MS	MS	MS	MS	MS	MS	MS	MS	MS	MS	MS	MS	MS	MS	MS	MS	MS	MS
SiO_2	42.35	47.23	46.69	46.58	45.94	46.69	47.25	45.09	44.61	45.38	45.49	45.00	44.70	44.55	44.71	44.95	47.04	46.87	46.69	46.56	46.83
Al_2O_3	26.73	30.96	30.87	31.10	30.75	31.31	30.24	35.72	35.56	35.92	35.61	35.47	35.71	35.11	33.32	35.59	31.02	31.46	31.45	31.38	33.46
TiO_2	0.76	0.29	0.25	0.22	0.12	0.19	0.13	0.44	0.41	0.48	0.55	0.52	0.43	0.44	0.36	0.44	0.17	0.22	0.18	0.17	0.89
K_2O	9.65	10.80	11.14	10.91	10.81	10.75	11.00	10.32	10.68	10.23	10.33	10.39	10.36	10.65	10.59	10.11	11.18	10.95	10.74	10.68	11.12
Na2O	0.17	0.27	0.30	0.31	0.19	0.26	0.26	0.75	0.69	0.83	0.90	0.74	0.64	0.44	0.28	0.84	0.35	0.29	0.34	0.24	0.28
FeO	9.80	2.82	2.75	2.64	2.93	2.61	2.97	1.26	1.29	1.15	1.31	1.17	1.35	1.71	2.10	1.38	2.75	2.91	2.61	2.90	2.36
MgO	4.49	2.09	2.04	1.99	1.97	1.78	2.18	0.59	0.64	0.51	0.57	0.54	0.63	0.76	1.08	0.59	1.96	1.98	1.87	1.85	1.73
CaO	0.09	0.00	0.01	0.01	0.06	0.06	0.03	0.01	0.00	0.00	0.01	0.00	0.00	0.00	0.00	0.03	0.02	0.00	0.01	0.00	0.00
MnO	0.00	0.00	0.02	0.00	0.01	0.00	0.00	0.06	0.00	0.00	0.03	0.01	0.02	0.00	0.02	0.00	0.03	0.04	0.01	0.00	0.08
SrO	0.06	0.00	0.03	0.06	0.00	0.08	0.06	0.09	0.11	0.12	0.07	0.05	0.00	0.12	0.02	0.00	0.00	0.12	0.06	0.06	0.03
BaO	0.16	0.23	0.08	0.08	0.07	0.00	0.19	0.06	0.09	0.12	0.11	0.12	0.14	0.00	0.12	0.03	0.17	0.08	0.10	0.22	0.06
Cr_2O_3	0.00	0.03	0.00	0.03	0.00	0.00	0.00	0.00	0.00	0.00	0.00	0.00	0.01	0.00	0.00	0.00	0.00	0.00	0.00	0.00	0.03
V_2O_3	0.02	0.00	0.01	0.00	0.00	0.02	0.01	0.00	0.06	0.00	0.00	0.03	0.07	0.02	0.04	0.09	0.00	0.04	0.03	0.06	0.01
F	0.23	0.12	0.00	0.04	0.00	0.00	0.04	0.00	0.00	0.00	0.00	0.00	0.00	0.00	0.06	0.00	0.03	0.00	0.00	0.00	0.12
Cl	0.04	0.01	0.00	0.00	0.01	0.00	0.01	0.00	0.00	0.02	0.01	0.00	0.00	0.01	0.03	0.02	0.00	0.01	0.00	0.01	0.01
Total	94.43	94.80	94.17	93.94	92.84	93.74	94.34	94.39	94.13	94.75	94.99	94.06	94.05	93.81	92.68	94.06	94.70	94.97	94.09	94.15	96.95

Rock	TCT	TCT	TCT	TCT	TCT	TCT	TCT	TCT	TCT	TCT	TCT	TCT	TCT	TCT	TCT	TCT	TCT	TCT
Mineral	MS	MS	MS	MS	MS	MS	MS	MS	MS	MS	MS	MS	MS	MS	BT	BT	BT	BT
SiO_2	46.18	45.91	46.04	47.07	46.39	47.01	49.55	49.39	49.10	48.34	45.61	46.15	46.41	46.70	38.39	37.99	38.12	37.87
Al_2O_3	33.75	34.23	34.82	32.64	33.85	33.65	29.20	30.02	30.47	31.42	34.77	35.15	34.50	32.95	17.39	17.63	17.40	17.52
TiO_2	0.86	0.98	0.96	0.89	1.06	0.99	0.12	0.25	0.24	0.28	0.86	1.02	1.11	0.67	1.76	1.44	1.36	1.21
K_2O	10.91	10.97	10.71	10.87	11.10	10.98	11.15	11.12	10.87	11.35	10.27	10.60	10.82	11.08	9.60	9.54	9.60	8.97
Na2O	0.42	0.34	0.47	0.30	0.40	0.38	0.22	0.24	0.23	0.28	0.50	0.40	0.41	0.26	0.01	0.02	0.04	0.15
FeO	2.39	2.25	2.09	2.96	2.45	2.39	2.80	2.74	3.15	2.68	2.11	1.89	2.38	2.63	17.36	16.82	16.99	18.03
MgO	1.47	1.30	1.18	1.71	1.47	1.50	2.99	2.86	2.87	2.51	1.11	1.11	1.22	1.95	11.07	11.50	11.52	11.13
CaO	0.02	0.03	0.00	0.04	0.00	0.00	0.00	0.01	0.06	0.00	0.11	0.02	0.02	0.04	0.00	0.05	0.06	0.07
MnO	0.02	0.00	0.00	0.01	0.02	0.00	0.01	0.00	0.00	0.06	0.04	0.05	0.01	0.03	0.22	0.26	0.15	0.23
SrO	0.00	0.02	0.00	0.00	0.04	0.03	0.00	0.02	0.00	0.07	0.08	0.00	0.01	0.00	0.00	0.00	0.08	0.08
BaO	0.00	0.00	0.00	0.09	0.09	0.10	0.00	0.20	0.09	0.20	0.03	0.08	0.00	0.02	0.00	0.02	0.13	0.17
Cr_2O_3	0.00	0.00	0.00	0.01	0.00	0.03	0.00	0.02	0.01	0.01	0.03	0.01	0.00	0.03	0.00	0.00	0.00	0.00
V_2O_3	0.01	0.04	0.00	0.03	0.00	0.01	0.00	0.02	0.06	0.05	0.02	0.06	0.05	0.00	0.00	0.01	0.01	0.03
F	0.08	0.00	0.05	0.08	0.07	0.12	0.20	0.15	0.21	0.18	0.01	0.02	0.00	0.15	1.07	1.15	1.15	1.08
Cl	0.00	0.04	0.00	0.00	0.00	0.01	0.02	0.01	0.04	0.00	0.01	0.03	0.02	0.04	0.05	0.01	0.06	0.05
Total	96.07	96.10	96.29	96.64	96.92	97.11	96.16	96.99	97.29	97.37	95.56	96.56	96.95	96.50	96.45	95.95	96.18	96.10

Table 17. Hydrothermalites' Sulphides Microprobe Data

Mineral	CCP	CCP	CCP	CCP	CCP	CCP	CCP	CCP	CCP	CCP	CCP	CCP	CCP	CCP	CCP	CCP	CCP	GN	GN
As	0	0	0.003	0	0	0	0	0	0	0	0	0	0	0	0	0	0	0	0
S	35.08	34.81	35.36	34.81	35.12	34.67	35.14	34.81	34.93	34.77	35.33	34.94	35.23	35.00	35.01	34.10	34.71	13.33	13.31
Bi	0.09	0.09	0.13	0.17	0.08	0.14	0.13	0.15	0.07	0.13	0.17	0.06	0.15	0.05	0.10	0.12	0.16	1.61	1.12
Pb	0.09	0.04	0.02	0.03	0.09	0.12	0.10	0.14	0.00	0.06	0.12	0.12	0.08	0.04	0.24	0.14	0.08	85.69	86.44
Ag	0.06	0.09	0.00	0.03	0.04	0.02	0.09	0.00	0.28	0.00	0.09	0.01	0.01	0.02	0.00	0.06	0.03	0.27	0.05
Cd	0.04	0.01	0.00	0.00	0.00	0.00	0.01	0.02	0.00	0.02	0.03	0.00	0.00	0.00	0.01	0.00	0.00	0.00	0.00
Sb	0	0	0	0.037	0	0.007	0.022	0.006	0.078	0	0	0.018	0.012	0	0.008	0	0.026	0	0
Se	0.00	0.13	0.29	0.02	0.08	0.08	0.00	0.00	0.02	0.24	0.31	0.00	0.00	0.00	0.19	0.32	0.24	0.00	0.00
Fe	30.59	28.69	29.08	29.64	29.57	28.91	29.07	28.76	30.76	28.19	29.29	28.67	28.46	30.64	29.05	28.32	30.54	0.19	0.20
Co	0.053	0.04	0.053	0.046	0.055	0.024	0.042	0.031	0.04	0.024	0.065	0.052	0.012	0.071	0.029	0.055	0.022	0	0
Cu	33.78	31.16	31.73	32.40	32.31	31.72	31.66	31.94	33.69	30.92	32.08	31.06	31.04	33.39	32.07	30.53	33.38	0.00	0.00
Zn	0.03	0.04	0.05	0.06	0.12	0.00	0.16	0.03	0.09	0.07	0.08	0.03	0.05	0.17	0.10	0.02	0.01	0.00	0.00
Pd	0	0.016	0	0	0	0	0.034	0.011	0	0.003	0.003	0	0	0	0	0.001	0.008	0	0
Au	0	0	0	0	0	0	0	0	0.005	0	0	0	0	0	0	0.003	0	0	0
Pt	0	0	0	0	0	0	0	0	0	0	0	0	0	0	0	0	0	0	0
Total	99.81	95.12	96.72	97.24	97.46	95.68	96.45	95.89	99.96	94.43	97.57	94.97	95.02	99.38	96.80	93.67	99.21	101.09	101.12

Mineral	PO	PO	PO	PO	PO	PO	PO	PO	PO	PY	PY	PY	PY	PY	PY	PY	PY	PY	PY
As	0.011	0	0.011	0.038	0	0	0	0	0	0	0	0.009	0	0	0	0	0	0	0
S	38.70	38.24	38.08	38.31	39.08	38.64	38.77	38.86	38.25	53.74	53.72	53.76	53.59	53.61	53.26	53.94	53.80	53.30	53.72	53.40
Bi	0.03	0.05	0.20	0.11	0.14	0.12	0.24	0.17	0.04	0.20	0.22	0.24	0.10	0.14	0.20	0.14	0.22	0.13	0.18	0.19
Pb	0.18	0.15	0.14	0.13	0.11	0.14	0.03	0.15	0.14	0.11	0.14	0.12	0.07	0.17	0.16	0.10	0.07	0.12	0.12	0.07
Ag	0.01	0.00	0.00	0.00	0.22	0.00	0.00	0.02	0.00	0.00	0.02	0.02	0.00	0.03	0.00	0.00	0.00	0.03	0.03	0.06
Cd	0.02	0.00	0.00	0.02	0.01	0.00	0.01	0.02	0.05	0.01	0.03	0.00	0.00	0.00	0.02	0.00	0.04	0.00	0.01	0.00
Sb	0	0.043	0	0	0	0	0	0.016	0	0	0	0.043	0	0.011	0.04	0.011	0.003	0	0	0.006
Se	0.00	0.16	0.09	0.00	0.00	0.26	0.06	0.00	0.00	0.05	0.00	0.29	0.19	0.21	0.00	0.00	0.07	0.00	0.28	0.06
Fe	62.94	56.22	56.31	56.39	56.89	60.01	57.36	56.28	55.78	47.40	45.57	44.48	44.71	43.59	43.94	46.66	43.37	44.96	44.60	42.83
Co	0.123	0.116	0.089	0.066	0.053	0.066	0.024	0.058	0.077	0.067	0.089	0.094	0.051	0.088	0.077	0.104	0.08	0.062	0.091	0.065
Cu	0.00	0.00	0.02	0.00	0.02	0.00	0.00	0.09	0.01	0.00	0.00	0.00	0.00	0.00	0.00	0.00	0.00	0.00	0.00	0.00
Zn	0.04	0.01	0.06	0.00	0.03	0.03	0.00	0.00	0.00	0.00	0.00	0.00	0.02	0.04	0.00	0.01	0.01	0.00	0.00	0.00
Pd	0.033	0.022	0.006	0	0	0.004	0.004	0.014	0.001	0	0.003	0	0	0.021	0.019	0	0.001	0.008	0	0
Au	0	0	0	0	0	0.007	0	0	0	0	0	0	0	0	0	0	0	0	0	0
Pt	0	0.017	0	0	0.036	0	0	0	0	0	0	0	0	0	0	0	0.041	0	0.009	0.006
Total	102.07	95.02	94.99	95.06	96.58	99.27	96.49	95.66	94.33	101.56	99.79	99.05	98.73	97.89	97.71	100.97	97.71	98.62	99.04	96.68

Table 17 Cont.

Mineral	PY	PY	PY	PY	PY	PY	PY	PY	PY	PY	PY	PY	PY	PY	PY	PY	PY	PY
As	0	0	0	0	0	0	0	0	0	0.008	0	0	0	0	0.009	0.03	0.015	0	0
S	53.56	53.70	53.27	53.98	54.00	53.68	53.75	54.06	54.12	53.87	53.57	53.64	53.52	53.97	53.73	53.44	53.53	53.58	53.07
Bi	0.20	0.17	0.16	0.18	0.14	0.19	0.10	0.12	0.14	0.18	0.26	0.16	0.14	0.21	0.17	0.22	0.19	0.22	0.11
Pb	0.04	0.17	0.10	0.01	0.08	0.09	0.17	0.19	0.28	0.12	0.09	0.18	0.02	0.06	0.12	0.16	0.17	0.23	0.07
Ag	0.03	0.01	0.00	0.00	0.03	0.01	0.00	0.00	0.02	0.03	0.01	0.00	0.00	0.00	0.00	0.00	0.05	0.01	0.02
Cd	0.01	0.06	0.00	0.00	0.00	0.00	0.04	0.05	0.01	0.00	0.00	0.01	0.00	0.00	0.02	0.02	0.00	0.00	0.00
Sb	0.028	0	0	0	0.002	0.013	0.039	0	0.013	0.027	0	0	0.051	0.007	0	0.002	0	0	0
Se	0.00	0.00	0.01	0.15	0.13	0.20	0.00	0.18	0.05	0.20	0.22	0.28	0.00	0.00	0.13	0.00	0.00	0.18	0.17
Fe	45.49	45.69	43.49	45.21	47.09	44.74	44.68	44.87	45.02	43.32	42.52	46.10	42.47	45.62	43.60	43.31	42.89	43.31	44.01
Co	0.117	0.097	0.078	0.077	0.099	0.08	0.082	0.065	0.07	0.091	0.087	0.086	0.073	0.088	0.091	0.058	0.045	0.102	0.098
Cu	0.00	0.02	0.01	0.00	0.02	0.01	0.00	0.01	0.00	0.00	0.00	0.00	0.00	0.00	0.01	0.00	0.02	0.00	0.00
Zn	0.00	0.03	0.04	0.00	0.02	0.01	0.02	0.01	0.00	0.10	0.00	0.01	0.00	0.04	0.01	0.00	0.00	0.01	0.01
Pd	0.006	0.005	0.05	0.005	0	0.011	0	0.009	0.016	0.001	0	0	0	0.008	0.007	0.005	0.004	0	0
Au	0	0	0	0	0	0	0	0	0	0	0	0	0	0.011	0.014	0	0	0	0
Pt	0	0	0	0	0	0	0	0	0	0	0	0	0	0.007	0	0	0	0	0
Total	99.48	99.95	97.21	99.61	101.59	99.03	98.88	99.56	99.73	97.94	96.76	100.46	96.27	100.03	97.90	97.25	96.91	97.64	97.54

Mineral	PY	PY	PY	PY	PY	PY	PY	PY
As	0	0	0.009	0	0	0	0	0
S	53.86	53.21	53.79	53.64	53.62	53.49	53.94	54.08
Bi	0.19	0.05	0.18	0.18	0.12	0.22	0.19	0.16
Pb	0.00	0.12	0.13	0.13	0.18	0.14	0.14	0.11
Ag	0.00	0.00	0.00	0.01	0.00	0.02	0.00	0.00
Cd	0.03	0.00	0.06	0.00	0.00	0.00	0.00	0.00
Sb	0	0	0	0	0	0.027	0	0.001
Se	0.17	0.00	0.05	0.00	0.00	0.06	0.14	0.45
Fe	45.74	43.80	44.31	43.59	44.07	43.38	46.18	45.58
Co	0.093	0.088	0.053	0.094	0.067	0.08	0.127	0.085
Cu	0.01	0.04	0.00	0.00	0.02	0.00	0.03	0.01
Zn	0.00	0.00	0.00	0.03	0.00	0.00	0.00	0.00
Pd	0.004	0.006	0	0	0.015	0	0.007	0.019
Au	0	0	0	0	0	0	0	0
Pt	0	0	0	0	0	0	0	0.05
Total	100.10	97.32	98.58	97.68	98.08	97.42	100.74	100.55

Table 18. Fluid Inclusions Data

Type	Tmice (°C)	Th (°C)	NaCl (wt%)	Density (g/cm³)	Pressure (bar)
IV	-8.4	235.1	12.2	0.93	26.8
IV	-2.3	268.3	3.9	0.80	49.5
IV	-2.8	225.3	4.6	0.87	21.9
IV	-3.3	232.2	5.4	0.87	25.2
IV	-4.6	275.1	7.3	0.83	55.4
IV	-1.9	260.5	3.2	0.81	43.2
IV	-2.7	212.7	4.5	0.89	16.7
IV	-1.9	239.0	3.2	0.84	28.9
IV	-3.6	252.7	5.9	0.85	37.5
IV	-5.5	217.5	8.5	0.92	18.6
IV	-2.5	271.2	4.2	0.80	51.9
IV	-4.2	283.9	6.7	0.81	63.9
IV	-2.4	294.6	4.0	0.76	75.3
IV	-1.7	229.2	2.9	0.85	23.7
IV	-1.5	238.0	2.6	0.84	28.4
IV	-2.6	230.2	4.3	0.87	24.2
IV	-1.3	256.6	2.2	0.80	40.3
IV	-3	262.4	5.0	0.83	44.7
IV	-1.4	224.4	2.4	0.85	21.5
IV	-2.5	240.9	4.2	0.85	30.0
IV	-3.3	257.5	5.4	0.84	40.9
IV	-0.7	206.8	1.2	0.87	14.7
IV	-2.9	244.8	4.8	0.85	32.4
IV	-2.6	220.5	4.3	0.88	19.8
IV	-4.2	243.9	6.7	0.87	31.8
IV	-1.6	281.9	2.7	0.77	61.9
IV	-4.4	254.6	7.0	0.86	38.9
IV	-3.1	246.8	5.1	0.85	33.6
IV	-2.8	271.2	4.6	0.81	51.9
IV	-4.7	220.5	7.4	0.90	19.8
IV	-3.2	264.4	5.3	0.83	46.2
IV	-3.6	279.0	5.9	0.81	59.1
IV	-2.5	297.5	4.2	0.76	78.6
IV	-3.5	227.3	5.7	0.88	22.8
IV	-1.9	251.7	3.2	0.82	36.8
IV	-5.6	286.8	8.7	0.83	66.8
IV	-1.3	240.9	2.2	0.83	30.0
IV	-4.8	233.1	7.6	0.89	25.7
IV	-2	255.6	3.4	0.82	39.6
IV	-1.8	221.4	3.1	0.87	20.2
IV	-4.2	236.1	6.7	0.88	27.3
IV	-3.7	249.7	6.0	0.86	35.5
IV	-2.5	241.9	4.2	0.85	30.6
IV	-5.1	252.7	8.0	0.87	37.5
IV	-2.2	272.2	3.7	0.80	52.8
IV	-2.9	225.3	4.8	0.88	21.9
IV	-1.7	245.8	2.9	0.83	33.0
IV	-4	253.6	6.4	0.86	38.1
IV	-3.3	255.6	5.4	0.84	39.6
IV	-4.3	267.3	6.9	0.84	48.6
Mean:	-3.09	249.1	5.0	0.84	37.3